

**A HUMAN MOTOR CONTROL-INSPIRED
CONTROL SYSTEM FOR A WALKING HYBRID
NEUROPROSTHESIS**

by

Naji A. Alibeji

BS in Mechanical Engineering, University of Pittsburgh, 2012

Submitted to the Graduate Faculty of
the Swanson School of Engineering in partial fulfillment
of the requirements for the degree of
Doctor of Philosophy in Mechanical Engineering

University of Pittsburgh

2017

UNIVERSITY OF PITTSBURGH
SWANSON SCHOOL OF ENGINEERING

This dissertation was presented

by

Naji A. Alibeji

It was defended on

June 8, 2017

and approved by

Nitin Sharma, PhD, Assistant Professor

Department of Mechanical Engineering and Materials Science and Department of

Bioengineering

William Clark, PhD, Professor

Department of Mechanical Engineering and Materials Science

Daniel Cole, PhD, Associate Professor

Department of Mechanical Engineering and Materials Science

Zhi-Hong Mao, PhD, Associate Professor

Department of Electrical and Computer Engineering and Department of Bioengineering

Dissertation Director: Nitin Sharma, PhD, Assistant Professor

A HUMAN MOTOR CONTROL-INSPIRED CONTROL SYSTEM FOR A WALKING HYBRID NEUROPROSTHESIS

Naji A. Alibeji, PhD

University of Pittsburgh, 2017

The purpose of this research is to develop a human motor control-inspired control system for a hybrid neuroprosthesis that combines functional electrical stimulation (FES) with electric motors. This device is intended to reproduce gait for persons with spinal cord injuries (SCI). Each year approximately 17,000 people suffer from an SCI in the U.S. alone, of which about 20% of them are diagnosed with complete paraplegia. Currently, there is a lot of interest in gait restoration for subjects with paraplegia but the existing technologies use either solely FES or electric motors. These two sources of actuation both have their own limitation when used alone. Recently, there have been efforts to provide a combination of the two means of actuation, FES and motors, into gait restoration devices called hybrid neuroprostheses.

In this dissertation the derivation and experimental demonstration of control systems for the hybrid neuroprosthesis are presented. Particularly, the dissertation addresses technical challenges associated with the real-time control of a FES such as nonlinear muscle dynamics, actuator dynamics, muscle fatigue, and electromechanical delays (EMD). In addition, when FES is combined with electric motors in hybrid neuroprostheses, an actuator redundancy problem is introduced. To address the actuator redundancy issue, a synergy-based control framework is derived. This synergy-based framework is inspired from the concept of muscle synergies in human motor control theory. Dynamic postural synergies are developed and used in the feedforward path of the control system for the walking hybrid neuroprosthesis. To address muscle fatigue, the stimulation levels are gradually increased based on a model-based fatigue estimate. A dynamic surface control technique, modified with a delay compensation

term, is used to address the actuator dynamics and EMD in the control derivation. A Lyapunov-based stability approach is used to derive the controllers and guarantee their stability. The outcome of this research is the development of a human motor control-inspired control framework for the hybrid neuroprosthesis where both FES and electric motors can be simultaneously coordinated to reproduce gait. Multiple experiments were conducted on both able-bodied subjects and persons with SCI to validate the derived controllers.

TABLE OF CONTENTS

1.0 INTRODUCTION	1
1.1 Motivation and Problem Statement	2
1.2 Research Objectives	8
1.3 Research Impact and Significance	10
1.4 Dissertation Outline	11
2.0 MUSCULOSKELETAL MODELING OF THE HYBRID NEUROPROS- THESIS AND THE EXPERIMENTAL TESTBEDS	14
2.1 Musculoskeletal Models	15
2.1.1 Walking Hybrid Neuroprosthesis Model	15
2.1.2 Knee Extension Model	19
2.1.3 Fixed Hip Model	21
2.2 Experimental Testbeds	25
2.2.1 Hybrid Neuroprosthesis	25
2.2.2 Leg Extension Machine	25
3.0 HUMAN MOTOR CONTROL-INSPIRED ARTIFICIAL SYNERGY- BASED CONTROLLER FOR A HYBRID NEUROPROSTHESIS	30
3.1 Introduction	30
3.2 Control Development	31
3.2.1 Control Objective	31
3.2.2 Synergy Extraction	32
3.2.3 Closed-Loop Error System	33
3.3 Stability Analysis	35

3.4	Simulations	37
3.4.1	Fixed Hip Model	37
3.4.1.1	Dynamic Optimizations	37
3.4.1.2	Simulation Results	38
3.4.2	Walking Hybrid Neuroprosthesis Model	38
3.4.2.1	Dynamic Optimizations	44
3.4.2.2	Simulations Results	45
3.5	Conclusion	57
4.0	DELAY COMPENSATION CONTROL FOR FES-BASED MUSCULO-	
	LOSKELETAL SYSTEMS WITH INPUT DELAY	59
4.1	Introduction	59
4.2	Control Development	60
4.2.1	Control Objective	60
4.2.2	Closed-Loop Error System	61
4.3	Stability Analysis	63
4.4	Experimental Protocol	67
4.5	Experimental Results	69
4.6	Conclusion	76
5.0	DYNAMIC SURFACE CONTROL OF FUNCTIONAL ELECTRICAL	
	STIMULATION SYSTEMS WITH ACTIVATION DYNAMICS	78
5.1	Introduction	78
5.2	Control Development	79
5.2.1	Control Objective	80
5.2.2	Closed-Loop Error System	81
5.3	Stability Analysis	83
5.4	Experimental Protocol	88
5.5	Experimental Results	90
5.6	Conclusion	91
6.0	HUMAN MOTOR CONTROL-INSPIRED SYNERGY-BASED PID-	
	DSC CONTROLLER WITH DELAY COMPENSATION	95

6.1	Introduction	95
6.2	Control Development	96
6.2.1	Control Objective	96
6.2.2	Synergy Extraction	97
6.2.3	Closed-Loop Error System	98
6.3	Stability Analysis	102
6.4	Simulations	108
6.5	Experimental Protocol	113
6.6	Experimental Results	121
6.7	Discussion	126
6.8	Conclusion	128
7.0	EXPERIMENTAL DEMONSTRATION OF THE SYNERGY-BASED PID-DSC CONTROLLER IN A WALKING HYBRID NEUROPROS- THESIS	130
7.1	Introduction	130
7.2	Dynamic Postural Synergies	131
7.2.1	Computing the Synergies	131
7.2.2	Computing the Synergies' Activation	133
7.3	Finite State Machine	136
7.4	Experimental Results	139
7.5	Discussion	148
7.6	Conclusion	150
8.0	SUMMARY	151
8.1	Contributions	152
8.2	Future Work	155
	BIBLIOGRAPHY	157

LIST OF TABLES

3.1	The root mean squared (RMS) error for the four simulated cases. Case 3 which had 2 synergies and feedback and Case 4 which had full optimal feedforward and feedback had the smallest RMS errors, followed by the Case 2 which had just adaptive feedforward, and then Case 3 with the non-adaptive feedforward.	52
4.1	The gains used to produce the experimental results shown in Fig. (4.1).	71
4.2	The tabulated results for the sinusoidal trajectory with 2 second time period ranging from 5 – 50° implemented on subject H1 with all three controllers.	71
4.3	The tabulated results for the sinusoidal trajectory with 2 second time period experiments include the average (AVG) and standard deviation (SD) of the EMD values measured for each volunteer subject (S) across five samples, the average root mean squared error (RMSE), the average steady state RMSE (SSRMSE), and the average root mean squared current (RMSC) normalized by the body mass index of each subject.	73
4.4	Tabulated results for the robustness of the estimated EMD value in the PID-DC controller as opposed to the measured EMD value of 85 <i>ms</i> . Note that the controller was able to maintain consistent performance even with mismatched EMDs after tuning β (ATB). The results for the estimated EMD values before tuning β (BTB) were included to demonstrate the effect of tuning β .	76
5.1	The tabulated results for the 4 second trajectory experiments include the EMD measured for each volunteer subject (S), the average root mean squared error (RMSE), the average steady state RMS error (SSRMSE), and the average RMS Current (RMSC) normalized by the body mass index of each subject.	94

6.1 The subject specific parameters and motor parameters extracted in the system identification experiments. Notice that the motors do not have any fatigue parameters or input delays. 119

LIST OF FIGURES

2.1	A 4-link gait model based of a subject wearing a hybrid neuroprosthesis while using a walker. The model has 10 inputs including FES of 6 muscles (antagonistic hip, knee, and ankle muscle pairs in the swing leg), 3 electric motors acting on each joint of swing leg (T_h, T_k, T_a), and a walker moment acting on the stance leg (M_w). The step length is defined as the distance from stance toe to swing toe.	16
2.2	Schematic of a subject sitting in the leg extension machine with a knee torque generated via NMES.	19
2.3	A schematic of the fixed hip model with no ground model. The pink muscle bellies labeled u_{he} , u_{hf} , u_{ke} , and u_{kf} indicate the stimulated muscles that produce hip/knee flexion and extension and the torques produced by the motors at both joints are labeled T_{hm} and T_{km}	22
2.4	The hybrid neuroprosthesis in the fixed hip model configuration. An electric motor is used at the hip and knee joint and FES of the hamstrings and quadriceps muscle group.	26
2.5	The hybrid neuroprosthesis in the walking configuration. An electric motor is used at the hip and knee joints of each leg and FES of the hamstrings and quadriceps muscle group.	27
2.6	The modified leg extension machine (LEM) used for the knee extension experiments. The LEM was instrumented with a load cell to measure force output and incremental encoder to measure the knee joint angle.	29

3.1	This graph shows how much variance is accounted for based on the number of principal components used. Typically, the number of principal components that account for over 90% of the variance is sufficient for decreasing dimensionality while being able to reconstruct the ideal input data to over a 90% match.	39
3.2	The joint angles resulting from simulating low dimensional controller. The top plot shows the desired and actual hip angle and the bottom plot shows the desired and actual knee angle, each for five steps.	40
3.3	These plots show the ideal inputs generated from optimizations and the actual inputs resulting from using only 3 principal components with the adaptive update law. Notice that the actual inputs for each muscle u_{he} , u_{hf} , u_{ke} , and u_{kf} at some instances were negative. These instances were replaced with zeros because the muscles are uni-directional actuators.	41
3.4	This figure shows the motor inputs from feedback control for the two motors.	42
3.5	The normalized fatigue variable for the four muscles: hip and knee flexors/extensors. The fatigue variable ranges from zero to one, which corresponds to full fatigue and no fatigue, respectively.	43
3.6	Optimal gait trajectories for a step size of 0.4 meters in 0.75 seconds.	46
3.7	Optimal inputs to the walker moment, electric motors, and stimulation channels to reproduce the optimal gait trajectories.	47
3.8	This plot indicates how much of the data variability would be accounted for based on the number of synergies considered. Rule of thumb would indicate using 3 synergies, but since the controller is not solely dependent on the feed-forward component less synergies can be used.	48
3.9	(a) Two synergies, w_1 and w_2 . (b) The corresponding time-varying activation coefficients, c_1 and c_2 , of synergies, w_1 and w_2	49

3.10	Four cases for gait control using a hybrid neuroprosthesis. Case 1 only used the feedforward synergies, Case 2 used the adapted feedforward synergies, Case 3 considered both the adapted feedforward synergies and feedback control, and Case 4 used the full optimal inputs and feedback control. Note that the profile from the third and fourth cases almost perfectly overlaps the desired profiles.	51
3.11	Control inputs for Case 1 & 2 of the simulations. Notice that the control input profile shapes, after PCA decomposition, in Case 1 may not be similar to the optimal inputs in Fig. 3.7.	53
3.12	Control inputs for Case 3 of the simulations. The feedback's contribution was used only in the walker moment and motor torques.	54
3.13	Control inputs for Case 4 of the simulations. The feedback's contribution was used only in the walker moment and motor torques.	55
3.14	The gait sequence for the four cases, a step length of 0.4 meters with a step duration of 0.75 seconds was used. Since the errors for the third and fourth cases are so close their gait sequences look identical.	56
4.1	Experimental results obtained from the representative trial for each of the three controllers. These plots show the desired & actual angular position (top plots), error (middle plots), and stimulation current amplitude (bottom plots).	70
4.2	Results obtained from running the three controllers on subject H1 with a larger trajectory ranging from $5 - 50^\circ$.	71
4.3	A graphical representation of the results from the LEM experiments. The three criteria: RMSE, SSRMSE, and RMSC were normalized by the maximum of each criterion after the ANOVA analyses were done. * indicates statistically significant differences between the controllers at a 95% confidence level and p refers to the p-value.	72
4.4	Tracking performance of PID-DC with mismatched EMDs that were set to ± 2 SDs away from the mean measured EMD. With mismatched EMD settings, the performance degraded but the PID-DC maintained stability. Top plot: the control performance, before tuning β . Bottom plot: the tracking performance improved after tuning β .	75

5.1	The control schematic for the implementation of the new PID-based DSC controller with delay compensation.	79
5.2	A visual representation of the 3 step data processing of the system identification experiments. Step 1: find the EMD value. Step 2: shift the measured force signal. Step 3: find the activation time constant that produces the best fit.	89
5.3	Experimental results obtained from the best trial for each controller: (a) PID-DSC and (b) PID-DC. These plots show the desired & actual angular position (top plots), error (middle plots), and stimulation current amplitude (bottom plots). (c) A graphical representation of the results from the LEM experiments. The three criteria: RMSE, SSRMSE, and RMSC were used to compare the controllers. The error bars show the standard error of the mean for each criteria. Miss-matching letters (A & B) indicate statistically significant differences between the controllers at a 95% confidence levels.	92
5.4	Experimental results obtained from the best trial for each controller: (a) PID-DSC and (b) PID-DC on subject S1. These plots show the desired & actual angular position (top plots), error (middle plots), and stimulation current amplitude (bottom plots).	93
6.1	The control schematic for the implementation of the adaptive synergy based PID-DSC controller with delay compensation.	103
6.2	Optimal activations generated from dynamic optimizations. The peak in the hip flexion and knee extension are intentionally computed by the dynamic optimizations to counteract the passive torques near hyper flexion and hyper extension.	110
6.3	Number of synergies vs. Reconstruction variance	111
6.4	(a) Three synergies: w_1 , w_2 , and w_3 after dimension reduction. (b) The corresponding time-varying synergy activation c_1 , c_2 , c_3 , of the three synergies.	112

6.5	The control performance of the joint angles resulting from simulating the newly developed controller. Top plots the desired and actual hip joint angle. Bottom plots the desired and actual knee joint angle, each for the first and last five seconds of the 5 min. simulation.	114
6.6	Feedforward component, $\hat{\phi}^{-1}\zeta_{sf}W\hat{c}$ in $\bar{\mu}$, reconstructed through the reduced synergies after adaptation and with the scaling up from the fatigue estimates. The first and last 5 seconds of the signals are shown to illustrate the increases in the signal amplitude as the muscles fatigue.	115
6.7	The first and last 5 seconds of the feedback component, kr in $\bar{\mu}$, which was only applied to the two motors.	116
6.8	The normalized inputs to the system, u . The first and last 5 seconds are shown for the stimulation inputs to show the effect of the scaling due to the fatigue estimate.	117
6.9	The normalized fatigue variable for the four muscles, hip and knee flexors/extensors, over the 5 minute trial. The fatigue variable ranges from zero to one, which correspond to full fatigue and no fatigue, respectively.	118
6.10	The testbeds used to conduct the experiments: (a) a hybrid exoskeleton with electric motors at the hip and knee joint and stimulation of quadriceps and hamstrings was used to implement the new controller and (b) a modified leg extension machine with a load cell to measure force was used to perform system identification experiments.	119
6.11	The synergies used in the preliminary experiments: (a) Two synergies: w_1 and w_2 after dimension reduction. (b) The corresponding time-varying synergy activation profiles c_1 and c_2	120
6.12	The joint angles resulting from the newly developed controller in experiments. Top plots the desired and actual hip joint angle. Bottom plots the desired and actual knee joint angle, each for five cycles.	122
6.13	The feedforward component of $\bar{\mu}$ which is reconstructed through the synergies after adaptation and with the scaling up from the fatigue estimate.	123
6.14	The feedback component of $\bar{\mu}$, which were only applied to the motors.	123

6.15	A comparison between the desired activation $\bar{\mu}$ and the estimated activation $\hat{\mu}$.	124
6.16	The inputs for the motors and stimulation during the experiments. Note that the stimulation levels start at the minimum value which differs for each muscle.	124
6.17	The normalized fatigue variable estimate for the knee flexors and extensors. The fatigue variable ranges from zero to one, which correspond to full fatigue and no fatigue, respectively.	125
7.1	The dynamic postural synergies computed through the optimizations and the dynamic postures they result in when activated.	134
7.2	(A) The dynamic postural synergies (a) and their activation to produce a half step (b), (B) the joint trajectories they produce, (C) the gait sequence for the half step.	137
7.3	(A) The dynamic postural synergies (a) and their activation to produce a full step (b), (B) the joint trajectories they produce, (C) the gait sequence for the full step.	138
7.4	The Finite State Machine determines the desired trajectories and synergy activations based on what state is activated; either half right step, full left step, or full right step. Then two controllers are used, one for each leg, which work in tandem to produce gait.	140
7.5	(A) The desired and actual joint angles of the right and left hip and knee joints resulting from using the developed synergy-based DSC/DC control system in conjunction with the FSM on an able-bodied subject. The shaded regions indicate which state of the FSM is active at that time. In addition, the role of the leg; whether it is the stance leg or swing leg, is also indicated. (B) A sequence of photos illustrating the gait produce during the experiments.	142
7.6	The desired feedforward component of $\bar{\mu}$ for all of the system inputs. This component is generated from the dynamic postural synergies and their activation after adaptation and with the scaling up from the fatigue estimate and the scaling factor control gain.	143

7.7	The desired feedback component of $\bar{\mu}$ which is only applied to the four motors at the hip and knee joints of each leg. It can be observed that they majority of the effort is occurring during the swing phase of each leg.	144
7.8	The fatigue estimates for the knee flexors and extensors of both legs. The fatigue estimate ranges from 1 to ϕ_{min} , which corresponds to no fatigue to fully fatigued, respectively. It can be observed that the fatigue occurs during the swing phase, and the muscles recover during the stance phase since there is no stimulation.	145
7.9	The inputs to all of the system inputs for this experimental trial. Note that there is no stimulation occurring during the stance phase of each leg.	146
7.10	The synergy activation after adaptation for both legs. Note that the synergies are not activated during the stance phase of each leg.	147

ACKNOWLEDGEMENTS

I would like to express my gratitude to my advisor, Dr. Nitin Sharma, for all of his guidance over the years. I am also grateful to my committee members Dr. Daniel Cole, Dr. William Clark, and Dr. Zhi-Hong Mao for their guidance and the knowledge they have shared with me in and out of the classroom over the years.

I would like to thank my friend and long time colleague Dr. Nicholas Kirsch who worked side by side with me over the years. He was a tremendous resource and it would have been a lonely lab without him.

I would like to thank my friends and fellow doctoral students for their feedback, cooperation and of course friendship. In addition, I would like to thank the volunteers that took the time to participate in experiments.

This dissertation would not have been possible without funding from the National Science Foundation Award no. 1462876.

Last but not the least, I would like to thank my family: my parents, brother, sisters, brother-in-laws, sister-in-laws for supporting me spiritually throughout writing this dissertation and my life in general.

I would like to dedicate this dissertation to my parents, Abdullah and Semira, for all the sacrifices they have made over the years for me and my siblings. It is because of their guidance and example that I am the man I am today.

1.0 INTRODUCTION

The purpose of this research is to develop a human motor control-inspired control system that provides adequate real-time performance for a hybrid neuroprosthesis that is capable of reproducing gait. Hybrid neuroprostheses are devices that use a combination of functional electrical stimulation (FES) and electric motors to restore gait in subjects with paraplegia. Currently, there is a lot of interest in gait restoration for subjects with paraplegia, but the existing technologies use either solely FES or electric motors, which each have their own limitation when used alone. Recently, there have been efforts to combine the two means of actuation, FES and motors, into a single gait restoration device called hybrid neuroprostheses. The use of FES can provide supplementary torque, which will allow for smaller motors that require less energy storage, and have added health benefits for the user, e.g., improved cardiovascular health and increased muscle mass and bone density. However, the control of FES can be difficult due to the nonlinear muscle dynamics, Ca^{2+} activation, electromechanical delays (EMD), and muscle fatigue. In addition, hybrid actuation uses FES and electric motors to influence the same degree of freedom (DOF) which introduces an actuator redundancy problem. This research overcomes these challenges by using control methods inspired by concepts from human motor control theory, while considering system stability. The benefits of this research are the development of a more efficient control system for a hybrid neuroprosthesis that addresses actuator redundancy, actuator dynamics, EMD, and muscle fatigue.

Primary Goal and Objectives: The primary goal of this research has been to derive a human motor control-inspired control system with a guarantee of stability for a hybrid neuroprosthesis. The control system must address the challenges associated with real-time

control of hybrid neuroprosthesis: actuator redundancy, electromechanical delays, actuator dynamics, and fatigue. These four objectives guide this research:

1. Establish a synergy-based control hierarchy to address actuator redundancy.
2. Address actuator dynamics and EMD by modifying and using a dynamic surface control structure.
3. Compensate for fatigue by incorporating a fatigue-based scaling factor in the controller.
4. Implement the synergy-based control system in walking experiments on human subjects.

1.1 MOTIVATION AND PROBLEM STATEMENT

Neurological dysfunctions caused by spinal cord injury (SCI), stroke, multiple sclerosis, traumatic brain injury, etc., are the leading causes of mobility disorders among adults across the world. Each year there are approximately 3,400 new cases of complete paraplegia due to an SCI in the U.S. alone [105]. Complete paraplegia of persons impairs their walking function and hinders their ability to perform activities of daily living. This loss of, or limited, limb functionality of their motor control of the lower extremities typically leaves the subjects confined to a wheelchair, significantly limiting their mobility. Until recently, there have been only two viable technologies that may help restore walking function in persons with SCI: Functional electrical stimulation and powered orthoses.

FES is the use of neuromuscular electrical stimulation (NMES) to produce muscle contractions that provide a function [76]. NMES is the application of artificial electrical potentials across a muscle group to elicit a muscle contraction. NMES is prescribed as an intervention to rehabilitate or restore functionality in mobility-impaired individuals [77]. For example, NMES can be used to produce advanced functional tasks such as upper extremity reaching and grasping [15, 17, 88, 106], rowing [19], single leg extension [30, 31, 33, 50, 87, 93, 94, 96], and stationary bicycling [8, 49, 52]. Gait restoration of subjects with paraplegia through the use of FES is a popular research problem that still remains unsolved [48, 58, 71, 92, 98].

When specific muscles are stimulated in an appropriate sequence and supplemented with a walker or crutches, walking movements can be reproduced. The first attempt to produce gait patterns using transcutaneous electrical stimulation of the quadriceps and glutei was presented in Kantrowitz et al. [51] and the first FES system to improve gait was developed in 1961 by Liberson et al. [62] to correct drop foot. Since then many FES based gait restoration systems have been developed [7, 43, 48, 58, 59, 66]. In Bajd et al. a combination of stimulation to the peroneal nerve, to produce withdraw reflex, and quadriceps to produce knee extension is used to achieve a rudimentary gait for subjects with an SCI [7]. However, FES-based walking restoration systems have achieved limited acceptability among persons with mobility disorders due to the rapid onset of muscle fatigue and other technical challenges such as coordinating multiple muscles with FES, EMD, poor and unreliable muscle force generation by electrical stimulation, and upper-body effort required to maintain balance while walking. Moreover, controlling FES can be cumbersome due to the highly nonlinear muscle dynamics. Although the majority of the aforementioned work uses ad hoc control methods or open-loop control, closed-loop control is typically employed to achieve accurate and precise limb control during NMES-elicited tasks. However, closed-loop control of NMES is challenging due to the uncertain and nonlinear musculoskeletal system and presence of muscle fatigue, unmodeled disturbances such as muscle spasticity or external changes in muscle loads, EMD, and Ca^{2+} activation dynamics.

To reduce the effects of muscle fatigue, FES can be used in conjunction with a passive orthosis [35, 42, 57, 101]. The addition of an orthosis lowers the metabolic cost of walking by providing a relatively natural and stable gait, reducing the load on a user's arms, and decreasing the stimulation duty cycle of FES. However, this type of a walking system can be disadvantageous because the power is still only provided by FES, which deteriorates with FES-induced muscle fatigue. Recently, powered exoskeletons that use electric motors, or other forms of external actuation, to assist or elicit lower-limb movements have been developed [34, 73, 102]. Unlike FES, powered exoskeletons reliably generate joint torque and can coordinate joint movements with high accuracy. However, the powered exoskeleton requires larger heavier batteries to sustain walking for long periods of time, which adds weight and bulk to the device.

A more viable technology for gait restoration is a hybrid device that combines an FES system with a powered exoskeleton [21,22,46,55,56]. With such a system, the limitations of FES such as limited and unreliable muscle torque generation, can be overcome by using an electric motor. Also, intermittent use of FES would provide therapeutic benefits to a user. This would also help conserve the battery charge required for an electric motor because a portion of the joint torque can be generated by FES; thus, resulting in smaller and lighter batteries and motors. However, the use of an electric motor and FES at each joint creates an actuator redundancy problem, which is a control challenge as there is no unique solution as to how to distribute the control effort among the multiple actuators. For example, in a hybrid walking system that controls 4 lower limb joints, 12 actuators need to be controlled if applying FES via surface electrodes. These actuators include FES of the antagonistic muscle pairs and an electric motor at each joint. Thus, a challenge for a controller for the hybrid system is to be able to allocate the control efforts between the redundant actuators to produce a coordinated movement.

Recent control methods developed for hybrid walking exoskeletons include open-loop FES control with a feedback controller for controlled brakes [31,41,42,81], iterative learning control [21,39], adaptive gain control [45,82], a finite state machine (FSM) was used to control an orthosis which combined FES with hydraulic actuators and wrap-spring clutches [57]. Although these pioneering control approaches are interesting, these methods did not consider control of multiple muscle stimulation and multiple electric drives applied to multiple DOFs. Further, these control methods do not follow a formal control development and do not provide stability guarantees. Thus, there is a lack in research on the systematic design of automatic control algorithms with stability guarantee for a hybrid walking system that addresses actuator redundancy.

As researchers, we often analyze biological systems to devise innovative solutions to real world applications. To overcome the challenge of actuator redundancy, I looked to how scientist believed the human body solves its high degree of freedom and actuator redundancy problem to achieve fluid and coordinated movements such as gait. It is hypothesized that the human central nervous system (CNS) activates multiple muscle fibers in groups or patterns called muscle synergies, or motor primitives, to efficiently perform complex movements

such as posture control and hand manipulations [18, 97, 107, 114, 115]. A small number of muscle synergies has been shown to capture various muscle patterns across different behavioral and task conditions. This is typically done by collecting electromyography data from a large number of muscles during tasks and performing statistical analyses. Some of the more common analysis techniques used are non-negative matrix factorization (NNMF), principal component analysis (PCA), partial least squares regression (PLSR), or singular value decomposition (SVD) to transform the system into a lower dimensional system while keeping as much of the variance of the data as possible. The underlining concept is the transformation of a high dimensional, complex system to a lower dimensional, simpler system that is easier to control [110]. Muscle synergies have also been studied for human locomotion and the extracted synergies have been successfully applied to complex human walking models to reproduce realistic gait motions [72]. For a more thorough background on the literature pertaining to synergies, the reader is referred to these references [110, 115]. In this research I use a synergy-based control system to distribute the control effort to the multiple actuators of a walking hybrid neuroprosthesis. Based on the synergy principle fewer control signals are used to control multiple actuators in a hybrid neuroprosthesis, therefore the use of synergies will not only solve the actuator redundancy problem similarly to how the body is hypothesized to do so, it will do it in a more computationally efficient way. However, there are still other remaining challenges that could hamper the effectiveness of a closed-loop synergy-based control system if not addressed. These remaining challenges are EMD, actuator dynamics, and muscle fatigue. Therefore, I have looked into formal control design approaches to make the synergy-based control robust to EMD and compensate for activation dynamics and muscle fatigue.

Electromechanical delays are classified as a time lag between the application of electrical stimulation to the motor-neurons and the buildup of tension in the muscles as they contract. The causes of EMD are accredited to various phenomena such as finite propagation time of the chemical ions in the muscle, cross-bridge formation between actin-myosin filaments, stretching of the series elastic components in response to the external electrical input, synaptic transmission delays, and others [14, 121]. Typically, the EMD is modeled as an input delay in the musculoskeletal dynamics [50, 87, 90]. Input delays can cause performance

degradation and have been reported to potentially cause instability during human stance experiments [67]. Despite the fact that EMDs are exhibited in muscle response and can lead to instability, NMES controllers that actively compensate for this phenomena are lacking. Previous results, such as in the work by Vette et al. and Masani et al. [67,68,112,113], examine EMD effects by implementing a standard proportional derivative (PD) controller during stance (or quiet standing) experiments that show robustness to the delays. The controllers in such results have not been modified to include a delay compensation (DC) term and have no mathematical proof of stability when the plant has uncertainties, nonlinearities, and/or disturbances.

Various methods exist in the general time-delay control literature to compensate for actuator or input delays, but the existing approaches such as Smith predictor methods [100], Artstein model reduction [6], finite spectrum assignment [65], and continuous pole placement [69] are applicable to only linear plants. The control problem becomes especially complicated when parametric uncertainties, nonlinearities, and additive disturbances are considered. Recently, two predictor-based control methods have been developed for an uncertain input delayed system with additive disturbances [95]. These results suggest that a PD or a proportional integral derivative (PID) controller can be augmented with a delay compensator that contains a finite integral of past control values to transform the delayed system into a delay-free system. Motivated by the modified PD control result in [95], a tracking controller for a nonlinear musculoskeletal system with known constant input delay, the proportional derivative with delay compensation (PD-DC), has been developed in Sharma et al. [90]. Only the modified PD control result was extended in [90] as the modified PID controller in Sharma et al. [95] requires a knowledge of inertia matrix. Thus, the PID-type delay compensating control design proposed in Sharma et al. [95] cannot be implemented because of many uncertainties in the musculoskeletal system that form an unknown nonlinear input gain to the voltage input. These uncertainties include the unknown moment of inertia, muscle force-length and force-velocity relationships, moment arm, etc. Recently, much research has gone into developing automatic closed-loop controllers, which are augmented with delay compensation terms to deal with input delays [2,3,74,90,91]. However, the aforementioned works ignore the activation dynamics.

The neuromuscular activation dynamics describe Ca^{2+} ion activation and deactivation dynamics that primarily facilitate the muscle force generation [36] and can be modeled as a first-order ordinary differential equation [87] or a Hammerstein structure [32, 37, 38]. The activation dynamics couple neural excitations to the muscle contraction dynamics (muscle force-length and force-velocity relationships) that drive the second order musculoskeletal dynamics. Although the activation dynamics change the behavior of the system, typically controllers designed for NMES ignore them [2, 30, 94] or use ad hoc methods without considering their effects on the stability [50, 63]. An integrator backstepping-based approach was used to design a neural network-based NMES controller for a musculoskeletal system with fatigue and calcium dynamics [93]. However, the control design required an acceleration signal during the control implementation. This requirement of the acceleration signal is due to the use of the integrator backstepping approach, which is associated with the “explosion of terms” for systems of higher order. Recently, a controller was designed for an NMES-driven musculoskeletal system with activation dynamics that used dynamic surface control (DSC) to avoid the “explosion of terms” problem [4]. DSC is a modified version of multiple sliding surface (MSS) control, which is very similar to integrator backstepping. A DSC approach, first developed by Swaroop et al. [103, 104], is a robust nonlinear control technique that uses the dynamics of first order low-pass filters to avoid the “explosion of terms” associated with IB and MSS. Since then, the DSC was extended to an adaptive DSC for linearly parameterizable uncertainties [120]. Later in [117], a neural network based adaptive DSC was developed for an uncertain nonlinear system regulation problem. More recently, in [47] an adaptive dynamic surface control scheme is combined with sliding mode control and recurrent neural networks for robust positioning control of a linear motion stage. The challenge of activation dynamics can be even more detrimental when combined with the actuator redundancy problem created by using different types of actuators such as electric motors and FES in hybrid neuroprostheses. The differences in the speeds of response of the different actuators can lead to ineffective or uncoordinated movements if not considered.

Muscle fatigue is defined as the decline in the ability of a muscle to produce a force and occurs as a result of nervous system or metabolic fatigue. The use of transcutaneous FES non-selectively activates the same muscle fibers repeatedly resulting in the rapid increase of

muscle fatigue [10, 61, 86]. The use of a powered orthosis in hybrid neuroprostheses helps to reduce the effects of muscle fatigue, however fatigue still occurs and can deteriorate control performance over time. This is especially apparent for open-loop controllers or feedforward control components if they do not adapt over time. Some studies have proposed different stimulation strategies [11, 27, 64] to prolong the onset of muscle fatigue such as choosing different stimulation patterns and parameters, improving fatigue resistance through muscle retraining, and sequential stimulation. Other studies used fatigue model-based feedforward control to counteract the effects of fatigue [23, 24, 40, 83, 84]. In Downey et al. a closed-loop control methodology that used asynchronous stimulation, alternating between multiple stimulation channels that produce the same movement, was developed to minimize the effects of fatigue [28, 30]. In Kirsch et al. a model-based estimator of the fatigue was used in the closed-loop control law to compensate for the fatigue [54].

Hybrid neuroprostheses are a promising form of gait restoration devices that have the potential to not only restore walking function in subjects with SCI, but also provide therapeutic benefits through FES. However, the limitation of these devices is that the real-time control of this system can be challenging due to the actuator redundancy, actuator dynamics, EMD, and muscle fatigue. In the aforementioned works, the limitations of closed-loop control of hybrid neuroprostheses were addressed by using ad hoc methods or ignoring them altogether. This can result in a less efficient gait restoration device with potential system instability. In this dissertation, a human motor control-inspired control system that considers the aforementioned challenges is developed using Lyapunov control design and stability methods.

1.2 RESEARCH OBJECTIVES

The following objectives aided in the derivation and experimental demonstration of a human motor control-inspired control system for a walking hybrid neuroprosthesis.

- **Objective 1: Establish a synergy-based control hierarchy to address actuator redundancy.**

These research efforts establish a control system for a hybrid neuroprosthesis. The hybrid actuation structure of these devices result in an actuator redundancy problem which makes it challenging to distribute the control effort while maintaining coordinated movements. This research uses concepts from human motor control theory that explain how the human body is able to resolve the actuator redundancy problem of the musculoskeletal system while achieving coordinated movements. More specifically, this research incorporates the concept of muscle synergies, which until now were primarily used as an analysis tool, in the control system. A synergy-based control hierarchy that serves as the foundation of the control system for the hybrid neuroprosthesis has been developed. In addition, different forms of synergies for a hybrid neuroprosthesis have been identified to be used in the control system.

- **Objective 2: Address actuator dynamics and EMD by modifying and using a dynamic surface control structure.**

Hybrid neuroprostheses can come in many different configurations and use a variety of actuation sources. The different forms of actuation influence the behaviour of the overall system in different ways. This research primarily focuses on using a combination of FES and electric motors. These two forms of actuation have different speeds of response, which are governed by their actuation dynamics. In addition, EMD are associated with FES and are modeled as input delays, which can also affect the behaviour of the system. In order to distribute the control effort effectively and prevent uncoordinated movements the effects of the actuator dynamics and EMD must be taken into account. This objective addresses the actuator dynamics by using nonlinear control techniques and modifying them to account for EMD. The control system is capable of taking into account the speed of response of the different actuators used and be more robust to EMD.

- **Objective 3: Compensate for fatigue by incorporating a fatigue-based scaling factor in the control.**

FES elicited muscle contractions result in the rapid onset of muscle fatigue, which further deteriorates the muscle torque generation. This decrease in the torque generation will minimize the effectiveness of the synergy-based control hierarchy. To compensate for the effects of fatigue, a scaling factor has been added to the synergy-based controller.

However, fatigue cannot be measured through a sensor, therefore a model-based estimator is used to estimate the fatigue variable. The completion of this objective further improved the control systems ability to operate despite muscle fatigue, which would result in longer walking durations.

- **Objective 4: Implement the synergy-based control system in experiments on human subjects.**

Throughout this research, innovative and unproven control methods have been developed for gait restoration devices for human use. It is imperative that the methods developed in this research are tested to ensure user safety and prevent injuries. First, this was done numerically by simulating the developed methods on musculoskeletal models that accurately reflect the behaviour of the system to evaluate their effectiveness and ensure that they are safe. Second, this was done experimentally by demonstrating the developed methods on able-bodied subjects and persons with SCI when possible. Preliminary testing of the developed control techniques were conducted on simpler configurations to minimize system complexity, such as a single degree of freedom knee extension and 2 degree of freedom fixed hip configuration. The outcome of this objective is the development of the testbeds and the experimental demonstration of the control systems.

1.3 RESEARCH IMPACT AND SIGNIFICANCE

This research aimed to derive and test control systems for a walking hybrid neuroprosthesis that addresses actuator redundancy, actuator dynamics, EMD, and muscle fatigue. In this dissertation, concepts from human motor control are bridged to nonlinear control theory, by incorporating them in the derivation of a novel control system. More specifically, the concept of muscle synergies was incorporated in the feedforward component of the control scheme. When identified properly, the synergies are capable of solving the actuator redundancy problem by providing a more optimal means of control allocation, while reducing the real-time computation load. However, due to actuator dynamics, EMD, and muscle fatigue, synergies are not enough to provide coordinated movements. Unlike other research efforts

which typically ignore these challenges because they complicate the control development process, this research addresses them in the control development and stability analysis. Actuator dynamics govern the speed of response of actuators, and to date, have only been addressed using ad hoc or inadequate control methods. System response is further complicated when considering EMD, which distorts the timing of control input, and FES-induced muscle fatigue, which diminishes the torque production of muscles and is difficult to compensate for because it is unmeasurable. When unaccounted for actuator dynamics, EMD, and muscle fatigue could cause uncoordinated movement for multi-DOF systems with actuator redundancy. Until now, some solutions to these challenges exist on an individual basis, but are limited by their compatibility. This work is important because unlike other efforts, it addressed these challenges during the control derivation and stability analysis.

The development of more effective control systems for gait restoration devices in this research has the potential to improve the quality of life of persons with mobility disorders. If successful, this research will advance knowledge and understanding of control theory. The use of synergies in real-time controls can be applied to other large complex systems with either actuator redundancy, DOF redundancy, or large online computation loads such as humanoid robots, soft robotics, bipedal/quadruped robots, multi-agent systems, etc. In addition, the synergy concept could be extended to other types of control methods such as model predictive control or optimal control to reduce computational loads. This work improved on existing control techniques by extending the method of dynamic surface control to classes of systems with input delays. Each of these contributions has the potential to lead to advancements in gait restoration devices.

1.4 DISSERTATION OUTLINE

The following list is a breakdown of the chapters of the dissertation and a brief description of each chapter.

- Chapter 2 introduces the musculoskeletal models used in this study including the 4-DOF walking hybrid neuroprosthesis model, a 1-DOF knee extension model, and a

2-DOF fixed hip model used to test proof of concept controllers. This chapter also discusses the testbeds that were used to demonstrate the controllers experimentally. These testbeds include the full walking hybrid neuroprosthesis, a knee extension machine, a fixed hip configuration of the hybrid neuroprosthesis.

- Chapter 3 focuses on solving the actuator redundancy problem created due to the hybrid actuation structure, which uses more than one actuator to actuate a joint; e.g., FES of antagonistic muscle pairs along with an electric motor can be used to rotate a joint. Inspired by the way the human body solves the actuator redundancy problem, a synergy-based controller was developed to deal with the actuator redundancy problem in a real-time controller. Synchronous synergies were extracted using PCA on optimal inputs precomputed from dynamic optimizations and used in a simulation study of walking in a hybrid neuroprosthesis.
- Chapter 4 addressed the EMD issue associated with NMES. This was done by using an EMD-based delay compensation term along with a PID controller to handle the EMD. Experimental results obtained from able-bodied subjects are also presented.
- Chapter 5 addressed the activation dynamics, which are usually neglected, like in the previous chapter. The derivation of a PID-based dynamic surface controller with delay compensation is presented. The DSC method uses lowpass filter dynamics in the error structure to avoid the requirement of acceleration signals. This controller was also validated through experiments on able-bodied subjects and one person with an SCI.
- Chapter 6 combined the three control techniques developed in Chapter 3-5 into one complete control system. In addition, an estimate of the fatigue state is added in the control structure to compensate for the NMES-induced muscle fatigue. The control system was then validated in preliminary experiments on an able bodied subject in the fixed hip configuration.
- Chapter 7 presents an alternative method to develop synergies based on key dynamic postures observed during gait. Unlike the synergies extracted through PCA in Chapter 3, these dynamic postural synergies are designed to produce two key dynamic postures when activated. These dynamic postural synergies are designed to be less

complex and more effective by computing them before the dynamic optimizations. Dynamic optimizations are then performed to compute the optimal synergy activations to produce gait. This chapter also details the finite state machine developed for the walking program and uses two of the synergy-based PID-DSC controllers, one for each leg, working in tandem to produce gait. The results from experimental demonstration of the walking hybrid neuroprosthesis on an able-bodied subject are also presented.

- Chapter 8 is the summary of this research and future work.

2.0 MUSCULOSKELETAL MODELING OF THE HYBRID NEUROPROSTHESIS AND THE EXPERIMENTAL TESTBEDS

Instead of developing and testing the different components of the control system on the full walking system, which can be complex, two additional models are used throughout this dissertation. In all three of these models FES, via surface electrodes, elicits contractions in the stimulated muscle groups that produce a joint torque and depending on the configuration of the hybrid neuroprosthesis a motor may be present at the same joint. The three musculoskeletal models used in this research are:

1. The walking hybrid neuroprosthesis model represents a person walking in a hybrid neuroprosthesis while using an assistive device, like a walker, and is modeled as a 4-DOF system.
2. The knee extension model represents a subject sitting in a leg extension machine while their quadriceps are stimulated. This is modeled as a 1-DOF system and serves as the least complex system for proof of concept tests for real-time control of FES.
3. The fixed hip model represents a person standing on one leg while the other leg, using one side of the hybrid neuroprosthesis, is free to swing without interacting with the ground. This model is more complex than the simple 1-DOF knee extension model because it includes multi-joint movement and actuator redundancy but less complex than the 4-DOF model because it has less DOF and avoids ground contact.

For the experimental demonstration of the developed control systems, two testbeds are used. The first testbed is the hybrid neuroprosthesis and the second testbed is the modified leg extension machine (LEM). These models and testbeds are used in the following chapters as follows:

- Chapters 3 used the walking and fixed-hip model to derive the synergy-based controller and demonstrated it in a simulation study.
- Chapters 4 and 5 developed the control methods to deal with EMD and activation dynamics using the 1-DOF knee extension model and LEM testbed for experimental demonstration of the standalone controllers.
- Chapter 6 derived the full control system for the fixed-hip and walking model and demonstrated it in a simulation study using the fixed-hip model and experimentally demonstrated it using the fixed hip configuration of the hybrid neuroprosthesis.
- Chapter 7 used the walking model to compute the dynamic postural synergies and experimentally demonstrating the full control system for walking used the hybrid neuroprosthesis testbed.

The remainder of this chapter will introduce these models and testbeds in more detail.

2.1 MUSCULOSKELETAL MODELS

2.1.1 Walking Hybrid Neuroprosthesis Model

A person taking one step (half of a gait cycle) using a hybrid neuroprosthesis and a walker, is modeled as a 4-link musculoskeletal system. The hybrid neuroprosthesis uses a hip knee ankle foot orthosis (HKAFO) which provides kinematic constraints on the user, allowing only motion in the saggital plane. In addition, the HKAFOs typically use a motor or wrap spring clutch to lock the knee joint of the stance leg to prevent flexion when standing. This reduces the amount of stimulation needed which decreases muscle fatigue and prolongs walking durations [92]. The stance leg is modeled as one rigid segment simulating the locking of the knee joint and the ankle is fixed to the ground because only half of the gait cycle is considered in this model. The swing leg has a thigh, shank, and foot segment with 3 actuators at each joint: motor and FES for flexion and extension of antagonistic muscle pairs. The trunk dynamics were neglected in the model because the use of a assistive support device like a walker allows the user to stabilize their truck. In addition, the walker is used to help

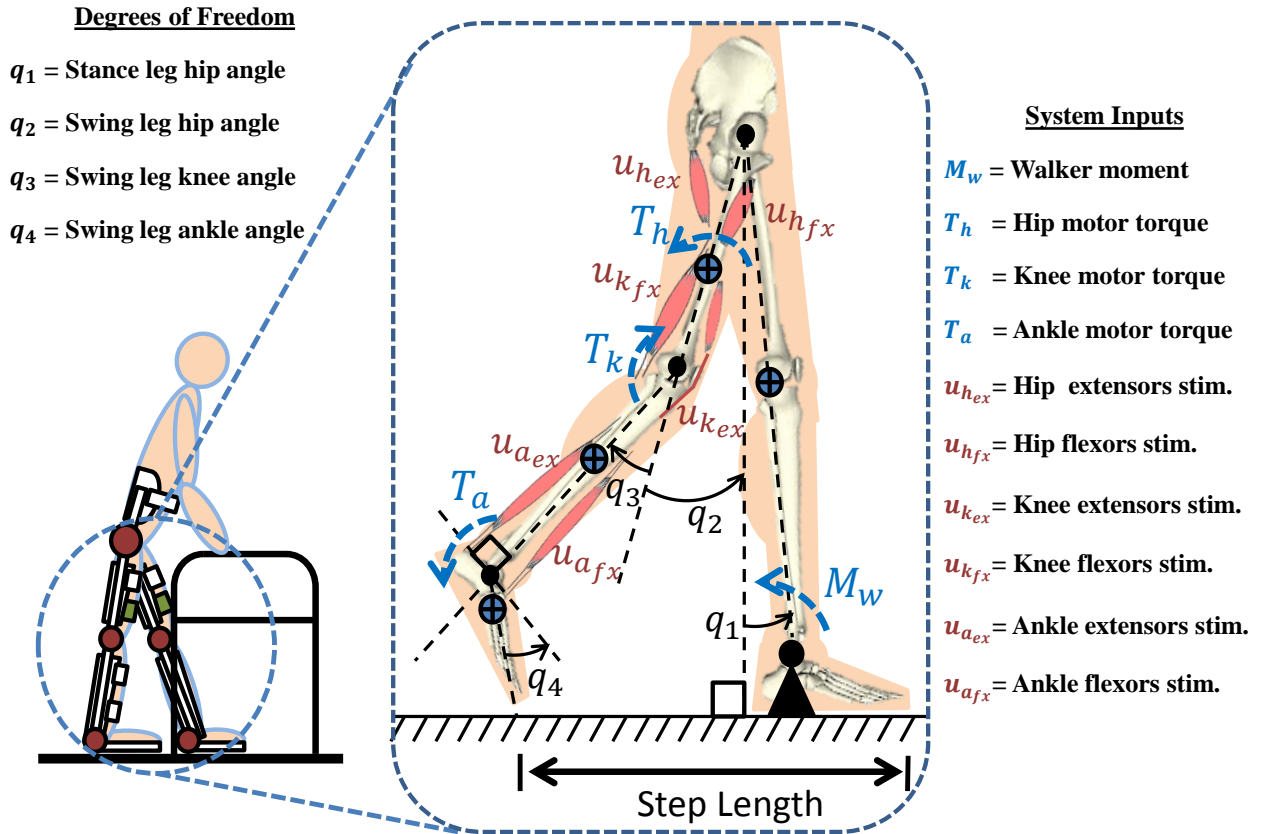


Figure 2.1: A 4-link gait model based of a subject wearing a hybrid neuroprosthesis while using a walker. The model has 10 inputs including FES of 6 muscles (antagonistic hip, knee, and ankle muscle pairs in the swing leg), 3 electric motors acting on each joint of swing leg (T_h, T_k, T_a), and a walker moment acting on the stance leg (M_w). The step length is defined as the distance from stance toe to swing toe.

propel the body forward and also to keep it upright, this is modeled as a moment acting on the stance leg.

The n -DOF lower limb model is given as:

$$M(q)\ddot{q} + C(q, \dot{q})\dot{q} + G(q) + f(q, \dot{q}) + \tau_d(t) + \tau_{ext}(t) = \tau, \quad (2.1)$$

where $q, \dot{q}, \ddot{q} \in \mathbb{R}^n$ are the angular positions, velocities, and accelerations of the leg segments, respectively. In (2.1), $M(q) \in \mathbb{R}^{n \times n}$ is the combined inertia of the hybrid neuroprosthesis and human limbs, $C(q, \dot{q}) \in \mathbb{R}^{n \times n}$ is the centripetal/Coriolis matrix, $G(q) \in \mathbb{R}^n$ is the gravity vector, $f(q, \dot{q}) \in \mathbb{R}^n$ is the viscoelastic vector term that models the passive muscle dynamics, $\tau_{ext} \in \mathbb{R}^n$ is the torque generated at each joint due to contact with the ground, and $\tau_d \in \mathbb{R}^n$ is any unmodeled effects or disturbances in the system. The active torques at the joints are generated by including the musculoskeletal dynamics due to FES [78], an electric motor attached at each joint, and the moment generated by the walker force. The torque term is defined as

$$\tau = b(q, \dot{q})u, \quad (2.2)$$

where $b \in \mathbb{R}^{n \times m}$ is the control gain matrix containing the scaling functions for the m inputs.

Remark. $b(q, \dot{q})$ and $u(t)$ are presented for a gait model with DOF, $n = 4$, and control inputs, $m = 10$. However, without loss of generality, the control development and analysis can be extended to n -DOF system with m inputs.

The model used in this work considers a hybrid neuroprosthesis that uses electric motors and FES via surface electrodes, which non-selectively apply an external voltage potential to a muscle group to generate a contraction. In (2.2), $u(t) \in \mathbb{R}^m$ is defined as

$$u = \left[M_w \quad \mu_{h_{fx}} \quad \mu_{h_{ex}} \quad \mu_{k_{fx}} \quad \mu_{k_{ex}} \quad \mu_{a_{fx}} \quad \mu_{a_{ex}} \quad T_h \quad T_k \quad T_a \right]^T, \quad (2.3)$$

and $b(q, \dot{q})$ is defined as

$$b = \begin{bmatrix} 1 & 0 & 0 & 0 \\ 0 & \psi_{h_{fx}}(q_h, \dot{q}_h) & 0 & 0 \\ 0 & -\psi_{h_{ex}}(q_h, \dot{q}_h) & 0 & 0 \\ 0 & 0 & \psi_{k_{fx}}(q_k, \dot{q}_k) & 0 \\ 0 & 0 & -\psi_{k_{ex}}(q_k, \dot{q}_k) & 0 \\ 0 & 0 & 0 & \psi_{a_{fx}}(q_a, \dot{q}_a) \\ 0 & 0 & 0 & -\psi_{a_{ex}}(q_a, \dot{q}_a) \\ 0 & \kappa_h & 0 & 0 \\ 0 & 0 & \kappa_k & 0 \\ 0 & 0 & 0 & \kappa_a \end{bmatrix}^T, \quad (2.4)$$

where subscripts $i = h, k, a$ stand for the hip, knee, and ankle joints of the swing leg. In (2.4), $\mu_{i_{ex}}, \mu_{i_{fx}}$ are the muscle activations and $\psi_{i_{fx}}, \psi_{i_{ex}}$ are the torque-length and torque-velocity relationships of the flexor and extensor muscles, and T_i is the current input to the motor and the conversion constants (current to torque) of the electric-motor drives is κ_i . The moment due to the walker is denoted as M_w . For this model, hip joint actuation via FES is achieved by stimulating the inner hip muscles (Iliopsoas) for flexion and the Gluteals for extension. Knee joint actuation uses the Quadriceps muscle group for extension and Hamstrings for flexion, and the ankle joint uses the Gastrocnemius for dorsiflexion and Tibialis anterior for plantarflexion.

This 4-link walking model was developed in SimMechanics [MathWorks, USA]. The head, arms, and torso were modeled as a point mass at the hips. The stance leg was modeled as a single link with a fixed knee joint and a pinned ankle joint. The swing leg was modeled with 3-links: thigh, shank, and foot. Each link in the swing leg had redundant actuation, i.e., an electric motor and FES for the muscle flexors and extensors. The influence of the walker was modeled as a moment acting on the stance leg. This moment was used to help propel the body forward and help keep the body stable and upright. The unmodeled effects or disturbances, τ_d , was incorporated by injecting uniformly distributed noise into the 4 joints. The masses and lengths for each limb were taken from anthropometric data [119],

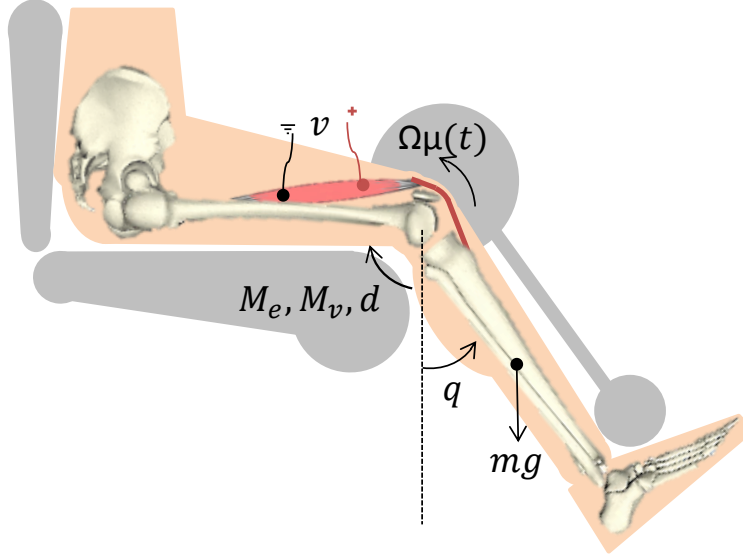


Figure 2.2: Schematic of a subject sitting in the leg extension machine with a knee torque generated via NMES.

and the muscle parameters of a subject with SCI were taken from [26, 78]. The ground reaction force was realized on two contact points: the toe and heel. The model uses a spring-damper system in the vertical direction and a static or kinetic friction model in the horizontal direction when the foot is in contact with the ground. More information on the specifics of this ground reaction model can be found in [39].

2.1.2 Knee Extension Model

The 1-DOF knee-joint dynamics as depicted in Fig. (2.2) are modeled as

$$J\ddot{q} + M_e(q) + M_g(q) + M_v(\dot{q}) + d(t) = \Gamma \quad (2.5)$$

where $q, \dot{q}, \ddot{q} \in \mathbb{R}$ are the angular position, velocity, and acceleration of the knee joint, respectively. In (2.5), J is the moment of inertia of the lower shank, $M_e \in \mathbb{R}$ denotes the elastic effects due to joint stiffness, $M_g \in \mathbb{R}$ denotes the gravitational forces, and $M_v \in \mathbb{R}$ denotes the viscous effects due to the damping in the knee joint. In (2.5), $d(t) \in \mathbb{R}$ denotes

any unmodeled phenomena or disturbances in the system. The torque produced at the knee due to NMES is denoted as $\Gamma \in \mathbb{R}$, and can be represented two ways depending on if the activation dynamics is considered or not. If the Ca^{2+} activation dynamics are not considered Γ is defined as

$$\Gamma = \zeta(q) \eta(q, \dot{q}) u(t - \tau) \quad (2.6)$$

where $\tau \in \mathbb{R}$ denotes the constant input delay caused by electromechanical delays associated with NMES, $\zeta \in \mathbb{R}$ denotes the unknown moment arm function, $\eta \in \mathbb{R}$ denotes the unknown force-length and force-velocity relationships, and u denotes the normalized input due to FES. For the case where activation dynamics is considered Γ is defined as

$$\Gamma = \zeta(q) \eta(q, \dot{q}) \mu(t) \quad (2.7)$$

where $\mu \in \mathbb{R}$ is the muscle activation produced using NMES which is governed by the following first order differential equation

$$\dot{\mu} = -\omega\mu + \omega u(t - \tau), \quad (2.8)$$

where $\omega \in \mathbb{R}^+$ is the muscle activation decay constant. The stimulation applied to the muscle is bounded by two stimulation levels v_{min} and v_{max} to avoid under/over stimulating the muscles. This allows the normalization of the input function $u(t) \in \mathbb{R}$, which is modeled by a piecewise linear recruitment curve [87], as

$$u(t) = sat[v(t)] = \begin{cases} 0 & v < v_{min} \\ \frac{v(t)-v_{min}}{v_{max}-v_{min}} & v_{min} \leq v \leq v_{max} \\ 1 & v > v_{max} \end{cases} \quad (2.9)$$

where $v_{min} \in \mathbb{R}$ is the minimum voltage required to produce an increase in the muscle force and $v_{max} \in \mathbb{R}$ is the minimum voltage at which there is no considerable increase in force or a desired maximum force is achieved. In (2.9), the applied stimulation voltage across the quadriceps muscle is denoted as $v \in \mathbb{R}$.

Property 1. For the linear first order activation dynamics with $u(t) \in [0, 1]$, it can be shown that $\mu(t) \in [0, 1]$. This property also extends to the estimate of the activation dynamics, $\hat{\mu} \in [0, 1]$.

2.1.3 Fixed Hip Model

Consider the dynamics of a swinging leg as shown in Fig. 2.3 are modeled as

$$M(q)\ddot{q} + C(q, \dot{q})\dot{q} + G(q) + f(q, \dot{q}) + d = \Gamma, \quad (2.10)$$

where $q, \dot{q}, \ddot{q} \in \mathbb{R}^n$ are the angular position, velocity, and acceleration of the limb segments, respectively. To simplify the presentation of the model the following subscripts are introduced: 1) i denotes the element for the i^{th} limb, 2) j denotes the type of actuator, i.e., extension muscle ($j = ex$), flexion muscle ($j = fx$), and electric motor ($j = m$), and 3) l denotes the l^{th} parameter for the sets of parameters in the subsequently defined passive dynamics.

In (2.10), $M(q) \in \mathbb{R}^{n \times n}$ is the combined inertia of the semi-powered orthosis and human limbs in the swing phase, $C(q, \dot{q}) \in \mathbb{R}^{n \times n}$ is the centripetal/Coriolis matrix, $G(q) \in \mathbb{R}^n$ is the gravity vector, and $d(t) \in \mathbb{R}^n$ is any unmodeled effects or disturbances in the system such as spasticity. In (2.10), $f(q, \dot{q}) \in \mathbb{R}^n$ denotes the nonlinear viscoelastic passive dynamics of the muscles and can be defined as $f(q, \dot{q}) = M_e + M_v$, where $M_e \in \mathbb{R}^n$ are the elastic muscle effects that account for muscle elasticity under normal functional usage, hyperextension, and hyperflexion and $M_v \in \mathbb{R}^n$ are the viscous effects in the musculoskeletal system. These nonlinear functions were modeled as

$$\begin{aligned} M_{e_i} &= k_{1_i}(q_i - k_{0_i}) + k_{2_i}e^{k_{3_i}q_i} - k_{4_i}e^{k_{5_i}q_i} \\ M_{v_i} &= B_{1_i}\tanh(-B_{2_i}\dot{q}_i) - B_{3_i}\dot{q}_i \end{aligned}$$

where $k_{l_i} (l = 0 \text{ to } 5)$, $B_{l_i} (l = 1 \text{ to } 3) \in \mathbb{R}$ are subject specific model parameters for an i^{th} joint/DOF. The active torques at the joints are generated by including the muscle dynamics due to FES [78] and the current dynamics due to an electric motor attached at each joint. Depending on if the activation dynamics is considered or not the torque term is represented differently. When the activation dynamics are not considered $\Gamma \in \mathbb{R}^n$ is defined as

$$\Gamma \triangleq b(q, \dot{q})\phi(t)u, \quad (2.11)$$

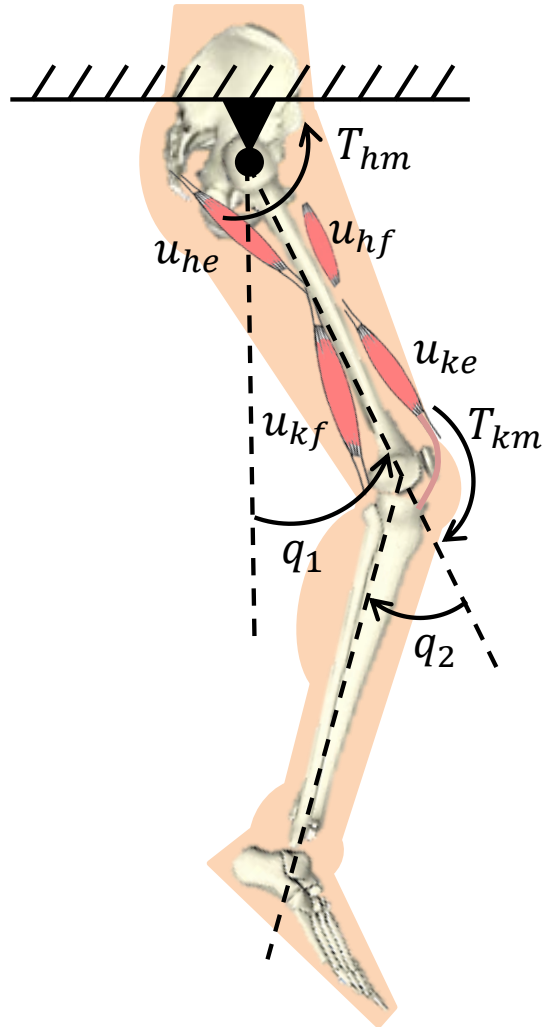


Figure 2.3: A schematic of the fixed hip model with no ground model. The pink muscle bellies labeled u_{he} , u_{hf} , u_{ke} , and u_{kf} indicate the stimulated muscles that produce hip/knee flexion and extension and the torques produced by the motors at both joints are labeled T_{hm} and T_{km} .

The active torque, Γ , is coupled to the normalized control input, $u \in \mathbb{R}^{3n}$, through the intermediate normalized activation vector, $\mu \in \mathbb{R}^{3n}$. The general actuator dynamics for the electric motor and FES are governed by the following differential equation [87]

$$\dot{\mu}_{i_j} = -w_{i_j}\mu_{i_j} + w_{i_j}u_{i_j}(t - \tau_{i_j}), \quad (2.15)$$

where $\tau_{i_j} \in \mathbb{R}^+$ is a known constant EMD and $w_{i_j} \in \mathbb{R}$ is the time constant for the activation variables, μ_{i_j} . The input delay is included out of necessity for FES but is generalized for the electric motors as well, and can be assumed to be zero for the motors. The normalized input $u(t) \in \mathbb{R}^{3n}$ is defined as the saturation function vector that contains μ_{i_j} in (2.15) and is denoted by a piecewise linear function as

$$u = \text{sat}[v] \triangleq \begin{cases} u_{\min} & v < v_{\min} \\ \frac{u_{\max} - u_{\min}}{v_{\max} - v_{\min}}(v - v_{\min}) + u_{\min} & v_{\min} \leq v \leq v_{\max} \\ u_{\max} & v > v_{\max}, \end{cases} \quad (2.16)$$

where $v_{\min}, v_{\max} \in \mathbb{R}^{3n}$ are the minimum/maximum input magnitudes for each actuator (stimulation or motor). Based on (2.15) and (2.16), a linear differential inequality can be developed to show that $\mu \in [u_{\min}, u_{\max}]$. The u_{\min}, u_{\max} values are $[0, 1]$ for muscles because they are unidirectional and $[-1, 1]$ for electric motors because they are bidirectional actuators.

The fatigue dynamics of the muscles, $\phi_{i_j} \in \mathbb{R}$ is generated from the first order differential equation [84]

$$\dot{\phi}_{i_j} = \frac{1}{T_{f_{i_j}}}(\phi_{\min_{i_j}} - \phi_{i_j})\mu_{i_j} + \frac{1}{T_{r_{i_j}}}(1 - \phi_{i_j})(1 - \mu_{i_j}), \quad (2.17)$$

where $\phi_{\min} \in (0, 1)$ is the unknown minimum fatigue constant of a muscle, and $T_f, T_r \in \mathbb{R}^+$ are unknown time constants for fatigue and recovery in the muscle, respectively. Because $\mu \in [u_{\min}, u_{\max}]$ for muscles, it can be shown that $\phi \in [\phi_{\min}, 1]$, where $\phi = 1$ when the muscle is fully rested, and $\phi = \phi_{\min}$ when the muscle is fully fatigued.

2.2 EXPERIMENTAL TESTBEDS

2.2.1 Hybrid Neuroprosthesis

The hybrid neuroprosthesis testbed can be broken down into four primary components: an adjustable orthosis, electric motors, a stimulation unit, and an assistive support device. The orthosis is designed to be adjustable to comfortably fit a wide variety of body types while maintaining the alignment of the joints between the orthosis and subject. Custom motor mount brackets were fabricated to attach the electric motors at the joints of the orthosis. The electric motors [Harmonic Drive LLC, MA, USA] can generate a maximum torque of 50 Nm. The testbed only uses electric motors at the hip joints because it is difficult to use FES to stimulate hip flexors and extensors, as these muscle are not easily accessible using surface electrodes. The knee joint uses a combination of electric motors and FES of the knee flexors and extensors. A RehaStim 8-channel stimulator (Hasomed Inc., DE) was used to generate the current modulated biphasic pulse trains used to elicit muscle contractions. A set of transcutaneous electrodes was placed on the quadricep and hamstring muscle groups. The current modulated pulse train with a frequency of 35 Hz and a 400 μ s pulse width is typically used for all experiments. For the fixed hip model experiments only one side of the exoskeleton is used as shown in Fig. 2.4. For the walking experiments an assistive support device, called an E-Pacter (Rifton, USA), is used for the walking experiments to help the subject maintain balance and propel themselves forward. An xPC target (SpeedGoat, CH) was used to interface with the different sensors and motor drivers and implement the controller in real-time at 1 kHz. The control algorithms were coded in Simulink (MathWorks Inc, USA) and used Simulink's (MathWorks Inc, USA) real-time toolbox software running on a Windows machine (Intel Xeon 3.10 GHz processor). The hybrid neuroprosthesis has a button to control the progression of gait and a emergency stop button to stop all the inputs.

2.2.2 Leg Extension Machine

The leg extension machine (LEM) was modified to hold the subject's leg in an isometric configuration for the system identification experiments or free configuration for the tracking

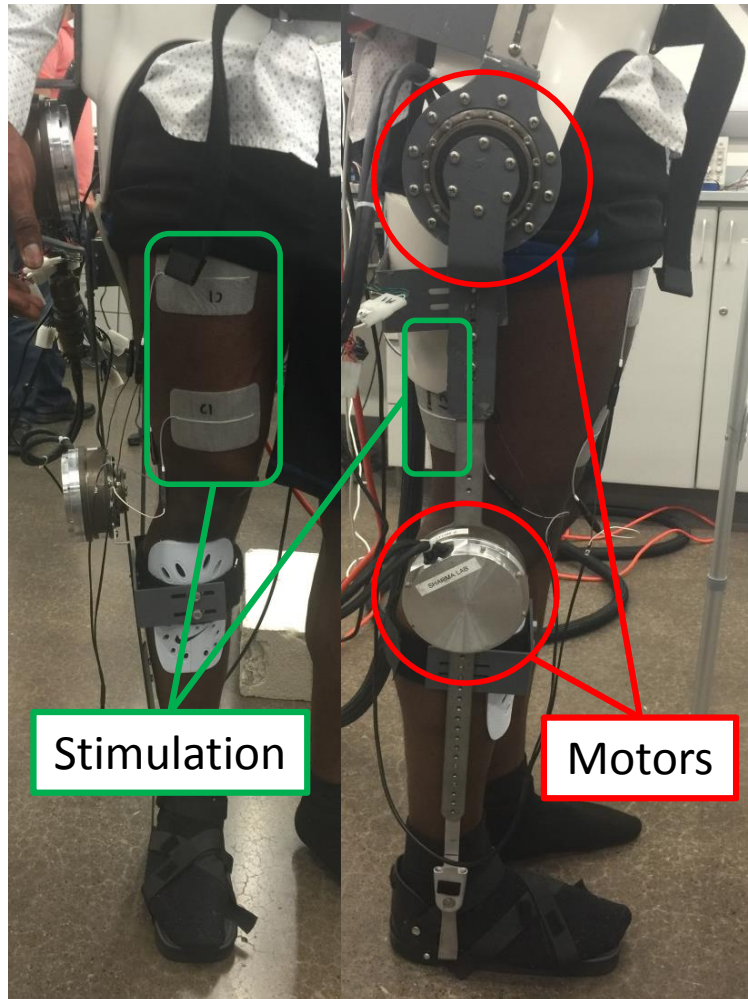


Figure 2.4: The hybrid neuroprosthesis in the fixed hip model configuration. An electric motor is used at the hip and knee joint and FES of the hamstrings and quadriceps muscle group.

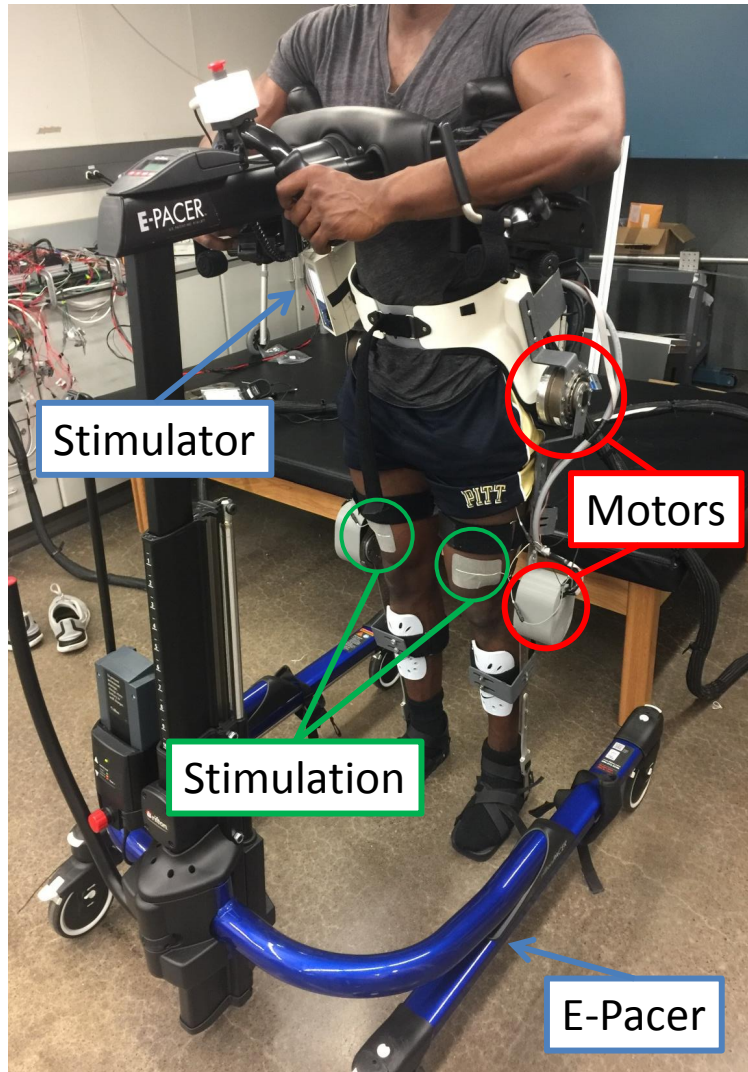


Figure 2.5: The hybrid neuroprosthesis in the walking configuration. An electric motor is used at the hip and knee joints of each leg and FES of the hamstrings and quadriceps muscle group.

experiments. As shown in Fig. 2.6, the LEM was instrumented with a load cell (Omega, USA) to measure the torque generated through NMES elicited contractions and an incremental optical encoder (Hengxiang, CN) with 1024 pulses per revolution resolution to measure the knee joint angle for position feedback. A RehaStim 8-channel stimulator (Hasomed Inc., DE) was used to generate the current modulated biphasic pulse trains used to elicit muscle contractions. A set of transcutaneous electrodes was placed on the quadriceps muscle group. The current modulated pulse train with a frequency of 35 Hz and a 400 μ s pulse width is typically used for all experiments. The QPIDE (Quanser Inc, Ontario Canada) DAQ board was used to interface with the sensors and run the controller in real-time at a control frequency of 1 kHz. The system identification and control algorithms were coded in Simulink (MathWorks Inc, USA) and implemented using the Quarc real-time software (Quanser Inc, Ontario Canada) running on a Windows machine (Intel Xeon 3.10 GHz processor). A emergency stop button is provided for the subjects to stop the stimulation

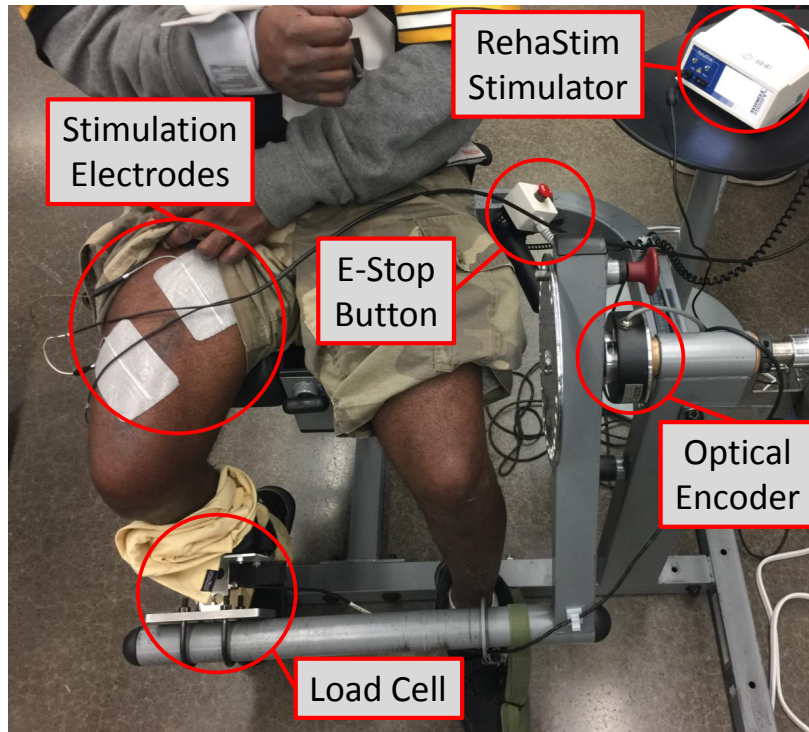


Figure 2.6: The modified leg extension machine (LEM) used for the knee extension experiments. The LEM was instrumented with a load cell to measure force output and incremental encoder to measure the knee joint angle.

3.0 HUMAN MOTOR CONTROL-INSPIRED ARTIFICIAL SYNERGY-BASED CONTROLLER FOR A HYBRID NEUROPROSTHESIS

3.1 INTRODUCTION

The purpose of this research is to derive novel control systems for a hybrid neuroprosthesis. Lyapunov control design methods are used to derive these controllers and guarantee their stability. To this end, the previous chapter presented in detail the models that capture the challenges of real-time control of hybrid neuroprostheses. These challenges include actuator redundancy, electromechanical delays, actuator dynamics, and muscle fatigue. Instead of addressing all of these challenges at once, each challenge is addressed individually to ensure the efficacy of the developed control techniques.

The focus of this chapter is solving the actuator redundancy problem associated with hybrid neuroprosthesis. Inspired by how the cerebellum is hypothesized to use synergies to solve the massive actuator redundancy problem in the human body, I opted to use an artificial synergy-based controls approach. The key contributions of this chapter is the development of an adaptive synergy-based controller for a hybrid neuroprosthesis. Dynamic optimizations were used to produce optimal inputs and gait trajectories, using a subject specific gait model. A PCA-based decomposition technique was used to extract the artificial time-invariant synergies and their activation profiles that are present in the optimal input space. The activation profiles were further adapted online using a gradient-based update law to be used as feedforward control. Then feedback control to the motors was used to improve the performance and robustness of the overall controller. In sections 3.2 and 3.3 the control development and stability analysis is presented. Section 3.4 first implements the new synergy-based controller on the fixed hip model and then on the walking model with

10 actuators (FES of 3 antagonistic muscle pairs, 3 electric motors, and a walker moment). These simulation serve as a proof-of-concept of the muscle synergy-inspired controller and to test its performance.

3.2 CONTROL DEVELOPMENT

3.2.1 Control Objective

The control objective is to track a continuously differentiable desired trajectory $q_d \in \mathbb{R}^n$. The tracking error, $e \in \mathbb{R}^n$, is defined as

$$e = q_d - q. \quad (3.1)$$

To facilitate the control design and stability analysis, the auxiliary error signal $r \in \mathbb{R}^n$ is defined as

$$r = \dot{e} + \alpha e, \quad (3.2)$$

where $\alpha \in \mathbb{R}^+$ is a control gain.

To facilitate the control development, the following assumptions were made:

Assumption 1: The trunk dynamics were neglected in the model because the use of a walker allows the user to stabilize their trunk. However, mass of the head, arm, and torso was incorporated in the model as a point mass located at the hip joint.

Assumption 2: The motion is considered only in the sagittal plane because the HKAFO puts kinematic constraints on motion in planes other than sagittal. The stance leg is modeled as one link because the knee is locked and the stance leg ankle acts as an anchor because only half of the gait cycle is considered in this study. These assumptions allow us to model the kinematics of the lower extremities as a 4-link chain.

Assumption 3: The walker is used to help produce the required propulsion force or M_w . As the user pushes against the walker to pull themselves forward, the resultant force acts as a moment on the hip of the user or the stance leg, M_w . Therefore, the walker moment, M_w , is treated as an input to the system that can be computed by the developed controller.

Assumption 4: First order muscle activation dynamics are ignored to simplify the control design. This avoids the use of control techniques such as integrator backstepping [53] which would add the requirement of additional signals such as the acceleration which is typically unavailable or very noisy [94].

Assumption 5: The unmodeled effects or disturbances, τ_d , are bounded as $|\tau_d| \leq \epsilon_1$ where $\epsilon_1 \in \mathbb{R}^+$ is a constant.

Assumption 6: The control input, u , can be decomposed as $u = Wc_d + u_{loss}$, where the synergies in the matrix, W , are bounded constants and the time-varying activation coefficients, c_d , are bounded signals. The reconstruction error, u_{loss} , is bounded by a constant.

3.2.2 Synergy Extraction

Let $u_d(t) \in \mathbb{R}^m$ be the desired optimal control vector containing desired stimulation and motor voltage levels to achieve the desired optimal trajectory, $q_d(t) \in \mathbb{R}^n$. The dynamics are written in terms of the optimal control inputs and kinematic trajectories as

$$\begin{aligned} M(q_d)\ddot{q}_d + C(q_d, \dot{q}_d)\dot{q}_d + G(q_d) + f(q_d, \dot{q}_d) + \tau_{ext}^*(t) \\ \equiv b(q_d, \dot{q}_d)u_d(t), \end{aligned} \quad (3.3)$$

where τ_{ext}^* is the torque created at each joint due to the ground reaction force when using the optimal inputs, and $b_d = b(q_d, \dot{q}_d)$ is the desired control gain matrix, which is bounded. By using PCA, the possibly correlated inputs, u_d , can be transformed into linearly correlated inputs, c_d , such as

$$u_d = Wc_d(t) + u_{loss}, \quad (3.4)$$

where $W \in \mathbb{R}^{m \times p}$ are the precomputed orthogonal synergies, and $c_d(t) \in \mathbb{R}^p$ are the corresponding time-varying activation coefficients of the synergies. The PCA analysis computes m synergies that account for all the variability of the data. The synergies are ordered such that the first synergy accounts for most of the variance, the second accounts for the second most, and so on. Typically, the rule of thumb is to use the number of synergies, $p < m$, that would account for over 90% of the variability of the data. But since the controller also

has feedback control and adapts online less synergies can be used. After dropping the $m - p$ synergies that account for the least amount of variability in the data, the reconstructed inputs, Wc_d , do not match the optimal inputs, u_d . Therefore, a reconstruction error, denoted as u_{loss} , is introduced in (3.4).

3.2.3 Closed-Loop Error System

The closed-loop error is derived by multiplying the time derivative of (3.2) with $M(q)$ and substituting the dynamics in (2.1) to obtain

$$M\dot{r} = M\ddot{q}_d + C\dot{q} + G + f + \tau_d + \tau_{ext} - bu + M\alpha\dot{e}. \quad (3.5)$$

This expression can be written in the form

$$M\dot{r} = -Cr + \tilde{N} + N_d + \tau_d + \tau_{ext} - bu - e, \quad (3.6)$$

where $\tilde{N} = N - N_d$ and the auxiliary signals $N(e, r)$ and $N_d(t)$ are defined as

$$N = M\ddot{q}_d + C\dot{q}_d + C\alpha\dot{e} + G + f + M\alpha\dot{e} + e,$$

$$N_d = M(q_d)\ddot{q}_d + C(q_d, \dot{q}_d)\dot{q}_d + G(q_d) + f(q_d, \dot{q}_d).$$

The term \tilde{N} in (3.6) can be upper bounded by using the Mean Value Theorem as

$$\|\tilde{N}\| \leq \rho_1(\|z\|) \|z\|, \quad (3.7)$$

where $\rho_1(\|z\|) \in \mathbb{R}$ is a positive monotonic bounded function and $z \in \mathbb{R}^{2n}$ is defined as

$$z = [r^T \quad e^T]^T.$$

Note that the auxiliary signal N_d is equal to the left hand side of the desired muscle synergy dynamics in (3.3), this allows us to substitute $b_d u_d - \tau_{ext}^*$ in for N_d resulting in

$$M\dot{r} = -Cr + \tilde{N} + \tau_d + \tilde{\tau}_{ext} + b_d u_d - bu - e, \quad (3.8)$$

where $\tilde{\tau}_{ext} = \tau_{ext} - \tau_{ext}^*$ is the torque due to the ground reaction force mismatch and can be bounded.

Remark. *Further analysis can be done to show that the bound on $\tilde{\tau}_{ext}$ gets smaller as the position and velocity errors get smaller; i.e., as the tracking errors approach to zero, $\tilde{\tau}_{ext}$ will approach to zero.*

By choosing the control law u as

$$u = W\hat{c} + kr, \quad (3.9)$$

where $\hat{c} \in \mathbb{R}^p$ is the estimate of c_d and $k \in \mathbb{R}^{m \times n}$ is the feedback gain that is chosen to only influence the electric motors. The estimate of the synergy activation coefficient updates according to the following gradient based update law with the projection algorithm

$$\dot{\hat{c}} = \text{proj}(\dot{c}_d + \Gamma W^T b_d^T r), \quad (3.10)$$

where $\Gamma \in \mathbb{R}^{p \times p}$ is a symmetric positive definite learning rate gain matrix. The projection algorithm imposes an upper and lower bound on \hat{c} , which is used in the stability analysis. More details of this algorithm can be seen in [53]. The purpose of the adaptation in the activation coefficient is to improve the feedforward component after reconstruction loss and to overcome any system uncertainties. After using (3.4) and (3.9), (3.8) becomes

$$M\dot{r} = -Cr + \tilde{N} + \tau_d + \tilde{\tau}_{ext} + b_d u_{loss} + b_d W\tilde{c} + \tilde{b}W\hat{c} - bkr - e, \quad (3.11)$$

where $\tilde{c} \in \mathbb{R}^p$ and $\tilde{b} \in \mathbb{R}^{n \times m}$ are defined as

$$\tilde{c} = c_d - \hat{c}, \quad \tilde{b} = b_d - b.$$

Using the Mean Value Theorem, Assumption 5, and the property of the projection algorithm the following terms can be bounded as

$$\|\tilde{b}\| \leq \rho_2(\|z\|) \|z\|, \quad \|W\hat{c}\| \leq \epsilon_2, \quad \|\tilde{\tau}_{ext} + b_d u_{loss}\| \leq \epsilon_3, \quad \|\tilde{c}\| \leq \delta, \quad (3.12)$$

where $\rho_2(\|z\|) \in \mathbb{R}$ is a positive monotonically increasing bounded function and $\epsilon_2, \epsilon_3, \delta \in \mathbb{R}^+$ are constants.

3.3 STABILITY ANALYSIS

Theorem 1. *The controller designed in (3.9) and (3.10) ensures semi-global uniformly ultimately bounded tracking provided that the following gain conditions are met:*

$$K_{min} > \frac{(\rho_1(\|z\|) + \epsilon_2 \rho_2(\|z\|))^2}{2}, \quad \gamma_{min} \{bk - \gamma I\} > 0,$$

where $\gamma_{min} \{\cdot\}$ denotes the minimum eigenvalue of a square matrix and $K_{min} \in \mathbb{R}^+$ is a subsequently defined constant.

Proof: A continuously differentiable Lyapunov candidate $U(z, t) \in \mathbb{R}$, is defined as

$$U = \frac{1}{2}e^T e + \frac{1}{2}r^T M r + \frac{1}{2}\tilde{c}^T \Gamma^{-1} \tilde{c}. \quad (3.13)$$

The Lyapunov candidate U can be upper and lower bounded as

$$\lambda_1 \|z\|^2 \leq U \leq \lambda_2 \|z\|^2 + \Upsilon, \quad (3.14)$$

where $\Upsilon, \lambda_1, \lambda_2 \in \mathbb{R}^+$ are constants. Taking the time derivative of $U(z, t)$ and using (3.2) and (3.11) results in

$$\begin{aligned} \dot{U} = & e^T (r - \alpha e) + \frac{1}{2}r^T \dot{M}r + \tilde{c}^T \Gamma^{-1} (\dot{c}_d - \dot{\hat{c}}) \\ & + r^T \left(-Cr + \tilde{N} + \tau_d + \tilde{\tau}_{ext} + b_d u_{loss} + b_d W \tilde{c} + \tilde{b} W \hat{c} - bkr - e \right). \end{aligned}$$

After using the skew-symmetry property [53] and canceling out the like terms, the previous equation becomes

$$\dot{U} = -\alpha e^T e - r^T bkr + \tilde{c}^T \Gamma^{-1} (\dot{c}_d - \dot{\hat{c}}) + r^T \left(\tilde{N} + \tau_d + \tilde{\tau}_{ext} + b_d u_{loss} + b_d W \tilde{c} + \tilde{b} W \hat{c} \right).$$

Using the update law in (3.10) yields

$$\dot{U} = -\alpha e^T e - r^T bkr + r^T \left(\tilde{N} + \tau_d + \tilde{\tau}_{ext} + b_d u_{loss} + \tilde{b} W \hat{c} \right).$$

The previous equation can be bounded using (3.12) and Assumption 4 to get

$$\dot{U} \leq -\alpha e^T e - r^T bkr + \|r\| [(\rho_1(\|z\|) + \epsilon_2 \rho_2(\|z\|)) \|z\| + \epsilon_1 + \epsilon_3].$$

Using nonlinear damping to separate the terms and further bounding results in

$$\dot{U} \leq -\alpha e^T e - r^T (bk - \gamma I) r + \frac{(\rho_1(\|z\|) + \epsilon_2 \rho_2(\|z\|))^2 \|z\|^2}{2\gamma} + \frac{(\epsilon_1 + \epsilon_3)^2}{2\gamma},$$

where $\gamma \in \mathbb{R}^+$ is a constant. This expression can be bounded as

$$\dot{U} \leq - \left(K_{min} - \frac{(\rho_1(\|z\|) + \epsilon_2 \rho_2(\|z\|))^2}{2\gamma} \right) \|z\|^2 + \frac{(\epsilon_1 + \epsilon_3)^2}{2\gamma}, \quad (3.15)$$

where K_{min} is defined as $K_{min} = \min \{ \alpha, \gamma_{min} \{ bk - \gamma I \} \}$. Consider a set \mathbb{S} defined as

$$\mathbb{S} \triangleq \left\{ z(t) \in \mathbb{R}^{2n} \mid \|z(0)\| < \sqrt{\frac{\lambda_1}{\lambda_2} \left(\bar{\rho}^{-2} \left(\sqrt{2\gamma K_{min}} \right) - \frac{\Upsilon}{\lambda_1} \right) - \frac{B\lambda_2}{\delta}} \right\},$$

where $\bar{\rho}$ is a positive monotonically increasing bounded function defined as $\bar{\rho} = \rho_1(\|z\|) + \epsilon_2 \rho_2(\|z\|)$, and $B \in \mathbb{R}^+$ is a subsequently defined constant. In \mathbb{S} , $A(\|z\|)$, which is defined as $A(\|z\|) = K_{min} - \frac{(\rho_1(\|z\|) + \epsilon_2 \rho_2(\|z\|))^2}{2\gamma}$, is bounded by a constant $\delta \in \mathbb{R}^+$ as

$$A(\|z\|) \geq \delta.$$

Adding and subtracting $\frac{\delta}{\lambda_2} \Upsilon$ to (3.15) and using (3.14), (3.15) becomes

$$\dot{U} \leq -\frac{\delta}{\lambda_2} U + B, \quad (3.16)$$

where $B = \frac{\delta}{\lambda_2} \Upsilon + \frac{(\epsilon_1 + \epsilon_3)^2}{2\gamma}$. (3.16) can be integrated with respect to time to obtain

$$U(z, t) \leq U(0) e^{-\frac{\delta}{\lambda_2} t} + \frac{B\lambda_2}{\delta} \left(1 - e^{-\frac{\delta}{\lambda_2} t} \right). \quad (3.17)$$

From (3.17) it is evident that $U(z, t)$ decays exponentially to a bound $\frac{B\lambda_2}{\delta}$ which can be minimized using the control gains. Therefore, it can be concluded that $U \in \mathcal{L}_\infty$ and the states $e, r \in \mathcal{L}_\infty$. Further analysis can be done to show that the $\|z\|$ decays to the ball of radius $\sqrt{\frac{B\lambda_2}{\delta\lambda_1}}$. By Theorem 4.18 in [53], we can conclude that the origin of z is semi-global uniformly ultimately bounded (SGUUB). ■

3.4 SIMULATIONS

3.4.1 Fixed Hip Model

This newly developed controller was tested in a simulation study on the 2-DOF fixed hip model that does not include actuator dynamics. The fixed hip model represents the gait cycle for one leg fixed at the hip joint. Only the hip and knee joints are actuated in this model (i.e., the ankle joint is fixed) and only motion in the sagittal plane is considered. There are six actuators in total; FES induced flexion and extension and an electric motor at each joint. A schematic of the model can be seen in Fig. 2.3. Before the controller is tested in simulations, dynamic optimizations were performed on the fixed hip model to compute the optimal inputs to track a desired trajectory.

3.4.1.1 Dynamic Optimizations

The musculoskeletal model and parameters used in the simulations were taken from [78] for a person with SCI. Optimizations were conducted to compute optimal inputs in order to track gait data taken from [119] for one complete gait cycle. For the optimizations, the convex cost function's objective is to minimize the position and velocity error, and minimize the input to the system, i.e. the amount of stimulation and motor torque used, and is defined as

$$\Pi = \int_{t_0}^{t_f} (e(t)^T Q_1 e(t) + \dot{e}(t)^T Q_2 \dot{e}(t) + u(t)^T R u(t)) dt$$

where $Q_1 \in \mathbb{R}^+$ is a weight on the position tracking error, $Q_2 \in \mathbb{R}^+$ is the weight on the velocity tracking error, and the matrix $R \in \mathbb{R}^{3n \times 3n}$ is a positive-definite matrix of weights on the input vector. PCA was then performed to reduce the dimensionality of the inputs by extract the principal components, c_d , and transformation matrix, W . For more details on the dynamic optimization used to compute optimal inputs, see [92]. The principal components that account for little variance in the data were disregarded. For this simulation study, the dimensions were reduced from 6 to 3 variables while still accounting for about 94% of the variance as can be seen in Fig. 3.1.

3.4.1.2 Simulation Results

The controller was demonstrated on a fixed-hip model for five steps. A muscle fatigue model was included in the simulations to test the controllers ability to deal with the onset of muscle fatigue. The fatigue is modeled as a first order differential equation [84,94]. The simulation results can be seen in Figs. 3.2-3.5.

The reduced number of principal components are sufficient to produce limb movements. However, their performance would begin to degrade as the muscles begin to fatigue, as seen in Fig. 3.5, and variations in the cyclic patterns occur, such as changes in the initial conditions before each step. Since the adaptation law and feedback component are error-based, as the performance degrades due to fatigue or any other effects, they react to the increase in error and modify the inputs to improve the performance. This is evident in Fig. 3.4, where the amount of feedback input increased after the first step at $t = 1$ because the feedforward inputs, in Fig. 3.3, were not sufficient enough to produce the following steps. The controller is capable of tracking the desired trajectory with just three principal components in the feedforward control, but with the adaptive and feedback control added, the performance is improved as can be seen in Fig. 3.2. It is to be noted that with the optimization, the stimulation inputs are constrained to be positive. However, after reducing the dimensionality of the principal components and reconstructing the input data, the characteristics that maintained the non-negative stimulation input were lost with the dropped principal components, evidence of this can be found in Fig. 3.3. Because the muscles are uni-directional actuators, negative stimulation inputs were set to zero.

3.4.2 Walking Hybrid Neuroprosthesis Model

The newly developed controller in (3.9) was simulated on a 4-link rigid body gait model presented in chapter 2. Before the controller is tested in simulations, dynamic optimizations were performed on a 4-link walking model developed in SimMechanics to compute the optimal trajectories and inputs.

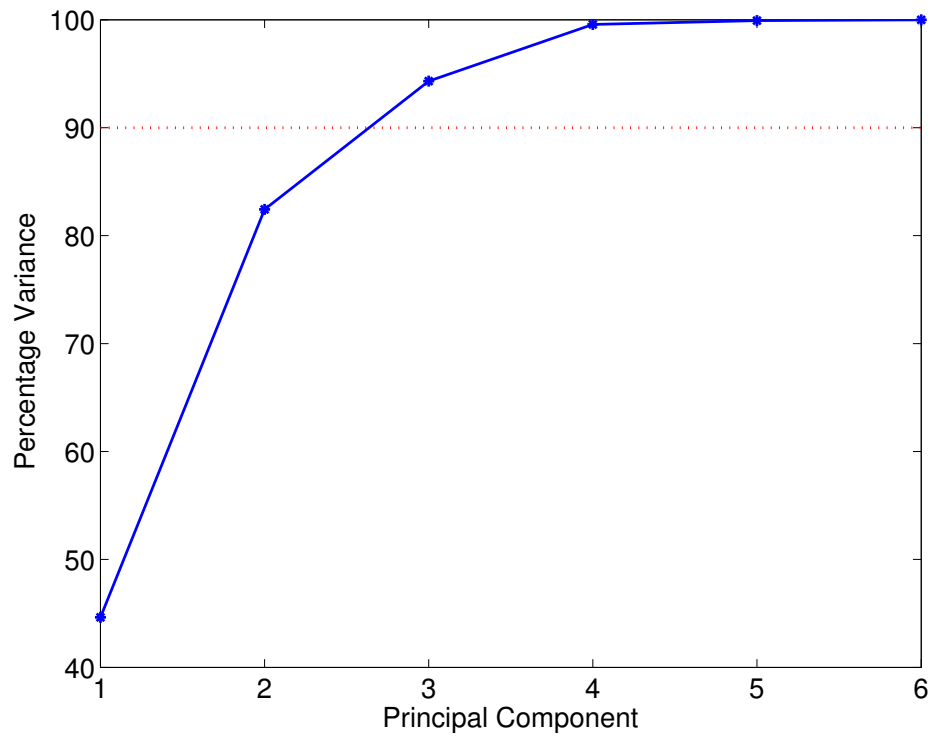


Figure 3.1: This graph shows how much variance is accounted for based on the number of principal components used. Typically, the number of principal components that account for over 90% of the variance is sufficient for decreasing dimensionality while being able to reconstruct the ideal input data to over a 90% match.

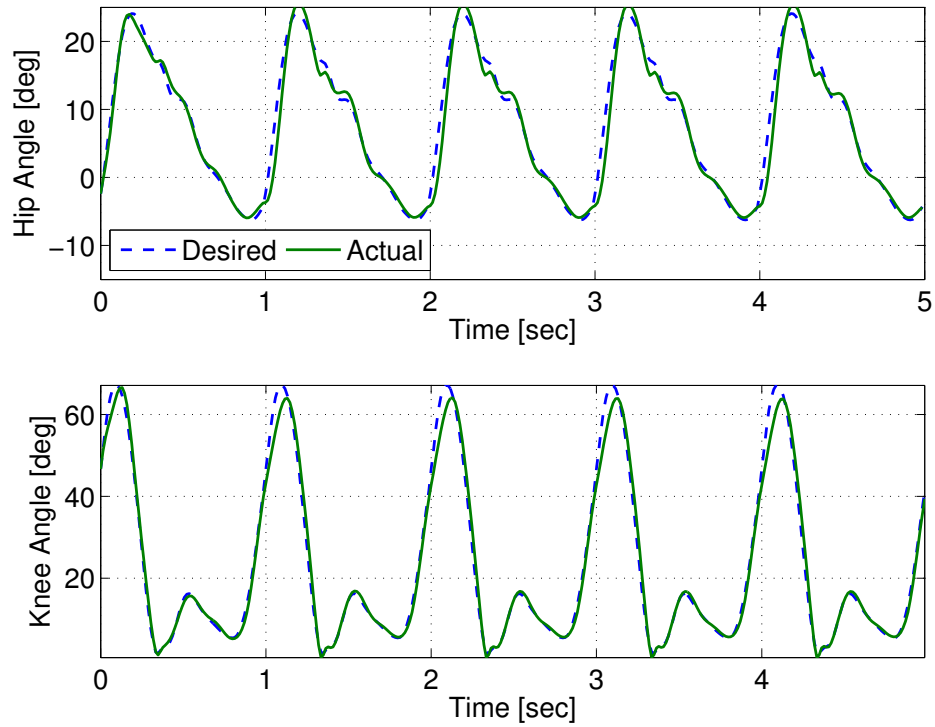


Figure 3.2: The joint angles resulting from simulating low dimensional controller. The top plot shows the desired and actual hip angle and the bottom plot shows the desired and actual knee angle, each for five steps.

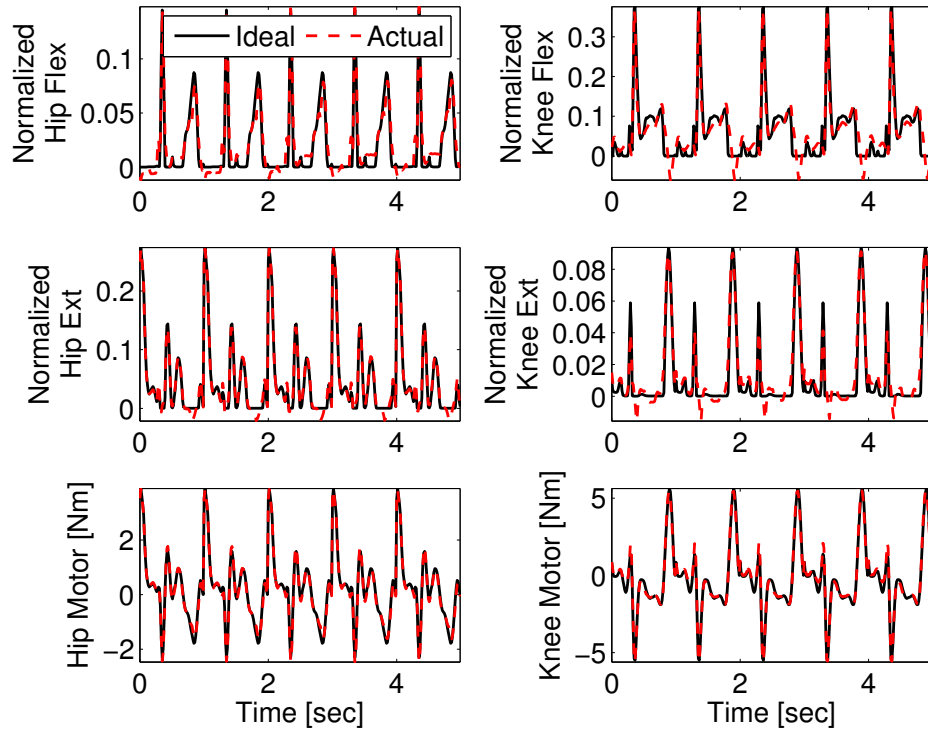


Figure 3.3: These plots show the ideal inputs generated from optimizations and the actual inputs resulting from using only 3 principal components with the adaptive update law. Notice that the actual inputs for each muscle u_{he} , u_{hf} , u_{ke} , and u_{kf} at some instances were negative. These instances were replaced with zeros because the muscles are uni-directional actuators.

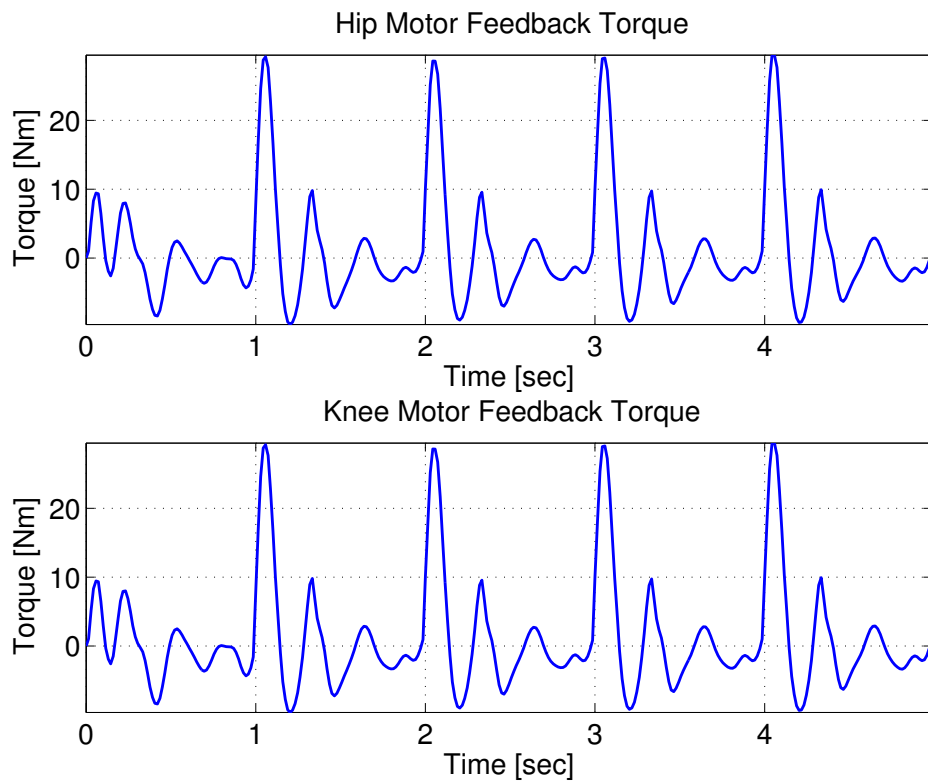


Figure 3.4: This figure shows the motor inputs from feedback control for the two motors.

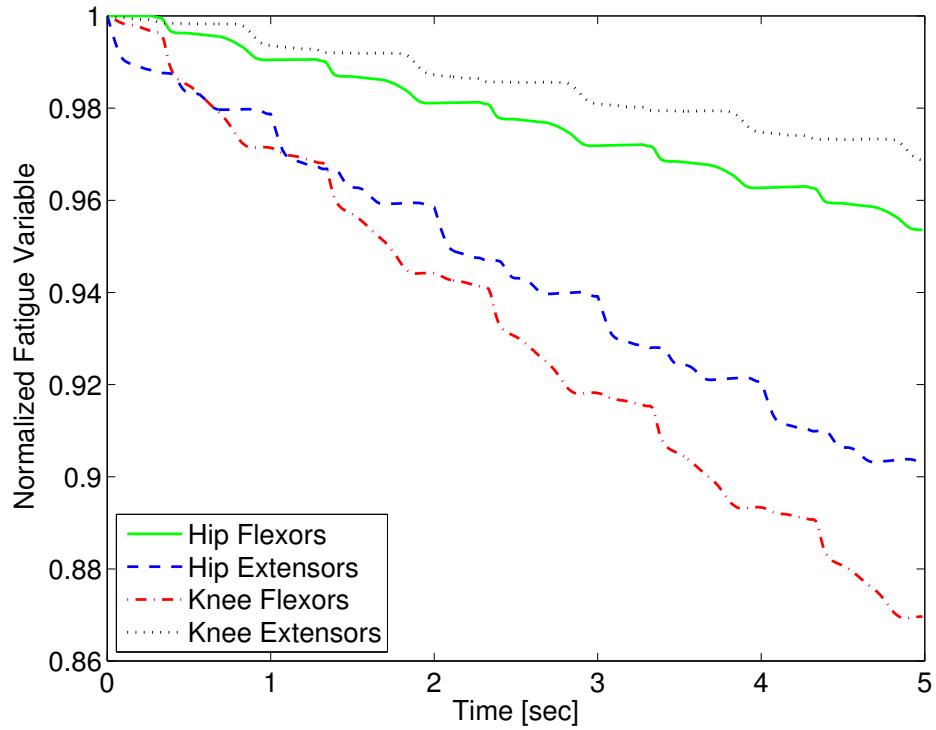


Figure 3.5: The normalized fatigue variable for the four muscles: hip and knee flexors/extensors. The fatigue variable ranges from zero to one, which corresponds to full fatigue and no fatigue, respectively.

3.4.2.1 Dynamic Optimizations

Dynamic optimization was used to compute optimal subject specific gait trajectories and inputs [56,92]. In these optimizations, the model was only restricted to achieve a certain step size and step duration (0.4 meters in .75 seconds). The optimization computes the inputs that minimize a user-defined cost function. One of the benefits of dynamic optimization is that it can account for constraints, such as a limited range of movement and strength of a user. These constraints are accounted for by constraining the optimization to a subject specific dynamic model. Rather than tracking able-bodied gait data, which may be suboptimal when applied in the case of subjects with paraplegia [25,26,75,78,80] and may result in over stimulation of the muscles and quicken the onset of FES induced muscle fatigue, the dynamic optimizations are used to compute subject specific optimal trajectories. The following cost function and constraints were used to compute the optimal control inputs and joint angle trajectories:

$$\begin{aligned} \min_u \quad & \Pi = \int_{t_o}^{t_f} u^T Q u \, dt \\ \text{subject to:} \quad & M(q) \ddot{q} + C(q, \dot{q}) \dot{q} + G(q) + f(q, \dot{q}) + \tau_{ext}(t) = b(q, \dot{q})u \\ & q(t_o) = q_o \\ & q(t_f) = q_f \\ & u \in [u_l, u_u] \end{aligned}$$

where $Q \in \mathbb{R}^{m \times m}$ is a symmetric positive definite weight matrix, q_o and q_f are the initial and final joint angle vectors corresponding to the user-defined step length, and the lower and upper bound on the inputs are defined as u_l and u_u . These bounds allow for the computation of an optimal solution while considering the physical constraints of the system, such as the maximum torque a motor can produce or the maximum amount of force a user can produce when using a walker. The inputs to the system are bounded by realistic values. The walker moment was constrained to 100 Nm and the motors torques are constrained to 40 Nm. The optimizations were run with 75 grid points for each control input in u . The inputs were interpolated using a linear interpolation. A 2nd order Heun method with a step size of 1 ms was used for numerical integration. This smaller step size was used to prevent numerical

divergence that may occur due to the harsh nonlinearities in the dynamics (e.g., ground reaction model and passive muscle models, $f(q, \dot{q})$), which diverge around hyperflexion and hyperextension.

The optimization results are shown in Figs. 3.6 & 3.7. Fig. 3.6 shows the optimal joint angle trajectories. Fig. 3.7 shows the optimal control inputs. The optimal contributions from the motor and FES can be adjusted by tuning the weights in the cost function.

Although 3 synergies are needed to reconstruct the optimal inputs to 90% of the variance as seen in Fig. 3.8, only 2 synergies were used since the controller also includes adaptation and feedback control. The two synergies and their activation profiles extracted through PCA can be seen in Fig. 3.9. Note that the scaling factors in the synergies on the left and the time-varying activation coefficients on the right can have negative values. This makes it harder to interpret what influence each synergy has on the system, but it is unavoidable when PCA is used. Also in the optimizations, the inputs to the stimulation channels are constrained to be positive, but after extracting the synergies, this property was lost. This results in negative stimulation values which are not applicable with FES because muscles are unidirectional actuators. Therefore, when implementing the controller any negative stimulation inputs were set to zero.

3.4.2.2 Simulations Results

To explore the efficacy of the controller, the simulations were done with four cases. Case 1 considered the synergies as the feedforward component but with no adaptation; i.e., Wc_d in (3.4). Case 2 considered the synergies with adaptation; i.e., $W\hat{c}$ with the adaptive law in (3.10). Case 3 considered both the synergies with adaptation and feedback control; i.e., (3.9) and (3.10). Case 4 considered the full optimal inputs computed in the optimizations with feedback control. Only the motors and walker moment were used as effectors to provide feedback. The control gains used in the cases that included feedback control were $k = 10$ and $\alpha = 100$. In the two cases where adaptation was present, the learning rate used for the two synergies were 0.0175 and 0.001. The results are shown in Figs. 3.10-3.14. The root mean squared error (RMSE) for the 4 joints for each case can be seen in Table 3.1. Of all the cases, the third and fourth cases were found to provide the best performance. In the first case, the

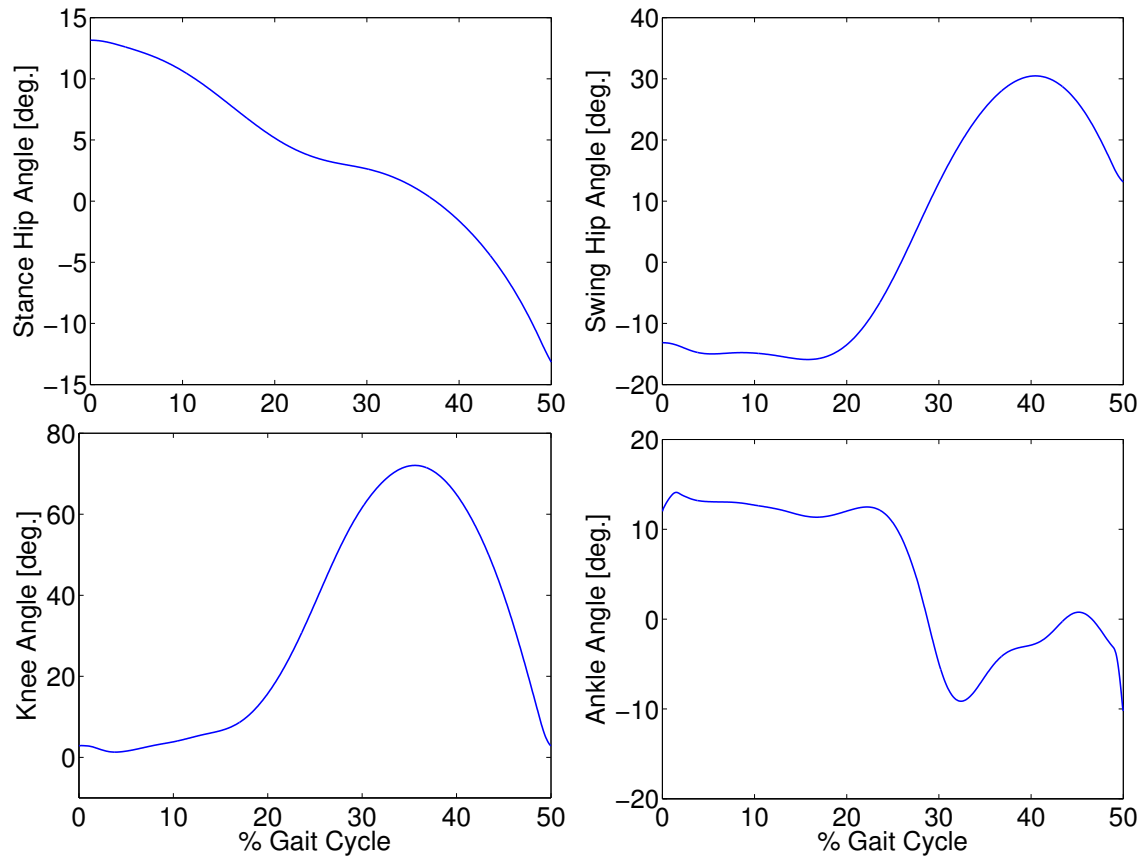


Figure 3.6: Optimal gait trajectories for a step size of 0.4 meters in 0.75 seconds.

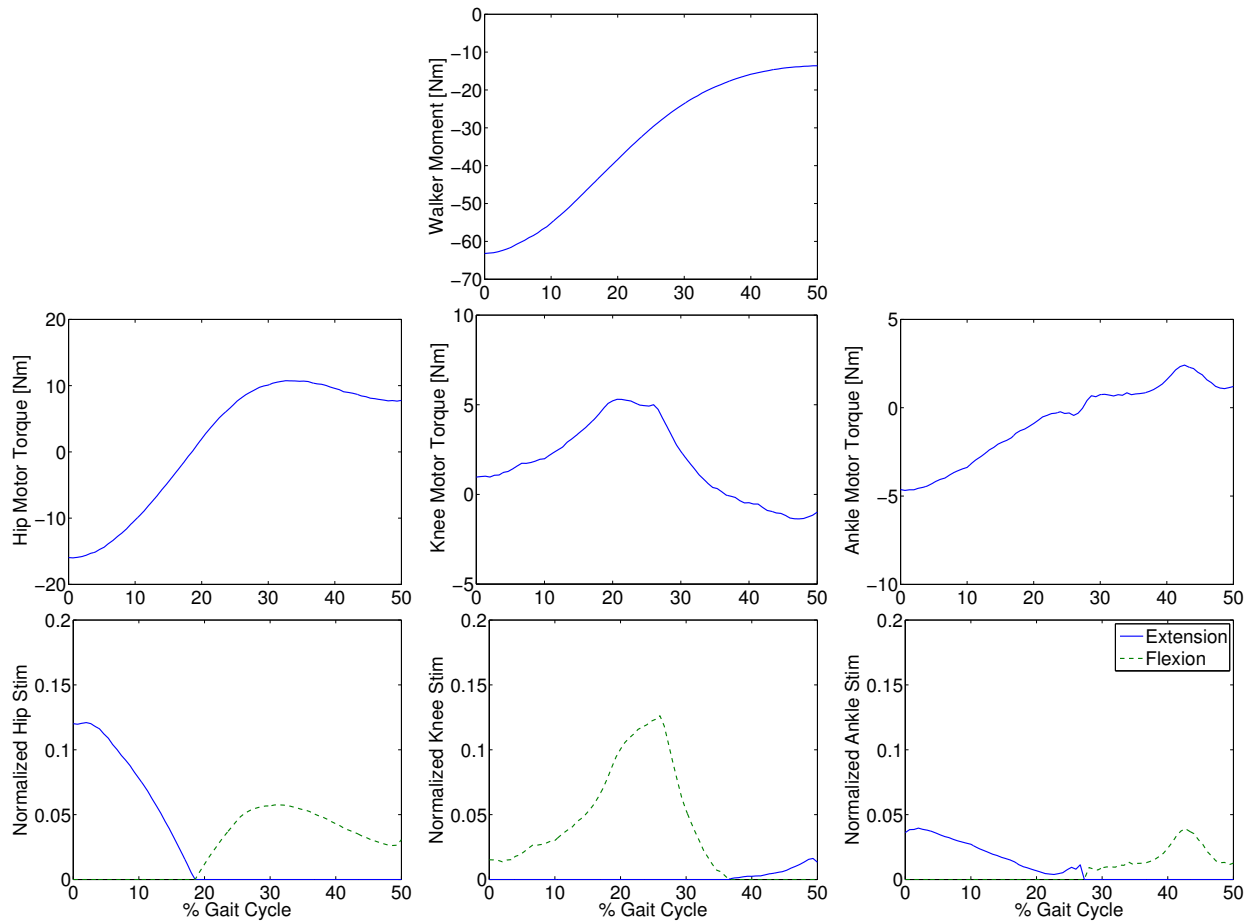


Figure 3.7: Optimal inputs to the walker moment, electric motors, and stimulation channels to reproduce the optimal gait trajectories.

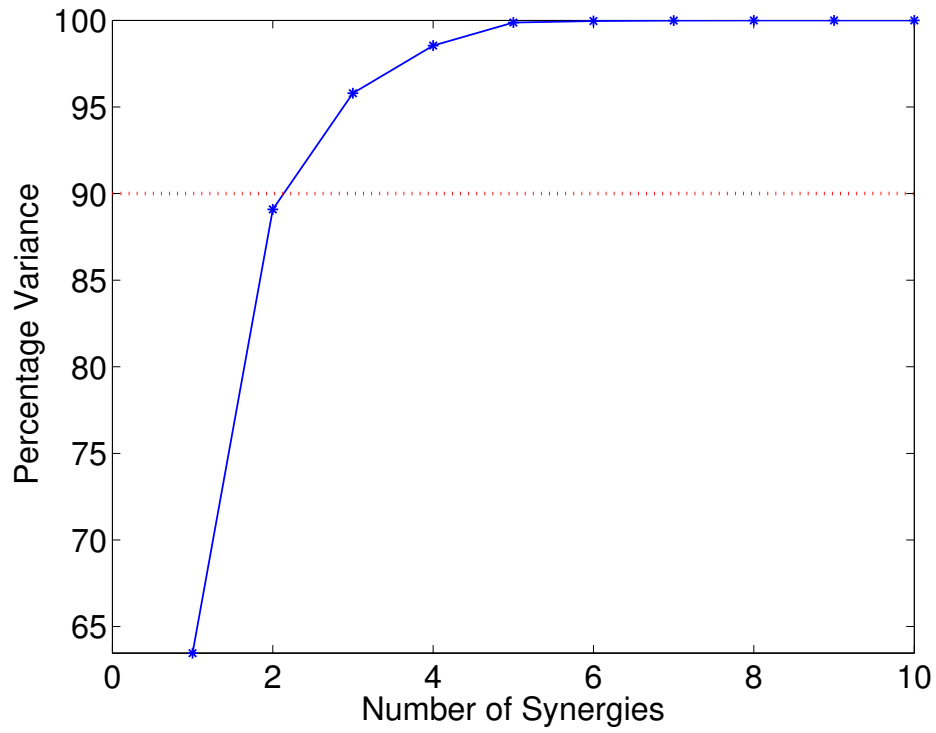


Figure 3.8: This plot indicates how much of the data variability would be accounted for based on the number of synergies considered. Rule of thumb would indicate using 3 synergies, but since the controller is not solely dependent on the feedforward component less synergies can be used.

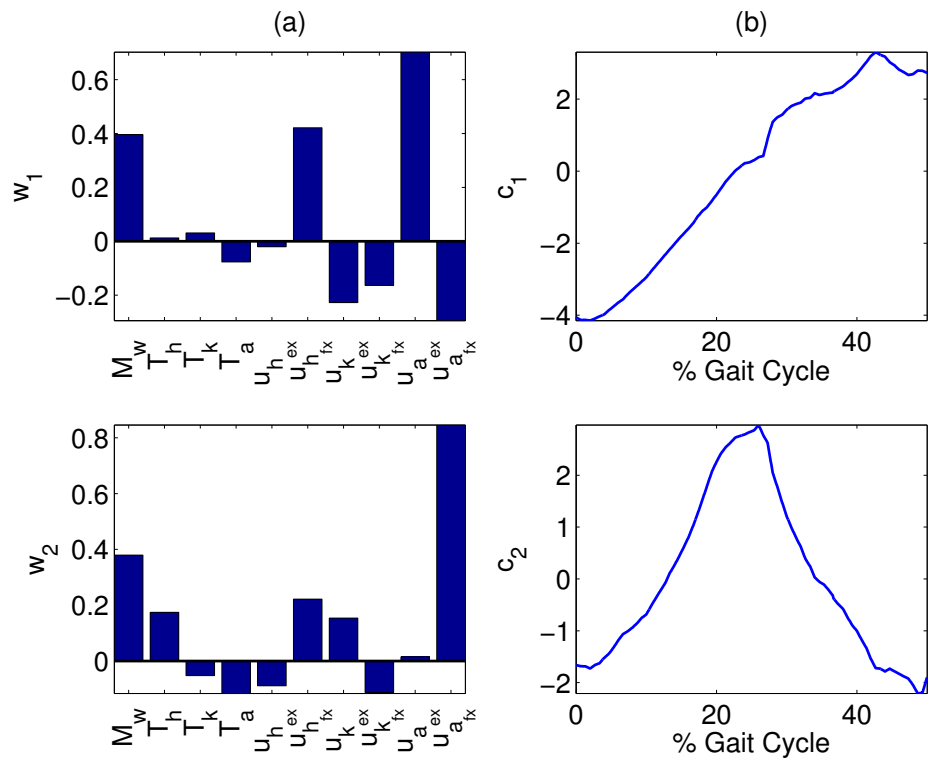


Figure 3.9: (a) Two synergies, w_1 and w_2 . (b) The corresponding time-varying activation coefficients, c_1 and c_2 , of synergies, w_1 and w_2 .

feedforward component provides just enough control input to produce the movements but fails to clear the ground to complete the step. This is because the toe makes contact with the ground model early and begins to drag. In the second case, the swing leg joint angles match the desired profiles better and almost completes the walking step but the swing foot does not reach the floor in the allotted time of .75 seconds. In the third and fourth cases, the trajectories match the desired profiles almost perfectly.

A muscle synergy approach can be useful for engineered systems with redundancy in effectors. For example, the research by Rugey et al. [20] mentions the usefulness of muscle synergies in FES-based systems. The muscle synergy principle has also been suggested as a hierarchical control framework for redundant manipulators [5, 109], brain machine interface-based control [116], and for the design and control of a humanoid robotic hand [13, 16, 44, 85]. In our proposed adaptive control scheme, we showed that the synergy-based approach can be modified to provide a lower dimensional feedforward controller and combined with a feedback controller to control a hybrid walking neuroprosthesis.

As shown in the simulations, the new controller (Case 3) performs as expected only when both the adaptive feedforward and feedback components were active. However, in Case 1, when two synergies were used alone, the key characteristics of the optimized gait was reconstructed, but the inputs from the two synergies were not enough to clear the ground and complete a full step as can be seen in Fig. 3.14. This was likely caused by the reconstruction error, u_{loss} in (3.4), due to the PCA decomposition. Evidence of this can be seen by comparing the optimal inputs in Fig. 3.7 and the feedforward inputs in Case 1, as shown in Fig. 3.11. To overcome the reconstruction error due to the synergy decomposition, we proposed adding an adaptive component and a feedback component to the synergy controller. In Case 2, the adaptive synergies provided sufficient control inputs to complete the walking step as well as enable the foot to clear the ground during the swing phase but the swing knee joint angle does not end at zero as seen in Fig. 3.14. This is evident in Fig. 3.10, near the 40% gait cycle region, where the swing hip, knee, and ankle profiles showed improved tracking of the desired profile.

In Case 3, the feedback control to the motors further improved the performance and the actual gait trajectories tracked the desired profile almost perfectly. In this case, the adaptive

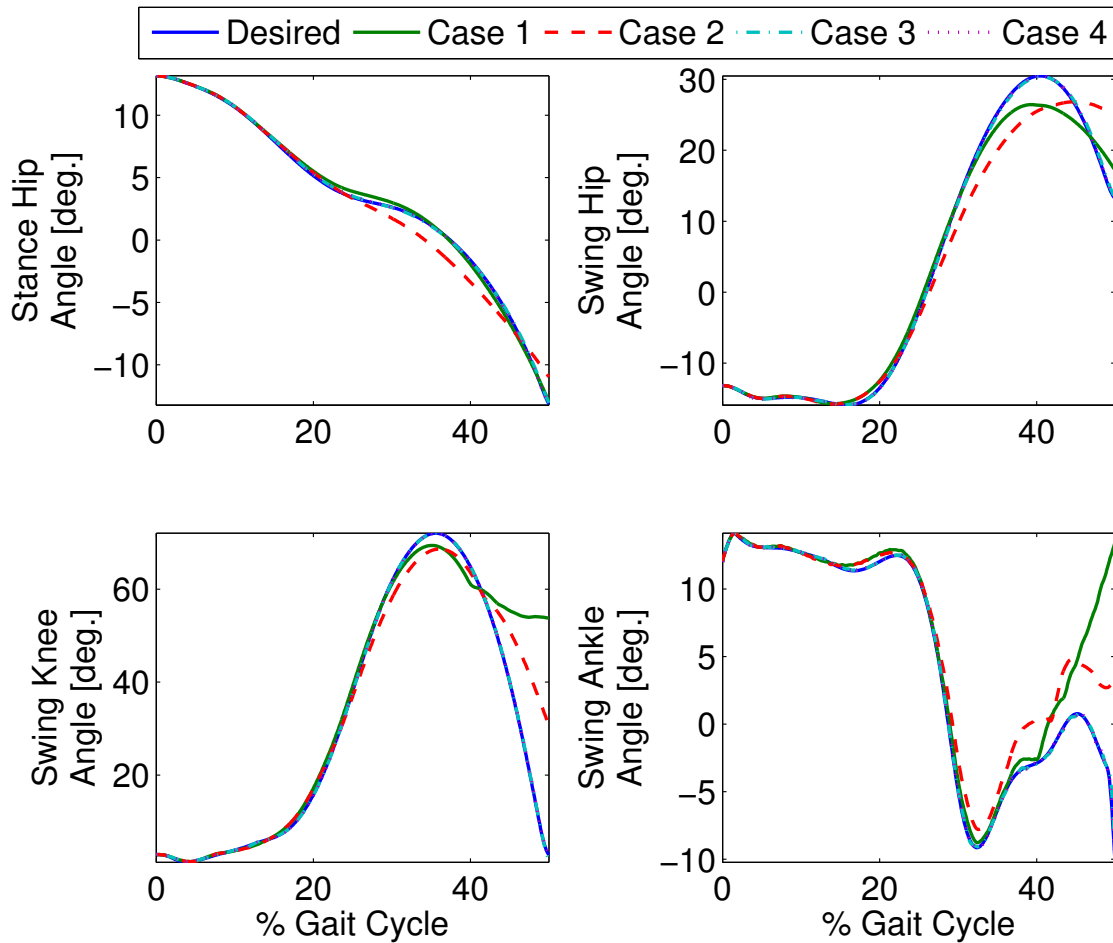


Figure 3.10: Four cases for gait control using a hybrid neuroprosthesis. Case 1 only used the feedforward synergies, Case 2 used the adapted feedforward synergies, Case 3 considered both the adapted feedforward synergies and feedback control, and Case 4 used the full optimal inputs and feedback control. Note that the profile from the third and fourth cases almost perfectly overlaps the desired profiles.

Table 3.1: The root mean squared (RMS) error for the four simulated cases. Case 3 which had 2 synergies and feedback and Case 4 which had full optimal feedforward and feedback had the smallest RMS errors, followed by the Case 2 which had just adaptive feedforward, and then Case 3 with the non-adaptive feedforward.

	RMS error [deg.]			
Case	Stance Hip	Swing Hip	Swing Knee	Swing Ankle
1	0.30	1.78	11.53	3.86
2	0.90	3.43	7.22	2.39
3	0.09	0.22	0.15	0.14
4	0.07	0.09	0.14	0.08

feedforward control may have given an approximate desired control input, and the feedback control fine tuned the input to further minimize the error. In Fig. 3.12, it can be seen that the amount of feedback motor torque and feedforward motor torque are comparable in magnitude. This indicates that the feedback is not doing all the work in this case. The need for the feedback torque is necessary because after dimensionality reduction, the feedforward component may not be enough to reproduce the movement due to reconstruction loss.

However, in Case 4's results (Fig. 3.13), where optimal inputs instead of reconstructed inputs were used, it can be seen that feedback control still played the same role as it did in Case 3. This is because the optimizations that computed the feedforward components did not consider system disturbances and other unmodeled effects. It can then be concluded that even if more synergies were used (greater than two) the feedforward component would still not be enough. But the benefit of decomposing the optimal inputs and truncating the amount of synergies used reduced amount of data needed in the real-time implementation of the controller. That is to say, instead of having the 10 signals with 750 data points each (.75 seconds at 1kHz) from the optimal inputs, the feedforward controller uses 2 signals and a matrix $W \in \mathbb{R}^{2 \times 10}$ in this case. Therefore, the feedforward component was reduced from using 7500 data points to using only 1520 data points.

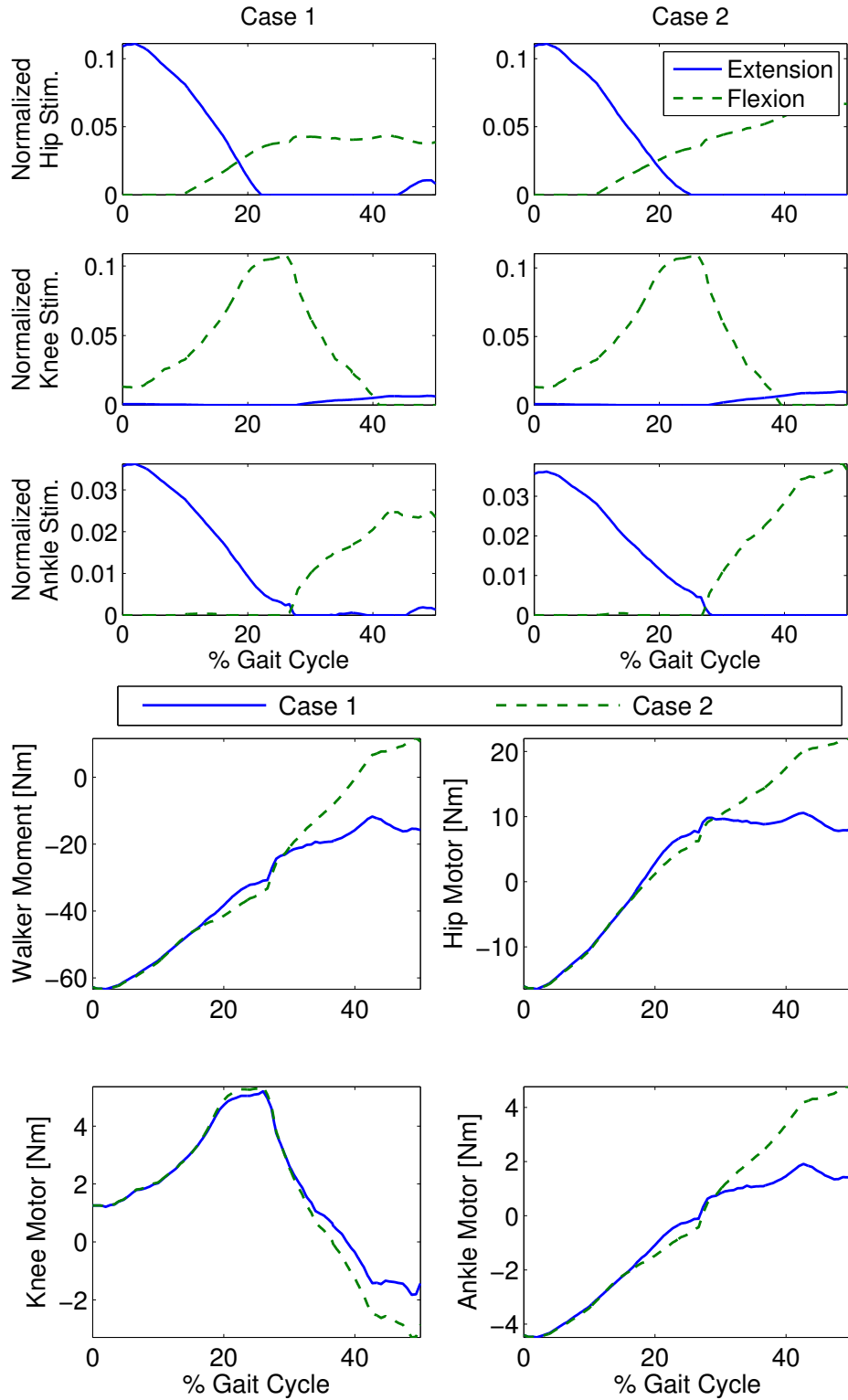


Figure 3.11: Control inputs for Case 1 & 2 of the simulations. Notice that the control input profile shapes, after PCA decomposition, in Case 1 may not be similar to the optimal inputs in Fig. 3.7.

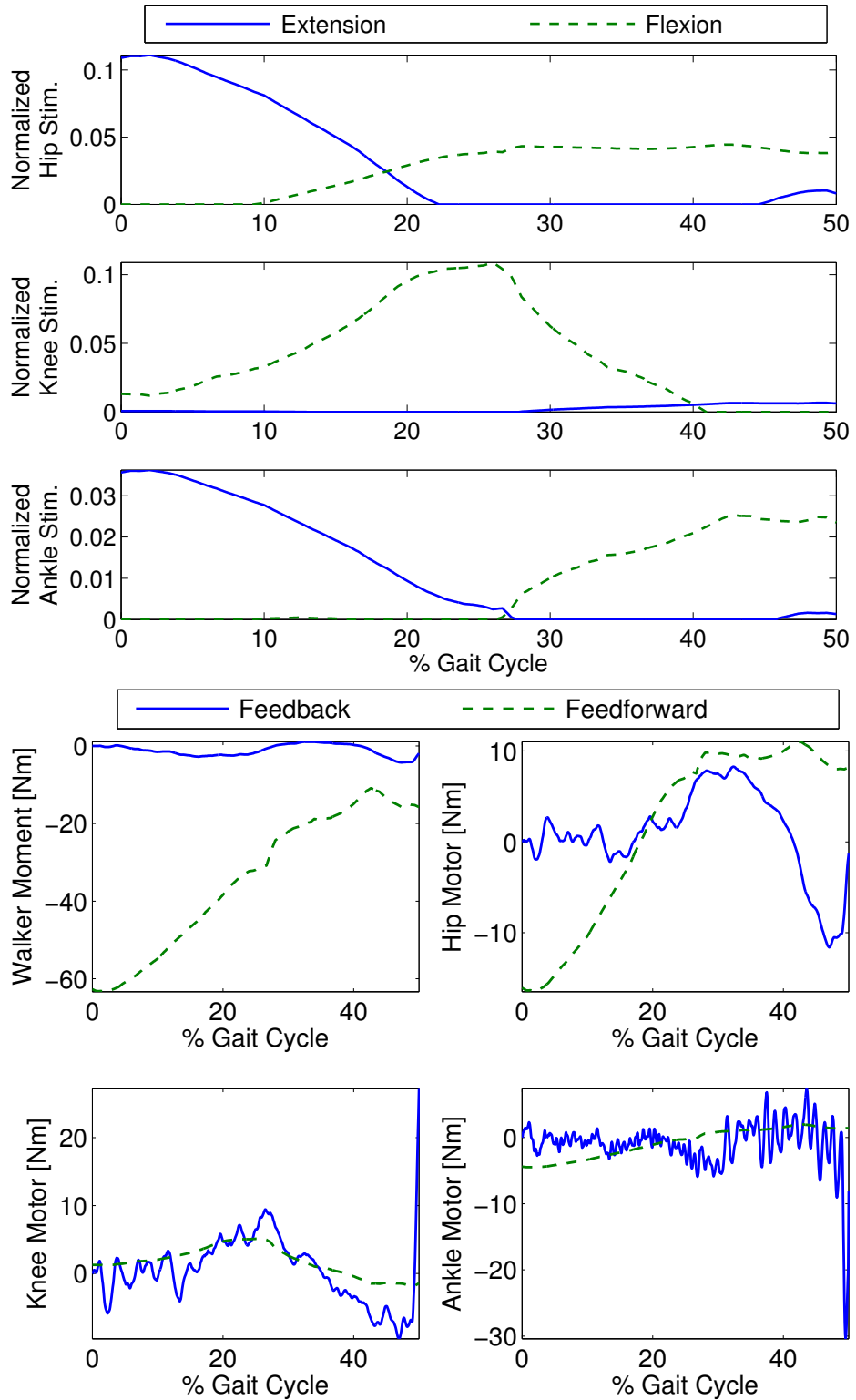


Figure 3.12: Control inputs for Case 3 of the simulations. The feedback's contribution was used only in the walker moment and motor torques.

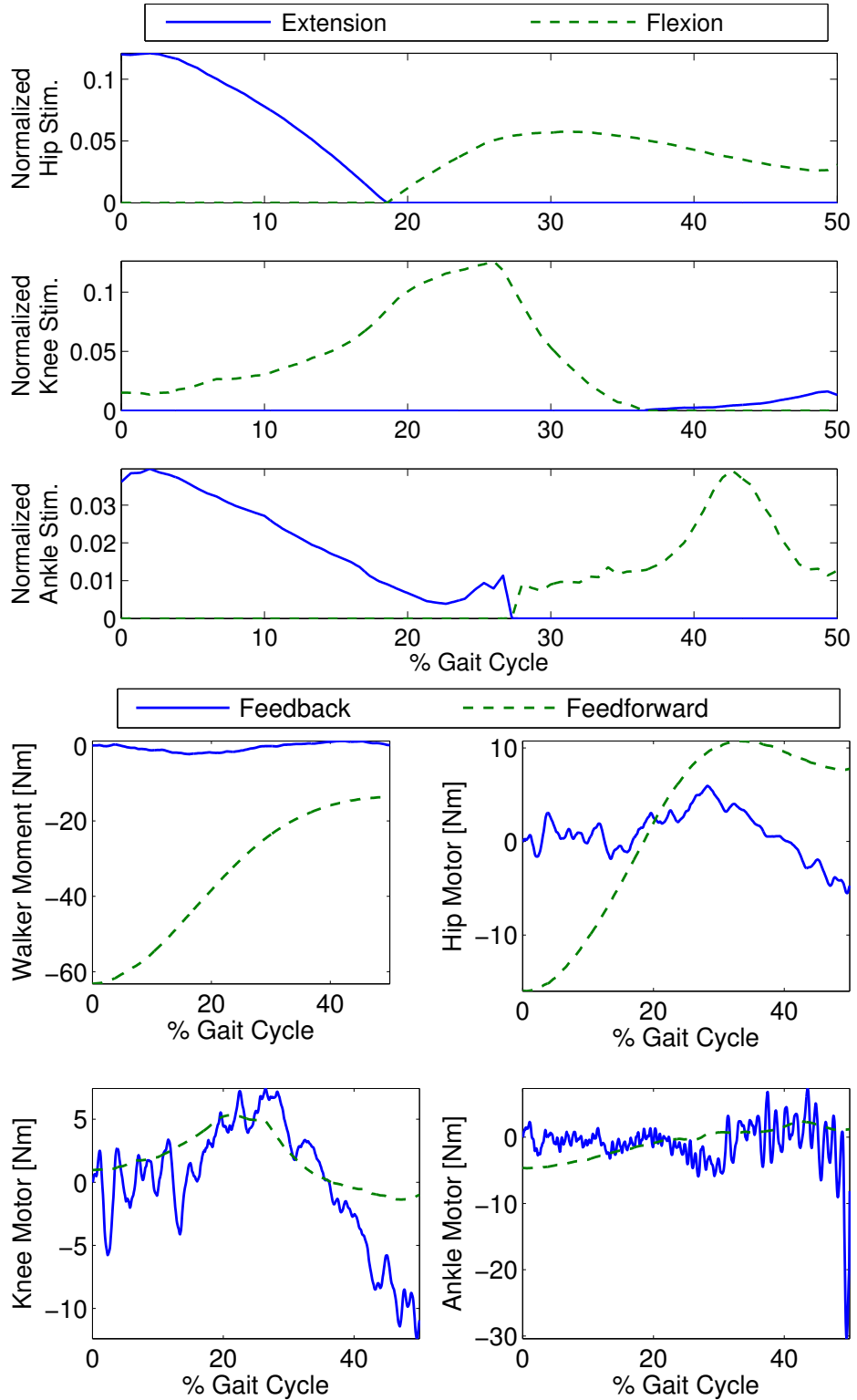


Figure 3.13: Control inputs for Case 4 of the simulations. The feedback's contribution was used only in the walker moment and motor torques.

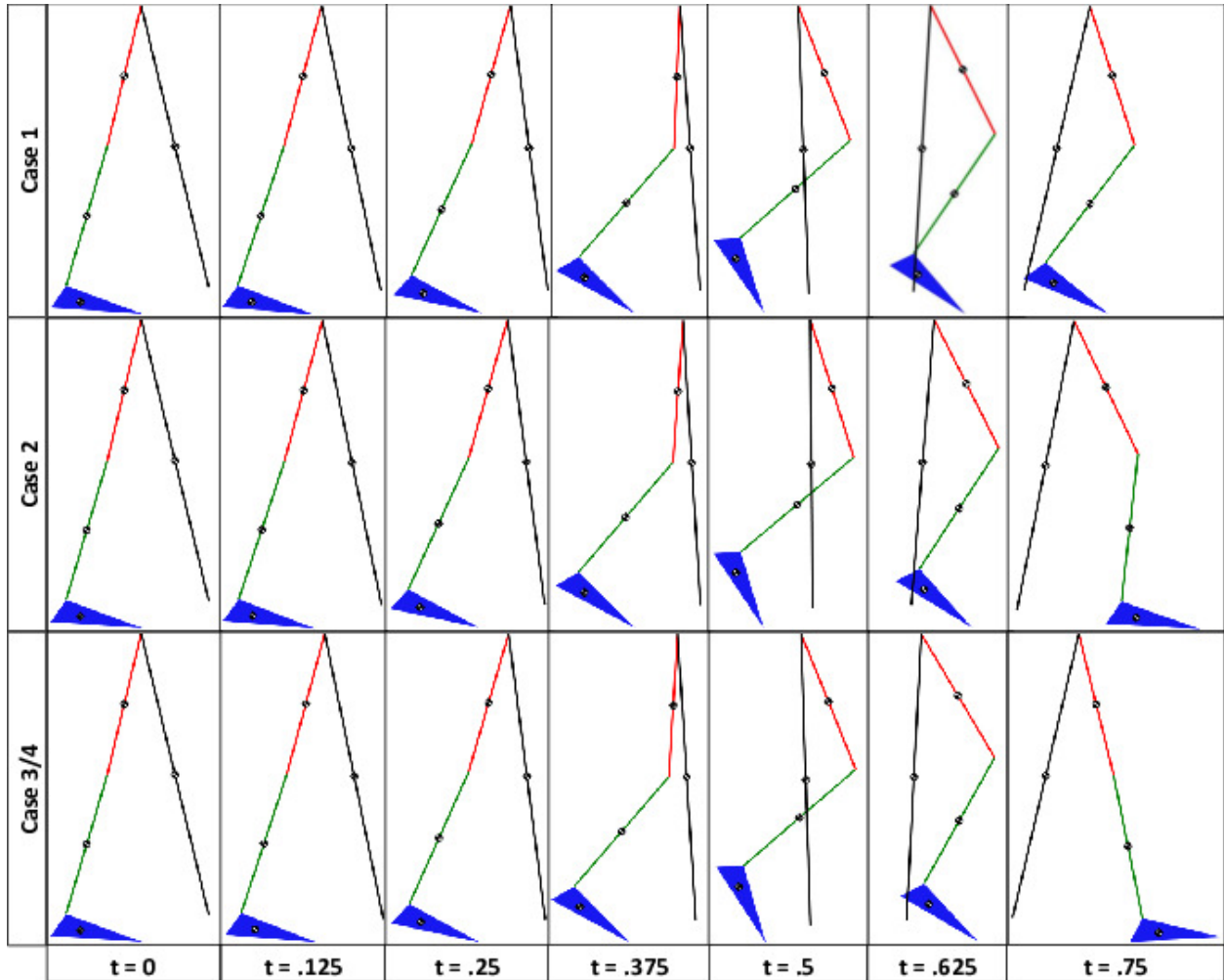


Figure 3.14: The gait sequence for the four cases, a step length of 0.4 meters with a step duration of 0.75 seconds was used. Since the errors for the third and fourth cases are so close their gait sequences look identical.

The limitation of PCA is that the decomposed synergies may not be easily interpreted. For example, in each synergy there is a scaling factor for each of the m control inputs and some synergies may have negative scaling factors. A negative scaling factor may not have any physical meaning (e.g., the stimulation inputs are always positive). Also, adaptation in one activation coefficient changes the scaling factors of all the control inputs in the corresponding synergy, which may result in a non-gait like motion. Interpretation of the synergies becomes even more inscrutable when PCA results in activation coefficients that can be negative.

The new control development is based on time-invariant synergies, which means that all the inputs within a synergy set were activated synchronously and temporal delays were not considered. Perhaps, the use of time-varying synergies, which have a spatial and temporal component, would result in less synergies and a more effective feedforward component. Also, synergies specific to the optimized gait data were extracted which means that they may not span the full input space of the system. However, the developed controller is general enough to be implemented on larger systems with more degrees of freedom and may be used with any set of synergies. While the focus of this chapter was on designing automatic control methods that can handle actuator redundancy, gait optimizations in our result can be improved by using high fidelity gait models or optimization methods such as in [1]. Our future work will explore extracting different forms of muscle synergies and implementing these controllers on human subjects.

3.5 CONCLUSION

In this chapter an adaptive synergy based controller is presented for a walking hybrid neuroprosthesis. The controller used optimal inputs and trajectories, computed from dynamic optimizations, that were performed on a subject specific gait model. A PCA algorithm was used to extract synergies from the optimal inputs to be used as a feedforward component to the controller. An update law was derived, using Lyapunov stability analysis, to adapt the time-varying activation coefficient of the synergies online. In addition, a feedback PD controller was used to make the controller more robust to disturbances. The efficacy of the

controller was demonstrated in simulations first on a 2-DOF fixed hip model and then on a 4-link gait model with 10 actuators including a walker moment, electric motors, and FES of the muscle flexors and extensors.

4.0 DELAY COMPENSATION CONTROL FOR FES-BASED MUSCULOSKELETAL SYSTEMS WITH INPUT DELAY

4.1 INTRODUCTION

In the last chapter a synergy-based controller was developed and tested through simulations to address the actuator redundancy challenge of real-time control of a hybrid neuroprosthesis. The derivation of this controller did not EMD associated with FES. EMD is a time-lag in when the stimulation is applied to when the muscles begin to produce a noticeable force. When unaccounted for, this EMD, which is modeled as an input delay, could cause performance degradation or even system instability.

The focus of this chapter is the derivation and experimental testing of a PID-based delay compensation controller that addresses electromechanical delays in FES-based system. The EMD is assumed to be a known constant and the activation dynamics are neglected. This controller is based off of the previous work of Sharma et al. [89–91] which developed but did not experimentally test the PID-based controller with delay compensation. The key contribution of this work is the modifications made to the error structure to improve the control development and stability analysis and the experimental validation on human subjects. Sections 4.2 and 4.3 will present the control development and Lyapunov stability analysis. The experimental protocol and results are presented in sections 4.4 and 4.5 of this chapter. The controller was experimentally compared to its predecessor the PD-DC controller, which lacked integral control, and the RISE controller, which lacked a delay compensation term.

4.2 CONTROL DEVELOPMENT

4.2.1 Control Objective

The control objective is to track a continuously differentiable desired trajectory, $q_d \in \mathbb{R}$. The tracking error is defined as

$$e_1 = \int_0^t e(s) ds. \quad (4.1)$$

where $e \in \mathbb{R}$ is the tracking error and is defined as $e = q_d - q$. To facilitate the control design and stability analysis, the auxiliary error signals $e_2 \in \mathbb{R}$ and $r \in \mathbb{R}$ are defined as

$$e_2 = \dot{e}_1 + \alpha_1 e_1, \quad (4.2)$$

$$r = \dot{e}_2 + \alpha_2 e_2 - \beta \int_{t-\tau}^t r(\theta) d\theta, \quad (4.3)$$

where $\alpha_1, \alpha_2, \beta \in \mathbb{R}$ are known positive control gains.

The following assumptions and notations are used to facilitate the subsequent control development and stability analysis.

Assumption 1: The moment arm $\zeta(q)$ is assumed to be a non-zero, positive, bounded function [12, 60] whose first time derivative exists and is continuous. The function $\eta(q, \dot{q})$ is assumed to be a non-zero, positive, and bounded function with a bounded and continuous first time derivative based on the empirical data [70, 118].

Assumption 2: The auxiliary non-zero unknown scalar function $\Omega(q, \dot{q}) \in \mathbb{R}^+$, which acts as a nonlinear input gain function to the applied voltage on the muscle, is defined as

$$\Omega = \zeta\eta, \quad (4.4)$$

where the first time derivative of $\Omega(q, \dot{q})$ is assumed to exist, be bounded, and continuous (see Assumption 1).

Assumption 3: The unknown disturbance $d(t)$ is bounded. Its first time derivative exists and is bounded and continuous. Based on Assumptions 1 and 2, the ratio $d(t)/\Omega(q, \dot{q})$,

denoted as $d_\Omega(q, \dot{q}, t)$ is also assumed to be bounded and its first time derivative exists is bounded and continuous.

Assumption 4: Based on Assumption 1, the ratio $J/\Omega(q, \dot{q})$, denoted as $J_\Omega(q, \dot{q}) \in \mathbb{R}^+$, can be upper bounded as

$$J_1 \leq J_\Omega \leq J_2, \quad (4.5)$$

where $J_1, J_2 \in \mathbb{R}^+$ are known constants. The force-length and force-velocity values will never allow the lower bound of J_Ω to be zero (i.e.; $J_1 \neq 0$) within the operating region of the knee joint.

Assumption 5: The EMD, denoted by τ , is assumed to be a known constant. Factors such as fatigue may cause it to be a time-varying phenomenon; however, the influence of these factors on EMDs are ignored.

Assumption 6: The desired trajectory, $q_d \in \mathbb{R}$, and its time derivatives, $\dot{q}_d, \ddot{q}_d, \ddot{\ddot{q}}_d \in \mathbb{R}$, are bounded and continuous.

Notation: A delayed state in the subsequent control development and analysis is denoted as $x(t - \tau)$ or as x_τ while a non-delayed state is denoted as $x(t)$ or as x .

Remark. *Assumptions 1-5 are made mainly for stability analysis and control design. These assumptions are based on empirical results as cited above. These assumptions, except Assumption 5, are standard assumptions and have no or little practical significance as shown in the experimental results presented in [90, 94, 96]. In addition, not all of the controller developed in this research require all of these assumptions.*

4.2.2 Closed-Loop Error System

The open-loop tracking error system can be developed by multiplying the time derivative of (4.3) by J_Ω and utilizing the expressions in (2.5), (2.6), (4.4), (4.1), and (4.2) to obtain

$$J_\Omega \dot{r} = J_\Omega \ddot{q}_d + M_{e\Omega} + M_{v\Omega} + M_{g\Omega} + d_\Omega - u_\tau + J_\Omega \alpha_1 \ddot{e}_1 + J_\Omega \alpha_2 \dot{e}_2 - J_\Omega \beta [r - r_\tau], \quad (4.6)$$

where the nonlinear functions $M_{e\Omega}(q, \dot{q})$, $M_{g\Omega}(q, \dot{q})$, and $M_{v\Omega}(q, \dot{q})$ are defined as

$$M_{e\Omega} = \frac{M_e}{\Omega}, \quad M_{g\Omega} = \frac{M_g}{\Omega}, \quad M_{v\Omega} = \frac{M_v}{\Omega}.$$

Based on (4.6) and to facilitate the subsequent analysis, the voltage input $u \in \mathbb{R}$ is designed as

$$u = Kr, \quad (4.7)$$

where $K \in \mathbb{R}^+$ is a known control gain that can be expanded as

$$K = K_1 + K_2 + K_3, \quad (4.8)$$

where $K_1, K_2,$ and $K_3 \in \mathbb{R}^+$ are known constants. After using (4.7), the closed-loop error system can be written as

$$J_\Omega \dot{r} = -\frac{1}{2} \dot{J}_\Omega r - e_2 + S + \tilde{N} + (\beta J_\Omega - K) r_\tau - \beta J_\Omega r. \quad (4.9)$$

In (4.9), the auxiliary function $\tilde{N}(e_1, e_2, r, e_I, t)$ and $S(\Omega, \dot{\Omega}, t) \in \mathbb{R}$ are defined as

$$N = \frac{1}{2} \dot{J}_\Omega r + J_\Omega \ddot{q}_d + e_2 + M_{e\Omega} + M_{v\Omega} + M_{g\Omega} - J_\Omega \alpha_1^2 e_1 + J_\Omega (\alpha_1 + \alpha_2) (r - \alpha_2 e_2 + \beta e_I), \quad (4.10)$$

$$N_d = J_{\Omega d} \ddot{q}_d + M_{e\Omega d} + M_{v\Omega d} + M_{g\Omega d}, \quad (4.11)$$

$$\tilde{N} = N - N_d, \quad S = N_d + d_\Omega, \quad (4.12)$$

where $J_{\Omega d}(q_d, \dot{q}_d)$, $M_{v\Omega d}(q_d, \dot{q}_d)$, and $M_{e\Omega d}(q_d, \dot{q}_d)$ are inertial, viscous, and stiffness terms (defined in (2.5)) that are expressed in terms of desired limb position (q_d) and velocity (\dot{q}_d), and $e_I(r, t, \tau) \in \mathbb{R}$ is defined as

$$e_I = \int_{t-\tau}^t r(\theta) d\theta. \quad (4.13)$$

Using the mean value theorem, the auxiliary functions $\tilde{N}(e_1, e_2, r, e_I, t, \tau)$ and $S(\Omega, \dot{\Omega}, t)$ can be upper bounded as

$$|\tilde{N}| \leq \rho(\|z\|) \|z\|, \quad |S| \leq \xi. \quad (4.14)$$

In (4.5), $\xi \in \mathbb{R}^+$ is a known constant, the bounding function $\rho(\|z\|) \in \mathbb{R}$ is a positive globally invertible non-decreasing function, and $z(e_1, e_2, r, e_I) \in \mathbb{R}^4$ is defined as

$$z = \begin{bmatrix} e_1 & e_2 & r & e_I \end{bmatrix}^T. \quad (4.15)$$

Based on the subsequent stability analysis, LK functionals: $P(r, t, \tau) \in \mathbb{R}$ and $Q(r, t, \tau) \in \mathbb{R}$ are defined as

$$P = \omega \int_{t-\tau}^t \left(\int_s^t r(\theta)^2 d\theta \right) ds, \quad (4.16)$$

$$Q = \psi \int_{t-\tau}^t r(\theta)^2 d\theta, \quad (4.17)$$

where $\omega, \psi \in \mathbb{R}^+$ are known constants.

4.3 STABILITY ANALYSIS

Theorem 2. *The controller given in (4.7) ensures semi-globally uniformly ultimately bounded tracking:*

$$|e_1(t)| \leq \epsilon_0 \exp(-\epsilon_1 t) + \epsilon_2, \quad (4.18)$$

where $\epsilon_0, \epsilon_1, \epsilon_2 \in \mathbb{R}^+$ denote constants, provided the control gains $\alpha_1, \alpha_2, \beta, K,$ and K_3 introduced in (4.2), (4.3), (4.7) and (4.8), respectively, are selected according to the following sufficient conditions:

$$\begin{aligned} \beta J_1 > K, \quad K_3 > \omega\tau + \psi, \quad \psi > \beta J_2 - K, \\ \alpha_1 > \frac{1}{2}, \quad \omega > \frac{2}{\gamma} + \frac{\tau\beta^2}{2}, \quad \alpha_2 > 1. \end{aligned} \quad (4.19)$$

In (4.19), the known positive constants J_1, J_2, ω and ψ are defined in (4.5), (4.16) and (4.17), respectively, τ is the input delay and $\gamma \in \mathbb{R}^+$ is a subsequently defined constant.

Proof: Let $y(t) \in \mathcal{D} \subset \mathbb{R}^5$ be defined as

$$y \triangleq \begin{bmatrix} e_1 & e_2 & r & \sqrt{P} & \sqrt{Q} \end{bmatrix}^T. \quad (4.20)$$

A positive definite Lyapunov functional candidate $U(y, t) : \mathcal{D} \times [0, \infty) \rightarrow \mathbb{R}$ is defined as

$$U \triangleq \frac{1}{2}e_1^2 + \frac{1}{2}e_2^2 + \frac{1}{2}J_\Omega r^2 + P + Q, \quad (4.21)$$

and satisfies the following inequalities

$$\lambda_1 \|y\|^2 \leq U \leq \lambda_2 \|y\|^2, \quad (4.22)$$

where $\lambda_1, \lambda_2 \in \mathbb{R}^+$ are known constants defined as

$$\lambda_1 = \frac{1}{2} \min [J_1, 1], \quad \lambda_2 = \max \left[\frac{J_2}{2}, 1 \right],$$

where J_1 and J_2 are defined in (4.5).

After using (4.2), (4.3), and (4.9), and canceling the common terms, the time derivative of (4.21) can be expressed as

$$\begin{aligned} \dot{U} = & e_1 e_2 - \alpha_1 e_1^2 - \alpha_2 e_2^2 + \beta e_2 \int_{t-\tau}^t r(\theta) d\theta + rS + r\tilde{N} + (\beta J_\Omega - K) r r_\tau \\ & - \beta J_\Omega r^2 + \omega \tau r^2 - \omega \int_{t-\tau}^t r(\theta)^2 d\theta + \psi(r^2 - r_\tau^2). \end{aligned} \quad (4.23)$$

On applying the Young's Inequality and utilizing the definition of e_I in (4.13), the following terms in (4.23) can be bounded as

$$e_1 e_2 \leq \frac{1}{2} e_1^2 + \frac{1}{2} e_2^2, \quad (4.24)$$

$$e_2 \beta \int_{t-\tau}^t r(\theta) d\theta \leq \frac{\beta^2}{2} e_I^2 + \frac{1}{2} e_2^2. \quad (4.25)$$

Further, by using the Cauchy Schwarz inequality, the following term in (4.25) can be upper bounded as

$$e_I^2 \leq \tau \int_{t-\tau}^t r(\theta)^2 d\theta. \quad (4.26)$$

Utilizing (4.5), (4.14), (4.24), and (4.26), (4.23) can be bounded as

$$\begin{aligned} \dot{U} \leq & - \left(\alpha_1 - \frac{1}{2} \right) e_1^2 - (\alpha_2 - 1) e_2^2 + |r| \xi + |r| \rho(\|z\|) \|z\| + (\beta J_\Omega - K) r r_\tau \\ & - \beta J_\Omega r^2 + \omega \tau r^2 - \omega \int_{t-\tau}^t r(\theta)^2 d\theta + \frac{\tau \beta^2}{2} \int_{t-\tau}^t r(\theta)^2 d\theta + \psi(r^2 - r_\tau^2). \end{aligned} \quad (4.27)$$

Note that by choosing control gains β and K such that $\beta J_1 > K$, the following Young's inequality can be used

$$(\beta J_\Omega - K) r r_\tau \leq (\beta J_\Omega - K) (r^2 + r_\tau^2). \quad (4.28)$$

After adding and subtracting $\frac{2}{\gamma} \int_{t-\tau}^t r(\theta)^2 d\theta$ to (4.27) and utilizing (4.26), provided that $\omega - \frac{2}{\gamma} - \frac{\tau\beta^2}{2} > 0$, (4.27) can be upper bounded as

$$\begin{aligned} \dot{U} \leq & - \left(\alpha_1 - \frac{1}{2} \right) e_1^2 - (\alpha_2 - 1) e_2^2 - \frac{1}{\tau} \left(\omega - \frac{2}{\gamma} - \frac{\tau\beta^2}{2} \right) e_I^2 + |r| \xi + |r| \rho(\|z\|) \|z\| \\ & + \omega\tau r^2 - \frac{2}{\gamma} \int_{t-\tau}^t r(\theta)^2 d\theta - \beta J_\Omega r^2 + (\beta J_\Omega - K) (r^2 + r_\tau^2) + \psi (r^2 - r_\tau^2). \end{aligned}$$

Rearranging the terms and canceling the common terms results in

$$\begin{aligned} \dot{U} \leq & - \left(\alpha_1 - \frac{1}{2} \right) e_1^2 - (\alpha_2 - 1) e_2^2 - \frac{1}{\tau} \left(\omega - \frac{2}{\gamma} - \frac{\tau\beta^2}{2} \right) e_I^2 + |r| \xi + |r| \rho(\|z\|) \|z\| \quad (4.29) \\ & - \frac{2}{\gamma} \int_{t-\tau}^t r(\theta)^2 d\theta - (\psi - (\beta J_\Omega - K)) r_\tau^2 - K_1 r^2 - K_2 r^2 - (K_3 - \omega\tau - \psi) r^2. \end{aligned}$$

After utilizing (4.8), completing the squares, and provided that $\psi > (\beta J_\Omega - K)$, (4.29) can be upper bounded as

$$\begin{aligned} \dot{U} \leq & - \left(\alpha_1 - \frac{1}{2} \right) e_1^2 - (\alpha_2 - 1) e_2^2 - (K_3 - \omega\tau - \psi) r^2 - \frac{1}{\tau} \left(\omega - \frac{2}{\gamma} - \frac{\tau\beta^2}{2} \right) e_I^2 \quad (4.30) \\ & + \frac{\rho^2(\|z\|) \|z\|^2}{4K_2} + \frac{\xi^2}{4K_1} - \frac{2}{\gamma} \int_{t-\tau}^t r(\theta)^2 d\theta. \end{aligned}$$

Since

$$\begin{aligned} \int_{t-\tau}^t \left(\int_s^t r(\theta)^2 d\theta \right) ds & \leq \tau \sup_{s \in [t, t-\tau]} \left[\int_s^t r(\theta)^2 d\theta \right] \\ & = \tau \int_{t-\tau}^t r(\theta)^2 d\theta, \end{aligned}$$

and after utilizing (4.15), (4.16), and (4.17), the inequality in (4.30) can be expressed as

$$\dot{U} \leq - \left(\mu - \frac{\rho^2(\|z\|)}{4K_2} \right) \|z\|^2 - \frac{1}{\gamma\tau\omega} P - \frac{1}{\gamma\psi} Q + \frac{\xi^2}{4K_1}, \quad (4.31)$$

where μ is defined as

$$\mu = \min \left[\alpha_1 - \frac{1}{2}, K_3 - \omega\tau - \psi, \alpha_2 - 1, \frac{1}{\tau} \left(\omega - \frac{2}{\gamma} - \frac{\tau\beta^2}{2} \right) \right]$$

Using the definition of $y(t)$ in (4.20), the expression in (4.31) can be upper bounded as

$$\dot{U} \leq -\bar{\mu} \|y\|^2 - \left\{ \mu - \frac{\rho^2(\|z\|)}{4K_2} \right\} \|e_I\|^2 + \frac{\xi^2}{4K_1}, \quad (4.32)$$

where $\bar{\mu}(\|z\|) \in \mathbb{R}^+$ is defined as

$$\bar{\mu} = \min \left[\mu - \frac{\rho^2(\|z\|)}{4K_2}, \frac{1}{\gamma\tau\omega}, \frac{1}{\gamma\psi} \right].$$

In order to further bound (4.32), it is required that $\mu - \frac{\rho^2(\|z\|)}{4K_2} > 0$ which is true if $\|z\|^2 < \rho^{-2}(2\sqrt{\mu K_2})$. Consider a set \mathcal{S} defined as

$$\mathcal{S} \triangleq \left\{ y(t) \in \mathbb{R}^5 \mid \|y(0)\| < \sqrt{\frac{\lambda_1}{\lambda_2} \min \left\{ 1, \frac{\bar{\psi}}{\tau} \right\} \rho^{-2}(2\sqrt{\mu K_2}) - \frac{\xi^2}{4K_1\delta}} \right\}$$

In \mathcal{S} , $\bar{\mu}(\|z\|)$ can be lower bounded by a constant $\delta \in \mathbb{R}^+$ as

$$\delta \leq \bar{\mu}(\|z\|),$$

and the condition, $\|z\|^2 < \rho^{-2}(2\sqrt{\mu K_2})$, is satisfied. By further utilizing (4.22), the inequality in (4.32) can be expressed as

$$\dot{U} \leq -\frac{\bar{\mu}}{\lambda_2} U + \frac{\xi^2}{4K_1}. \quad (4.33)$$

The linear differential equation in (4.33) can be solved as

$$U \leq U(0)e^{-\frac{\delta}{\lambda_2}t} + \frac{\xi^2\lambda_2}{4K_1\delta} \left[1 - e^{-\frac{\delta}{\lambda_2}t} \right], \quad (4.34)$$

provided the control gains α_1 , α_2 , β , and K are selected according to the sufficient conditions in (4.19) (i.e. a semi-global result). The result in (4.18) can now be obtained from (4.34). Based on the definition of $y(t)$, the result in (4.34) indicates that $e_1(t)$, $e_2(t)$, $r(t) \in \mathcal{L}_\infty$ in \mathcal{S} . Since $r(t) \in \mathcal{L}_\infty$ in \mathcal{S} , then (4.13) indicates that $e_I(t) \in \mathcal{L}_\infty$ in \mathcal{S} . Given that $e_1(t)$, $e_2(t)$, $q_d(t)$, $\dot{q}_d(t) \in \mathcal{L}_\infty$ in \mathcal{S} , (4.1) and (4.2) indicate that $q(t)$ and $\dot{q}(t) \in \mathcal{L}_\infty$ in \mathcal{S} . Since $r(t)$, $e_2(t)$, $e_I(t)$, $\dot{q}(t)$, $\dot{q}_d(t)$, $\ddot{q}_d(t) \in \mathcal{L}_\infty$ in \mathcal{S} , then (4.3) indicates that $\ddot{q}(t) \in \mathcal{L}_\infty$ in \mathcal{S} . Given that $r(t)$, $e_2(t)$, $e_I(t)$, $\dot{q}(t)$, $\dot{q}_d(t)$, $\ddot{q}_d(t) \in \mathcal{L}_\infty$ in \mathcal{S} , (4.6) and Assumptions 3 and 4 indicate that $V(t) \in \mathcal{L}_\infty$ in \mathcal{S} . ■

4.4 EXPERIMENTAL PROTOCOL

The new controller was applied as an amplitude modulated voltage to external electrodes attached to the quadriceps femoris muscle group in 4 non-impaired volunteers. The new controller was compared with its predecessors: PD-DC [90] and the Robust Integral of the Sign of the Error (RISE) [94]. The experimental results indicated that the new controller reduced the steady state root mean squared tracking error (SSRMSE) compared to the two previously developed nonlinear controllers, and was found to be robust to variations in the estimated EMD value.

The experiments were conducted on two testbeds as shown in Fig. 2.6: a modified LEM (A) and a brace (B) to mimic lower leg swing during walking. Four able bodied male subjects between the ages of 24-30 years were selected for the experiments. Prior to any experimentation, an approval from the Institutional Review Board at the University of Pittsburgh was obtained. The participants were instructed to relax and avoid any voluntary interference during the electrical stimulation. Two sets of experiments were conducted to evaluate the performance of the new controller and its robustness to variations in the estimated EMD value. Each experimental session was run for a duration of 30 seconds with a rest period of 3 minutes in between the sessions to prevent muscle fatigue.

In the first set of experiments, we compared the new controller (PID-DC) with two previously developed nonlinear controllers (PD-DC and RISE). The details of the RISE control law and PD-DC control law can be found in [94] and [90], respectively. These controllers were chosen because, just like the controller developed in this paper, they fall under the category of strictly feedback tracking controllers that are designed based on a nonlinear musculoskeletal system and are synthesized using a Lyapunov stability analysis. In addition, these controllers are easily implementable and do not require any model knowledge, unlike the sliding mode controller (SMC) in [63]. During the experiments, the 4 subjects were unaware of the controller being tested during the session. For each subject, the order of the controllers was selected at random and were tested on separate days (every other day). The three controllers were used to track a sinusoidal signal with a period of 2-seconds and alternating peaks. The desired trajectory started from the equilibrium and oscillated

between a minimum amplitude of 15° and an alternating maximum amplitudes of 35° and 25° , this prevented any subject from anticipating the desired motion and subconsciously interfering with the performance of the controller. Each controller was evaluated in five consecutive trials for each subject. A rest period of 3 minutes was given in between the 30 second trials. Also, the subjects were not allowed to view the desired trajectory or the performance in real-time. In addition to these experiments, the three controllers were tested on one subject with a larger range of motion ($5 - 50^\circ$) to see if the controllers could maintain their performance for larger movements.

As these experiments were conducted on human subjects, the gain tuning procedure could only be done over a finite interval of time in order to prevent muscle fatigue and subject discomfort. Prior to experimentation on a subject, the three controllers were tuned to find an initial guess of the control gains. Before conducting the five trials for each controller, the controller was further tuned, beginning at the initial guess. The control gains were fine tuned till the error over a 10 second trial was minimized.

Since the PD-DC and PID-DC require the knowledge of the EMD value, it was determined empirically for each test subject. This was done by applying a step stimulation at a time instant and measuring the time when the resulting knee joint movement occurred. The EMD value was calculated as the time difference from when the first stimulation pulse was applied and when the knee angle began to change. Five measurements of the EMD value were taken, and the average of the five values was used as the measured EMD value, which is used in the control implementation.

In the second set of experiments, the PID-DC controller was tested for its robustness to variations in the EMD value. This was done by assuming an estimated EMD value, used in the PID-DC controller, different from the measured EMD value in the previous experiments. A subject (H1) was held in a gait like configuration using a brace as shown in Fig. 2.4 B. The thigh of the subject was fixed at a certain angle (using the motor in the brace), while the new controller was used to track a sinusoidal trajectory with a 2 second time period. Robustness of the controller to an estimate EMD value was tested by evaluating its performance for estimated EMD values that ranged between ± 2 standard deviations (SD) from the mean of the measured EMD value.

4.5 EXPERIMENTAL RESULTS

Figs. 4.1-4.4 and Tables 4.1-4.4 illustrate the results from the two sets of experiments. In the first set of experiments, each controller was tested in five trials on each subject and then again on one subject with a larger range of motion. Trials for the PD-DC and PID-DC used the empirically found EMD values as reported in Table 4.3. A representative trial from each controller is shown in Fig. 4.1 and the control gains used to produce those results are given in Table 4.1. Table 4.3 contains the three criteria used to measure the performance of each controller: the root mean squared of the error (RMSE), steady state RMSE (SSRMSE), and root mean squared of the current (RMSC). The RMSC was normalized by the body mass index of each subject in order to scale the control effort with respect to the size of the subjects. Since the RISE and PID-DC controller have integral control, they require a transient period for the memory component to build up, that is why the SSRMSE is the primary focus of the comparison.

The differences in the aforementioned performance criteria were assessed using a one-way analysis of variance (ANOVA) with repeated measures. Post-hoc testing consisting of paired t-tests with a Bonferroni correction was performed when a significant ANOVA tests were identified. A Bonferroni adjustment was used to avoid potential type I errors associated with performing multiple t-tests in the post-hoc analysis. As a result, the critical threshold for significance was reduced to $P < 0.016$ (0.05 divided by 3). The results for the statistical analyses are given in Fig. 4.3, where each criterion's amplitude has been normalized to the maximum criterion value. This normalization is performed strictly for plotting the results and is completely independent of the ANOVA analyses. The SSRMSE of the PID-DC controller was found to be significantly lower than that of the other controllers ($p - value = 1.8E - 7$ between PD-DC and PID-DC and $p - value = 3.1E - 4$ between PID-DC and RISE). The RISE controller's SSRMSE was found to be lower than that of the PD-DC controller ($p - value = 3.4E - 4$). Although the SSRMSE was used to make the main comparison, the RMSE results were found to be concurrent with the SSRMSE results and can be seen in Table 4.3. Lack of integral control, which gives a controller a memory component in order to compensate for steady state errors, in the PD-DC controller

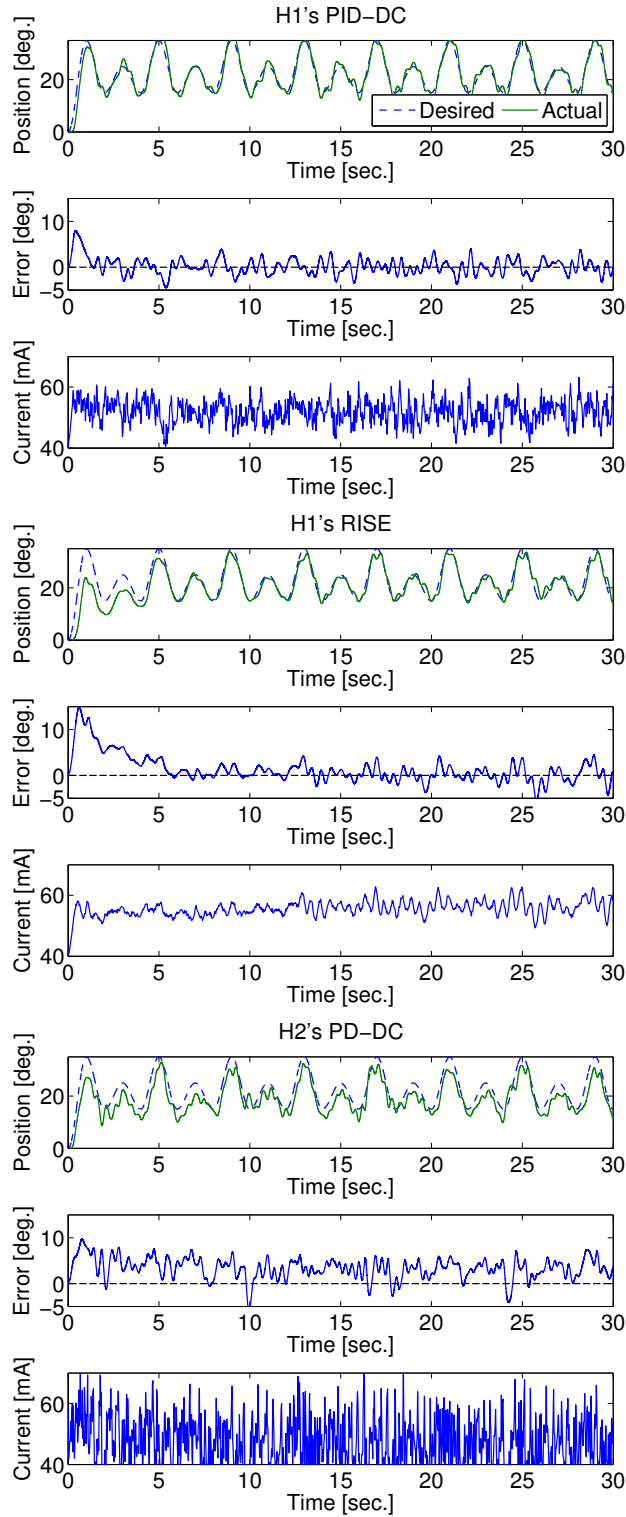


Figure 4.1: Experimental results obtained from the representative trial for each of the three controllers. These plots show the desired & actual angular position (top plots), error (middle plots), and stimulation current amplitude (bottom plots).

Table 4.1: The gains used to produce the experimental results shown in Fig. (4.1).

	k	α_1	α_2	β
H1's PID-DC	800	10.89	1.6	65
H1's RISE	125	7.57	0.42	100
H2's PD-DC	2000	8	-	75

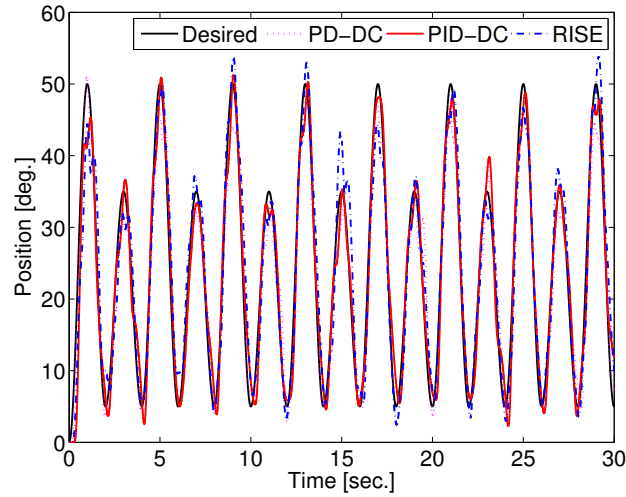


Figure 4.2: Results obtained from running the three controllers on subject H1 with a larger trajectory ranging from $5 - 50^\circ$.

Table 4.2: The tabulated results for the sinusoidal trajectory with 2 second time period ranging from $5 - 50^\circ$ implemented on subject H1 with all three controllers.

	RMSE [deg.]	SSRMSE [deg.]	RMSC [mA m ² kg ⁻¹]
PID-DC	3.15	2.76	1.90
RISE	3.96	3.57	2.05
PD-DC	3.13	3.15	1.79

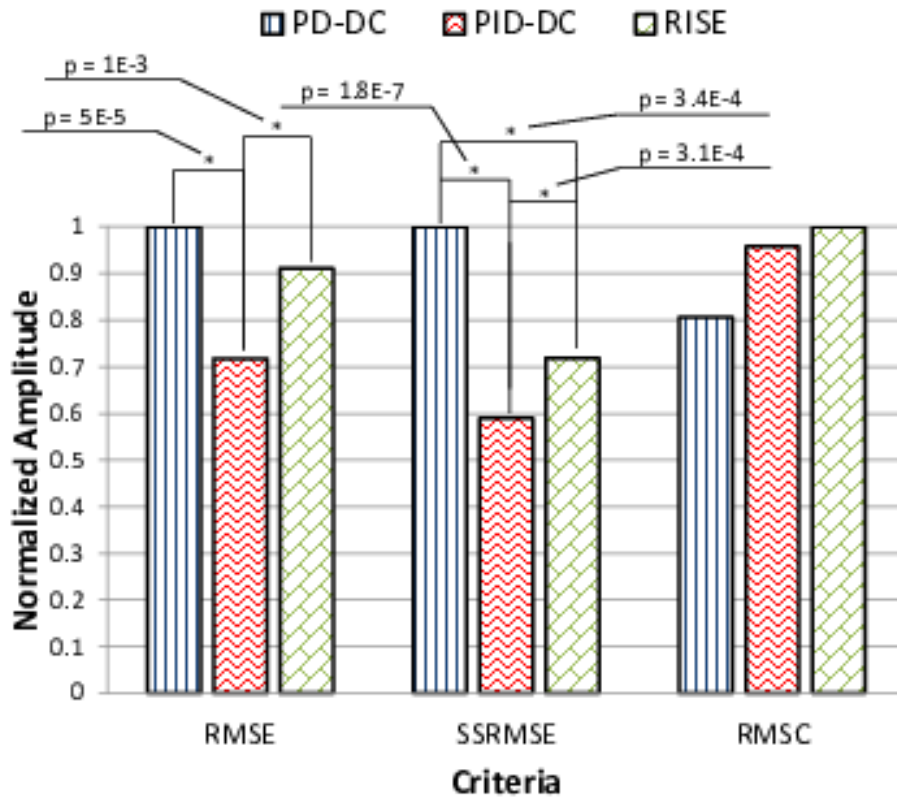


Figure 4.3: A graphical representation of the results from the LEM experiments. The three criteria: RMSE, SSRMSE, and RMSC were normalized by the maximum of each criterion after the ANOVA analyses were done. * indicates statistically significant differences between the controllers at a 95% confidence level and p refers to the p -value.

Table 4.3: The tabulated results for the sinusoidal trajectory with 2 second time period experiments include the average (AVG) and standard deviation (SD) of the EMD values measured for each volunteer subject (S) across five samples, the average root mean squared error (RMSE), the average steady state RMSE (SSRMSE), and the average root mean squared current (RMSC) normalized by the body mass index of each subject.

S	AVG EMD	SD
H1	<i>84.8</i>	<i>20.33</i>
H2	<i>91.8</i>	<i>14.97</i>
H3	<i>108.2</i>	<i>18.91</i>
H4	<i>103.6</i>	<i>8.26</i>
AvG	<i>97.1</i>	<i>10.72</i>

S	AVG RMSE [<i>deg.</i>]			AVG SSRMSE [<i>deg.</i>]			AVG RMSC [<i>mA m² kg⁻¹</i>]		
	PD-DC	PID-DC	RISE	PD-DC	PID-DC	RISE	PD-DC	PID-DC	RISE
H1	<i>4.37</i>	<i>2.04</i>	<i>3.19</i>	<i>4.36</i>	<i>1.70</i>	<i>2.32</i>	<i>2.50</i>	<i>2.11</i>	<i>2.06</i>
H2	<i>3.37</i>	<i>3.32</i>	<i>4.97</i>	<i>3.21</i>	<i>2.59</i>	<i>3.47</i>	<i>1.75</i>	<i>2.46</i>	<i>2.61</i>
H3	<i>4.47</i>	<i>3.21</i>	<i>2.73</i>	<i>4.37</i>	<i>2.62</i>	<i>2.48</i>	<i>1.80</i>	<i>2.44</i>	<i>2.56</i>
H4	<i>3.01</i>	<i>2.34</i>	<i>2.96</i>	<i>2.96</i>	<i>1.89</i>	<i>2.44</i>	<i>1.63</i>	<i>2.12</i>	<i>2.30</i>
AvG	<i>3.80</i>	<i>2.73</i>	<i>3.47</i>	<i>3.73</i>	<i>2.20</i>	<i>2.68</i>	<i>1.92</i>	<i>2.28</i>	<i>2.38</i>

seems to have played a role in its greater RMSE and SSRMSE as compared to the other two controllers.

While tuning the controllers, it was observed that in order to maintain stability with the RISE controller, the gain associated with integral control in the PID component of the controller, (i.e., $k\alpha_1\alpha_2$), was required to be kept low. This could be due to the combination of controller's increased responsiveness due to integral action and EMD-induced oscillations. Unlike the RISE controller, the PID-DC did not have this issue because the DC component provided the controller more robustness by removing the ill-timed excess energy that induced these oscillations. One thing to note is that because of the DC component the gains for the PD-DC and PID-DC were required to be much larger than the gains for the RISE controller. This does not necessarily mean the PD-DC and PID-DC controllers were using more control effort. This is simply due to the mechanics of the DC part of the controllers. The DC part of the controller integrates the control signal over an interval the duration of the input delay and subtracts it from the PID component of the controller. Therefore, most of the control effort generated from the PID component was dissipated due the DC component. Although results of the PD-DC controller reported the lowest RMSC as compared to the other two controllers, the statistical analysis determined that the differences in the RMSCs were not statistically significant (p -value = $7.5E-1$ between PD-DC and PID-DC, p -value = $8.9E-1$ between PD-DC and RISE, p -value = $7.6E-1$ between PID-DC and RISE). From Fig.4.2 and Table 4.2, it can be seen that even with larger ranges of motion, the PID-DC continued to outperform the other two controllers.

In the second set of experiments, the measured EMD value was empirically found to be 85 ms for Subject H1. The experimental results for tracking the sinusoidal trajectory with a 2 second time period, where the PID-DC controller used estimate EMD values different from the measured EMD value, are given in Fig. 4.4 and Table 4.4. As the estimated EMD value strayed from the measured EMD value, before tuning β (BTB), the control performance deteriorated but the controller maintained stability. However, after tuning β (ATB), the PID-DC controller not only maintained stability but also provided the same level of performance as in the first set of experiments. This was observed even when the estimated EMD value was varied by ± 2 SDs from the measured EMD value. Results when

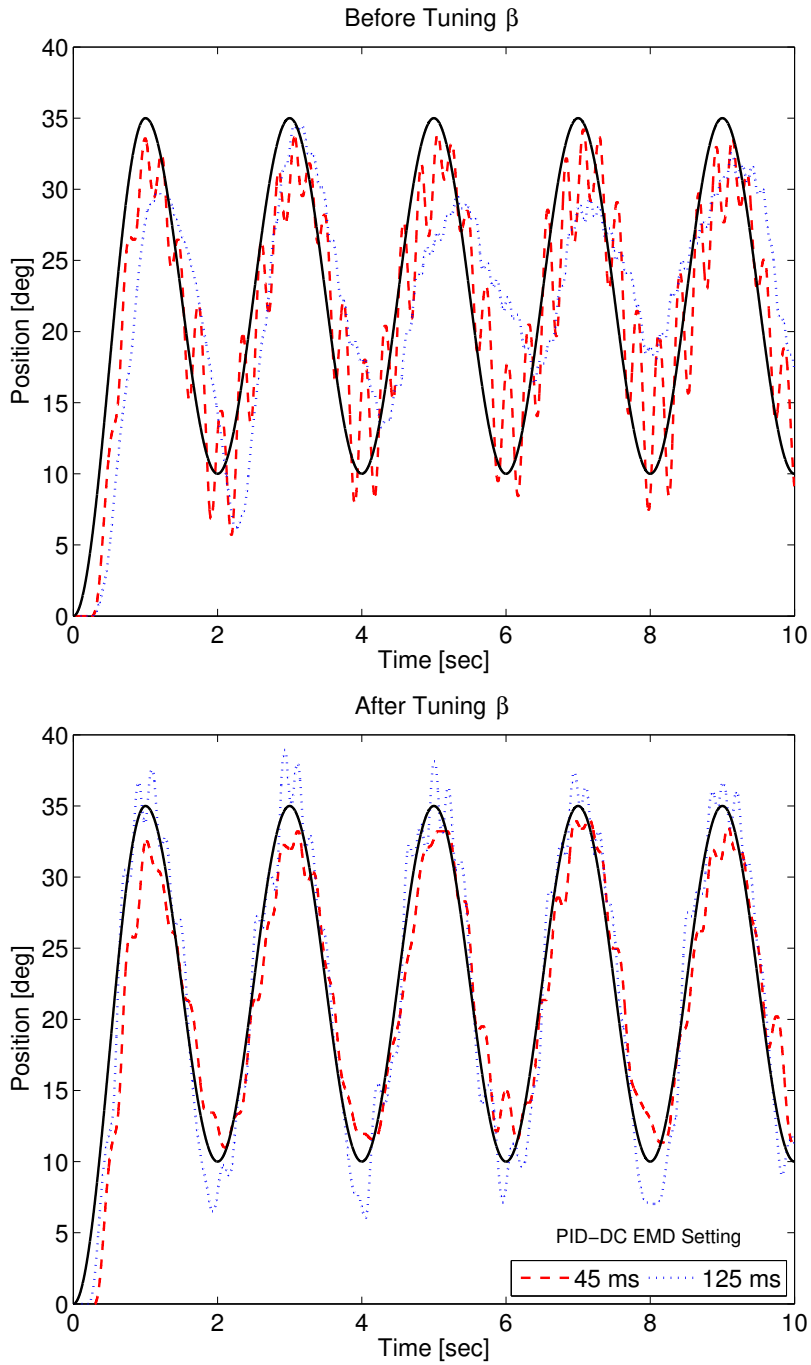


Figure 4.4: Tracking performance of PID-DC with mismatched EMDs that were set to ± 2 SDs away from the mean measured EMD. With mismatched EMD settings, the performance degraded but the PID-DC maintained stability. Top plot: the control performance, before tuning β . Bottom plot: the tracking performance improved after tuning β .

Table 4.4: Tabulated results for the robustness of the estimated EMD value in the PID-DC controller as opposed to the measured EMD value of 85 *ms*. Note that the controller was able to maintain consistent performance even with mismatched EMDs after tuning β (ATB). The results for the estimated EMD values before tuning β (BTB) were included to demonstrate the effect of tuning β .

EMD [ms]	RMSE [deg.]		SSRMSE [deg.]		RMSC [mA m ² kg ⁻¹]	
	ATB	BTB	ATB	BTB	ATB	BTB
45	2.74	4.45	2.51	4.36	1.87	2.18
65	2.37	2.65	2.06	2.40	1.91	1.93
85	2.24	2.24	1.91	1.91	1.80	1.80
105	2.70	4.60	2.56	4.36	1.73	1.94
125	2.36	6.83	2.32	6.93	1.75	1.97

the estimated EMD values were assumed to be ± 2 SDs away from the measured EMD value are plotted in Fig. 4.4. The decrease in control performance, resulting from mismatched delay estimates, was compensated for by tuning the gain β . For example, for the estimate EMD values greater than the measured EMD value, the DC portion of the controller over compensated due to the larger integral interval; therefore, decreasing β helped in offsetting the effect of mismatched EMD values. Similarly, increasing β helped in offsetting the effect of mismatched EMD values, when an estimated EMD value was smaller than the measured EMD value.

4.6 CONCLUSION

In this chapter, a PID-based delay compensation (PID-DC) controller was developed for an NMES-driven musculoskeletal system with EMDs. Lyapunov-based stability analysis yielded

semi-globally uniformly ultimately bounded tracking despite model uncertainties and EMDs. The addition of the integral action resulted in improved performance that was validated on four able bodied subjects and empirically compared to two nonlinear controllers: PD-DC (previous control design for EMD compensation) and RISE controller. The results showed that the PID-DC has a superior tracking performance (statistically significant) vis--vis the other two controllers. Further, the new controller was shown to be robust to variations in the measured EMDs. Future work will focus on testing this controller on persons with stroke or SCI, investigating the benefits of adding activation dynamics, considering spasticity and fatigue [49], and extending the controller to multiple degrees of freedom and more general systems.

5.0 DYNAMIC SURFACE CONTROL OF FUNCTIONAL ELECTRICAL STIMULATION SYSTEMS WITH ACTIVATION DYNAMICS

5.1 INTRODUCTION

In the previous chapters, control methods that addressed the challenges of actuator redundancy and EMD were developed and tested either through simulations or experiments. Similarly to most controllers for FES-based systems, the developed control methods in chapters 3 and 4 did not consider the actuator dynamics. For FES-based systems these actuator dynamics refer to the Ca^{2+} activation dynamics that facilitate the muscle force generation and govern the speed of response of the or muscles in this case. Typically, these activation dynamics are ignored all together just like in chapters 3 and 4. A few researchers have considered the activation dynamics during the NMES control but they either use ad hoc methods that do not consider system stability or integrator backstepping technique which results in the requirement of acceleration signals in the controller.

The focus of this chapter is to expand the PID-DC controller developed in the previous section to a system that considers the activation dynamics. In order to consider these additional dynamics and avoid the requirement of acceleration signals, I opted to use the nonlinear control technique of dynamic surface control. This technique uses the dynamics of a low-pass filter in the control development to avoid the requirement of acceleration signal. Unlike IB, which takes an additional time derivative that leads to the requirement of an acceleration signal in the control law, DSC approximates the derivative of the desired control input by using the filter signals and the dynamics of the low-pass filter. The key contribution of this work is the first development of a DSC controller for NMES system and the incorporation of a delay compensation mechanism in the DSC framework. Until now

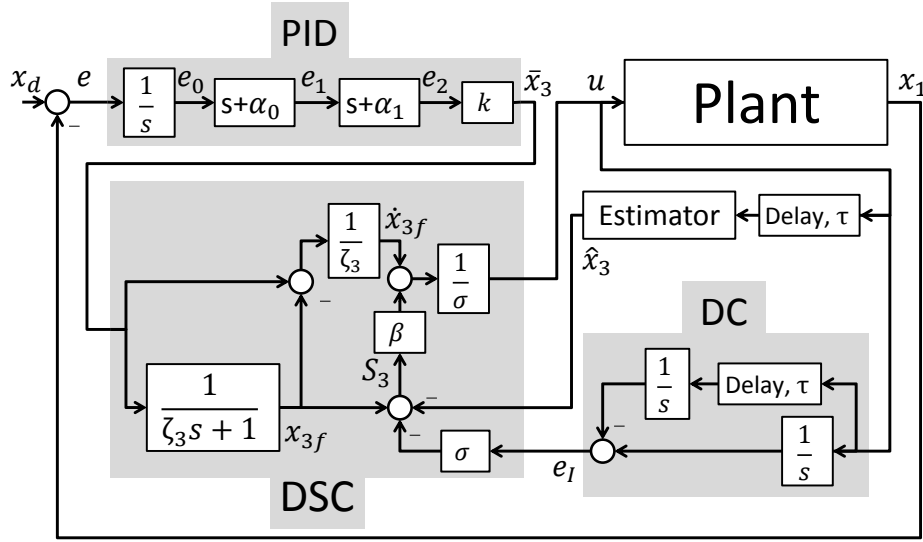


Figure 5.1: The control schematic for the implementation of the new PID-based DSC controller with delay compensation.

DSC has not been developed for systems with input delays. In addition, the DSC structure requires the use of the activation state which is unmeasurable in real-time implementation. Therefore, a model-based estimator is used to estimate the activation states during real-time control implementation. The second and third sections of this chapter will cover the control development and Lyapunov stability analysis of the newly derived PID-DSC controller. The fourth section will focus on validating the new controller by experimentally comparing it to the PID-DC on two able-bodied subjects and one subject with an SCI.

5.2 CONTROL DEVELOPMENT

To facilitate the control development, the musculoskeletal dynamics that include the activation dynamics in (2.5) are divided by Ω and their state space form can be written as

$$\begin{aligned}
\dot{x}_1 &= x_2, \\
\dot{x}_2 &= J_\Omega^{-1} [-f(x_1, x_2) - d_\Omega + x_3], \\
\dot{x}_3 &= -\omega x_3 + \omega u_\tau,
\end{aligned} \tag{5.1}$$

where $x_1 = q(t)$, $x_2 = \dot{q}(t)$, $x_3 = \mu(t)$, and $f(x_1, x_2) = M_{v\Omega} + M_{e\Omega} + M_{g\Omega}$.

5.2.1 Control Objective

The control objective is to track a continuously differentiable desired trajectory, $x_d(t) \in \mathbb{R}$.

To realize the control objective, the tracking error is defined as

$$e = x_d(t) - x_1(t). \tag{5.2}$$

To facilitate the control design and stability analysis, the auxiliary error signals $e_1(t)$, $e_2(t) \in \mathbb{R}$ are defined as

$$e_1 = \dot{e}_0 + \alpha_0 e_0, \tag{5.3}$$

$$e_2 = \dot{e}_1 + \alpha_1 e_1, \tag{5.4}$$

where $\alpha_0, \alpha_1 \in \mathbb{R}^+$ are control gains and $e_0 \in \mathbb{R}$ is an auxiliary signal defined as [29]

$$e_0 = \int_{t_0}^t e(s) ds \tag{5.5}$$

in order to incorporate integral control. To facilitate the control development and stability analysis, the following assumptions were made:

Assumption 1: The signals q , \dot{q} , are measurable.

Assumption 2: The nonlinear functions η and ς are non-zero, positive, bounded functions whose first time derivatives exist. Therefore, based on these assumptions, Ω is also non-zero, positive, bounded, and its first time derivative exists.

Assumption 3: Based on Assumption 2, the term, J , divided by Ω is bounded (i.e., $|J_\Omega| \leq \bar{J}_\Omega$) and its time derivative \dot{J}_Ω is also bounded.

Assumption 4: The unknown disturbance and unmodeled effects in the system are bounded (e.g., $|d| \leq \bar{d}$). Therefore, based on Assumption 2, d_Ω is also assumed to be bounded.

Assumption 5: The activation time constant is assumed to be bounded (i.e., $\omega \leq \gamma$). Also the estimate of the activation time constant is bounded as $0 < \hat{\omega} \leq \gamma$.

Assumption 6: The desired trajectory, $x_d \in \mathbb{R}$, and its derivatives, $\dot{x}_d, \ddot{x}_d \in \mathbb{R}$, are bounded.

5.2.2 Closed-Loop Error System

Multiplying the time derivative of (5.4) by J_Ω and using (5.1), (5.3), and (5.4) results in

$$J_\Omega \dot{e}_2 = J_\Omega \ddot{x}_d + f + d_\Omega - x_3 + J_\Omega \alpha_0 \ddot{e}_0 + J_\Omega \alpha_1 \dot{e}_1. \quad (5.6)$$

After adding and subtracting a desired signal $\bar{x}_3 \in \mathbb{R}$, a filtered version of the desired signal $x_{3f} \in \mathbb{R}$, a delay compensation term $e_I \in \mathbb{R}$ multiplied by a control gain σ , where $e_I = \int_{t-\tau}^t u(\theta) d\theta$, and an estimate of the activation constant $\hat{x}_3 \in \mathbb{R}$, and rearranging the terms, (5.6) becomes

$$J_\Omega \dot{e}_2 = -\frac{1}{2} \dot{J}_\Omega e_2 + S - \sigma e_I + y_3 + \tilde{x}_3 + \tilde{N} + \chi - \bar{x}_3 - e_1, \quad (5.7)$$

where the surface error, $S \in \mathbb{R}$, is defined as

$$S = x_{3f} - \hat{x}_3, \quad (5.8)$$

and the boundary layer error, $y_3 \in \mathbb{R}$, for x_3 is defined as

$$y_3 = \bar{x}_3 - x_{3f}, \quad (5.9)$$

and the estimation error, $\tilde{x}_3 \in \mathbb{R}$, is defined as

$$\tilde{x}_3 = \hat{x}_3 - x_3. \quad (5.10)$$

The estimate of the muscle activation is generated through a best guess model of the activation dynamics defined as

$$\dot{\hat{x}}_3 = -\hat{\omega} \hat{x}_3 + \hat{\omega} u_\tau. \quad (5.11)$$

In (5.7), the auxiliary signals $\tilde{N}(e_1, e_2, e_I, t) \in \mathbb{R}$ and $\chi(\Omega, t) \in \mathbb{R}$ are defined as

$$\tilde{N} = N - N_d, \quad \chi = N_d + d_\Omega,$$

$$N = \frac{1}{2} J_\Omega \dot{e}_2 + J_\Omega \ddot{x}_d + f + J_\Omega \alpha_0 (e_2 - (\alpha_1 + \alpha_0) e_1) - J_\Omega \alpha_0^3 e_0 + J_\Omega \alpha_1 (e_2 - \alpha_1 e_1) + e_1 + \sigma e_I,$$

$$N_d = J_{\Omega_d} \ddot{x}_d + f(x_d, \dot{x}_d),$$

where $J_{\Omega_d} = J/\Omega(x_d, \dot{x}_d)$. Based on Assumptions 3, 4, and 6 the auxiliary functions \tilde{N} and χ are bounded such that

$$|\tilde{N}| \leq \rho(\|z\|) \|z\|, \quad |\chi| \leq \epsilon, \quad (5.12)$$

where $\epsilon \in \mathbb{R}^+$ is a known constant, $\rho(\|z\|) \in \mathbb{R}$ is a positive globally invertible non-decreasing function, and $z(e_0, e_1, e_2, e_I) \in \mathbb{R}^4$ is defined as $z = [e_0, e_1, e_2, e_I]^T$. After designing the desired signal as

$$\bar{x}_3 = k e_2, \quad (5.13)$$

where $k = k_1 + k_2 + k_3$ and $k_1, k_2, k_3 \in \mathbb{R}^+$ are control gains.

Remark. The desired signal defined in (5.13) can be expressed in standard PID form as $K_P e + K_D \dot{e} + K_I \int_0^t e(\theta) d\theta$ where $K_P, K_D, K_I \in \mathbb{R}^+$ are the proportional, derivative, and integral control gains and are defined as $K_P = k(\alpha_0 + \alpha_1)$, $K_D = k$, and $K_I = k\alpha_0\alpha_1$.

After using the desired signal, (5.7) becomes

$$J_\Omega \dot{e}_2 = -\frac{1}{2} J_\Omega e_2 + S_3 + y_3 + \tilde{x}_3 + \tilde{N} + \chi - k e_2 - e_1, \quad (5.14)$$

where S_3 is the augmented surface error which now contains the delay compensation term σe_I and is defined as

$$S_3 = S - \sigma e_I.$$

The filtered desired signal x_{3f} is obtained by passing \bar{x}_3 through a low-pass filter such as

$$\zeta_3 \dot{x}_{3f} + x_{3f} = \bar{x}_3; \quad x_{3f}(0) = \bar{x}_3(0), \quad (5.15)$$

where $\zeta_3 \in \mathbb{R}^+$ is the low-pass filter time constant. The surface error dynamics are derived by taking the time derivative of (5.8) and using (5.1), resulting in

$$\dot{S}_3 = \dot{x}_{3f} + \hat{\omega} \hat{x}_3 - \sigma u + (\sigma - \hat{\omega}) u_\tau. \quad (5.16)$$

Remark. The delay compensation term e_I is used to replace the delayed input in the activation dynamics with a non-delayed input and is computed by integrating the past control inputs [6].

The control law u is designed to satisfy the subsequential stability analysis as

$$u = \frac{1}{\sigma} [\beta S_3 + \dot{x}_{3f}], \quad (5.17)$$

where $\beta \in \mathbb{R}^+$ is a control gain. Therefore, the closed-loop surface error dynamics can be written as

$$\dot{S}_3 = -\beta S_3 + \hat{\omega} \hat{x}_3 + (\sigma - \hat{\omega}) u_\tau. \quad (5.18)$$

The boundary layer error dynamics are found by taking the time derivative of (5.9) and using (5.15), results in

$$\dot{y}_3 = \eta - \frac{y_3}{\zeta_3}, \quad (5.19)$$

where $\eta(e_0, e_1, e_2, e_I, S_3, y_3, t)$ is a continuous nonlinear function defined as $\eta = \frac{d}{dt} [k e_2]$.

5.3 STABILITY ANALYSIS

Theorem 3. Consider the musculoskeletal system in (5.1) with an input delay in the activation dynamics. The control law in (5.17), when $0 \leq u \leq 1$, ensures uniformly ultimately bounded tracking

$$\|y(t)\| \leq \epsilon_0 \exp(-\epsilon_1 t) + \epsilon_2, \quad (5.20)$$

provided that the control gains k_1 , α_0 , α_1 , β , ζ_3 satisfy the following sufficient gain conditions:

$$\alpha_0 > \frac{1}{2}, \quad \alpha_1 > \frac{1}{2}, \quad k_1 > 1, \quad \frac{1}{\zeta_3} \geq \frac{1}{\kappa} \left[\frac{1}{2} + \frac{M^2}{2\epsilon} + k_o \right]$$

$$\beta \geq \max \left\{ \frac{1}{2} \left(\sqrt{\vartheta^2 + \frac{4\tau\zeta_3}{\hat{\omega}^2}} + \vartheta \right), \frac{1}{2} \left(\sqrt{(\tau\hat{\omega}^{-2})^2 + 4\tau\hat{\omega}^{-2}} + \tau\hat{\omega}^{-2} \right) \right\}$$

where τ is the EMD, k_o and ε are arbitrary constants, and M , ϑ , and κ are constants defined in the subsequent stability analysis.

Proof: Let $y(t) \in \mathbb{R}^6$ be defined as

$$y = \left[e_0 \ e_1 \ e_2 \ S_3 \ y_3 \ \sqrt{P} \right]^T.$$

A positive definite continuously differentiable Lyapunov functional candidate $V(y, t) : D \times [0, \infty) \rightarrow \mathbb{R}^+$ is defined as

$$V \triangleq \frac{1}{2}e_0^2 + \frac{1}{2}e_1^2 + \frac{1}{2}J_\Omega e_2^2 + \frac{1}{2}S_3^2 + \frac{1}{2}y_3^2 + P, \quad (5.21)$$

which satisfies the following inequalities

$$\lambda_1 \|y\|^2 \leq V \leq \lambda_2 \|y\|^2, \quad (5.22)$$

where $\lambda_1, \lambda_2 \in \mathbb{R}$ are positive constants. The Lyapunov-Krasovskii functional $P \in \mathbb{R}^+$ in (5.21) is defined as

$$P = \frac{\zeta_3}{\beta^2} \int_{t-\tau}^t \left(\int_s^t u(\theta)^2 d\theta \right) ds.$$

Taking the time derivative of (5.21) and using (5.4), (5.14), (5.18), and (5.19) results in

$$\begin{aligned} \dot{V} = & e_0(e_1 - \alpha_0 e_0) + e_1(e_2 - \alpha_1 e_1) + e_2 \left(-\frac{1}{2} \dot{J}_\Omega e_2 + S_3 + y_3 + \tilde{x}_3 + \tilde{N} + \chi - e_1 - k e_2 \right) \\ & + \frac{1}{2} \dot{J}_\Omega e_2^2 + S_3(-\beta S_3 + \hat{\omega} \hat{x}_3 + (\sigma - \hat{\omega})u_\tau) + y_3 \left(\eta - \frac{y_3}{\zeta_3} \right) + \frac{\zeta_3}{\beta^2} \tau u^2 - \frac{\zeta_3}{\beta^2} \int_{t-\tau}^t u(\theta)^2 d\theta. \end{aligned}$$

Canceling out the like terms, using (5.17), and rearranging the negative definite terms results in

$$\begin{aligned} \dot{V} = & -\alpha_0 e_0^2 - \alpha_1 e_1^2 - k e_2^2 - \beta S_3^2 - \frac{1}{\zeta_3} y_3^2 + e_0 e_1 + e_2 (S_3 + y_3 + \tilde{x}_3 + \tilde{N} + \chi) \quad (5.23) \\ & + S_3(\hat{\omega} \hat{x}_3 + (\sigma - \hat{\omega})u_\tau) + y_3 \eta + \frac{\zeta_3 \tau}{\beta^2 \sigma^2} (\beta^2 S_3^2 + 2\beta S_3 \dot{x}_{3f} + \dot{x}_{3f}^2) - \frac{\zeta_3}{\beta^2} \int_{t-\tau}^t u(\theta)^2 d\theta. \end{aligned}$$

After using (5.9), (5.12), and (5.15), (5.23) be bounded as

$$\begin{aligned}\dot{V} \leq & -\alpha_0 e_0^2 - \alpha_1 e_1^2 - k e_2^2 - (\beta - \tau \zeta_3 \sigma^{-2}) S_3^2 - \left(\frac{1}{\zeta_3} - \frac{\tau}{\zeta_3 \beta^2 \sigma^2} \right) y_3^2 + |e_0| |e_1| \\ & + |e_2| |S_3| + |e_2| |y_3| + |e_2| |\tilde{x}_3| + |e_2| \rho(\|z\|) \|z\| + |e_2| \epsilon + |S_3| |\hat{\omega} \hat{x}_3 + (\sigma - \hat{\omega}) u_\tau| \\ & + |y_3| |\eta| + \frac{2\tau}{\beta \sigma^2} |S_3| |y_3| - \frac{\zeta_3}{\beta^2} \int_{t-\tau}^t u(\theta)^2 d\theta.\end{aligned}$$

Using Young's inequality, Property 1, and Assumption 5 to bound the following terms

$$\begin{aligned}|e_0| |e_1| &\leq \frac{1}{2} e_0^2 + \frac{1}{2} e_1^2, \quad |e_2| |S_3| \leq \frac{1}{2} e_2^2 + \frac{1}{2} S_3^2, \\ |e_2| |y_3| &\leq \frac{1}{2} e_2^2 + \frac{1}{2} y_3^2, \quad |y_3| |\eta| \leq \frac{1}{2\varepsilon} y_3^2 \eta^2 + \frac{\varepsilon}{2}, \\ |S_3| |\hat{\omega} \hat{x}_3 + (\sigma - \hat{\omega}) u_\tau| &\leq \Psi |S_3| \leq \frac{\Psi^2}{2\varepsilon} S_3^2 + \frac{\varepsilon}{2}, \\ \frac{2\tau}{\beta \sigma^2} |S_3| |y_3| &\leq \frac{\tau \zeta_3}{\beta \sigma^2} S_3^2 + \frac{\tau}{\zeta_3 \beta \sigma^2} y_3^2,\end{aligned}$$

where $\varepsilon \in \mathbb{R}^+$ is a arbitrary constant, and rearranging the terms results in

$$\begin{aligned}\dot{V} \leq & -\left(\alpha_0 - \frac{1}{2}\right) e_0^2 - \left(\alpha_1 - \frac{1}{2}\right) e_1^2 - (k-1) e_2^2 - \left(\beta - \vartheta - \frac{\tau \zeta_3}{\beta \sigma^2}\right) S_3^2 - \left(\frac{\kappa}{\zeta_3} - \frac{1}{2}\right) y_3^2 \quad (5.24) \\ & + |e_2| \rho(\|z\|) \|z\| + |e_2| (\epsilon + 1) + \frac{1}{2\varepsilon} y_3^2 \eta^2 + \varepsilon - \frac{\zeta_3}{\beta^2} \int_{t-\tau}^t u(\theta)^2 d\theta,\end{aligned}$$

where $\vartheta = \frac{1}{2} + \frac{\Psi^2}{2\varepsilon} + \tau \zeta_3 \sigma^{-2}$ and $\kappa = 1 - \tau \sigma^{-2} \beta^{-1} - \tau \sigma^{-2} \beta^{-2}$. After defining ζ_3 such that

$$\frac{1}{\zeta_3} \geq \frac{1}{\kappa} \left[\frac{1}{2} + \frac{M^2}{2\varepsilon} + k_o \right], \quad (5.25)$$

where $k_o \in \mathbb{R}^+$ is a known constant and $M > 0$ is the maximum of η in the defined compact set $\Xi = \{h \in \mathbb{R}^6 \mid \|h\| < 2\sigma, h = [e_0, e_1, e_2, e_I, S_3, y_3]^T\}$ where $\sigma \in \mathbb{R}^+$ is a known constant, the previous equation becomes

$$\begin{aligned}\dot{V} \leq & -\left(\alpha_0 - \frac{1}{2}\right) e_0^2 - \left(\alpha_1 - \frac{1}{2}\right) e_1^2 - (k-1) e_2^2 - \left(\beta - \vartheta - \frac{\tau \zeta_3}{\beta \sigma^2}\right) S_3^2 - k_o y_3^2 \quad (5.26) \\ & + |e_2| \rho(\|z\|) \|z\| + \varepsilon + |e_2| (\epsilon + 1) - \left(1 - \frac{\eta^2}{M^2}\right) \frac{y_3^2 M^2}{2\varepsilon} - \frac{\zeta_3}{\beta^2} \int_{t-\tau}^t u(\theta)^2 d\theta.\end{aligned}$$

After adding and subtracting $\frac{(\rho(\|z\|)\|z\|)^2}{4k_2}$ and $\frac{\epsilon^2}{4k_3}$, performing nonlinear damping, and further bounding, (5.26) becomes

$$\begin{aligned} \dot{V} \leq & -(\alpha_0 - \frac{1}{2})e_0^2 - (\alpha_1 - \frac{1}{2})e_1^2 - (k_1 - 1)e_2^2 - \left(\beta - \vartheta - \frac{\tau\zeta_3}{\beta\sigma^2}\right)S_3^2 - k_oy_3^2 \\ & + \frac{(\rho(\|z\|)\|z\|)^2}{4k_2} + \frac{(\epsilon + 1)^2}{4k_3} + \varepsilon - \frac{\zeta_3}{\beta^2} \int_{t-\tau}^t u(\theta)^2 d\theta. \end{aligned} \quad (5.27)$$

Further, by splitting the integral term and using the Cauchy Schwarz inequality

$$e_I^2 \leq \tau \int_{t-\tau}^t u(\theta)^2 d\theta$$

the following term can be bounded as

$$-\frac{\zeta_3}{2\tau\beta^2} \left(\tau \int_{t-\tau}^t u(\theta)^2 d\theta \right) \leq -\frac{\zeta_3}{2\tau\beta^2} e_I^2.$$

Therefore, (5.27) results in

$$\begin{aligned} \dot{V} \leq & -\left\{ \psi - \frac{\rho(\|z\|)^2}{4k_2} \right\} \|z\|^2 - \left(\beta - \vartheta - \frac{\tau\zeta_3}{\beta\sigma^2}\right)S_3^2 - k_oy_3^2 + \frac{(\epsilon + 1)^2}{4k_3} \\ & + \varepsilon - \frac{\zeta_3}{2\beta^2} \int_{t-\tau}^t u(\theta)^2 d\theta \end{aligned} \quad (5.28)$$

where $\psi = \min \left\{ \alpha_0 - \frac{1}{2}, \alpha_1 - \frac{1}{2}, k_1 - 1, \frac{\zeta_3}{2\tau\beta^2} \right\}$. Because

$$\begin{aligned} \int_{t-\tau}^t \left(\int_s^t u(\theta)^2 d\theta \right) ds & \leq \tau \sup_{s \in [t, t-\tau]} \left[\int_s^t u(\theta)^2 d\theta \right] \\ & = \tau \int_{t-\tau}^t u(\theta)^2 d\theta, \end{aligned}$$

(5.28) can be rewritten as

$$\dot{V} \leq -\left\{ \psi - \frac{\rho(\|z\|)^2}{4k_2} \right\} \|z\|^2 - \left(\beta - \vartheta - \frac{\tau\zeta_3}{\beta\sigma^2}\right)S_3^2 - k_oy_3^2 + \frac{(\epsilon + 1)^2}{4k_3} + \varepsilon - \frac{1}{2\tau}P.$$

Using the definitions of $y(t)$ and $z(t)$ this expression can be upper bounded as

$$\dot{V} \leq -\bar{\psi}\|y\|^2 - \left\{ \psi - \frac{\rho(\|z\|)^2}{4k_2} \right\} \|e_I\|^2 + \nu, \quad (5.29)$$

where $\nu = \frac{(\epsilon+1)^2}{4k_3} + \varepsilon$ and $\bar{\psi}(\|z\|) \in \mathbb{R}^+$ is

$$\bar{\psi} = \min \left\{ \left(\psi - \frac{\rho(\|z\|)^2}{4k_2} \right), \left(\beta - \vartheta - \frac{\tau\zeta_3}{\beta\sigma^2} \right), k_o, \frac{1}{2\tau} \right\}.$$

This expression can be further bounded if $\psi - \frac{\rho(\|z\|)^2}{4k_2} > 0$, which is true if the condition $\|z\|^2 < \rho^{-2}(2\sqrt{\psi k_2})$ is satisfied. Considering (5.22), the definitions of y and z , and $P > \frac{\zeta_3}{\tau\beta^2} e_1^2$, a set \mathcal{S} can be defined as

$$\mathcal{S} \triangleq \left\{ y(t) \in \mathbb{R}^6 \mid \|y(0)\| < \sqrt{\frac{\lambda_1}{\lambda_2} \left[\min \left\{ 1, \frac{\zeta_3}{\tau\beta^2} \right\} \rho^{-2} \left(2\sqrt{\psi k_2} \right) - \nu \right]} \right\}.$$

In \mathcal{S} , $\bar{\psi}(\|z\|)$ can be lower bounded by a constant $\delta \in \mathbb{R}^+$ as $\delta \leq \bar{\psi}(\|z\|)$. By further utilizing (5.22), (5.29) can be written as

$$\dot{V} \leq -\frac{\delta}{\lambda_2} V + \nu. \quad (5.30)$$

For $y(0) \in \mathcal{S}$, the linear differential equation in (5.30) can be solved as

$$V(y, t) \leq V(0)e^{-\frac{\delta}{\lambda_2}t} + \frac{\nu\lambda_2}{\delta} \left(1 - e^{-\frac{\delta}{\lambda_2}t} \right). \quad (5.31)$$

Based on (5.31) and (5.22), the condition in Theorem 1, (5.20), can be restated as

$$\|y(t)\| \leq \sqrt{\frac{\lambda_2}{\lambda_1} \left(\|y(0)\|^2 - \frac{\nu}{\delta} \right) e^{-\frac{\delta}{2\lambda_2}t} + \frac{\lambda_2\nu}{\lambda_1\delta}}. \quad (5.32)$$

Using this expression, the definition of $y(t)$, and (5.3), an explicit bound on the tracking error $e(t)$ can be derived as

$$\|e(t)\| \leq (1 + \alpha_0) \left(\sqrt{\frac{\lambda_2}{\lambda_1} \left(\|y(0)\|^2 - \frac{\nu}{\delta} \right) e^{-\frac{\delta}{2\lambda_2}t} + \frac{\lambda_2\nu}{\lambda_1\delta}} \right). \quad (5.33)$$

■

5.4 EXPERIMENTAL PROTOCOL

As previously stated, we hypothesize that the consideration of the activation dynamics in the control development and the use of DSC would improve the control performance. To test this hypothesis and demonstrate the efficacy of the newly developed PID-DSC controller and the impact of the DSC component of the controller, it was experimentally compared with its predecessor, the PID-DC. The new controller was compared to the PID-DC because both controllers are feedback based controllers that were 1) developed for nonlinear musculoskeletal system, 2) used Lyapunov control methods, and 3) because the PID-DC was developed under the assumption of no activation dynamics. These experiments were conducted on both legs of two able bodied subjects, referred to as A1 and A2 (2 males; Ages: 21 and 27 years), and one leg of a subject with T10 AIS A paraplegia from an SCI, referred to as S1 (Age: 41), on a modified leg extension machine. Prior to any experimentation, an approval from the Institutional Review Board at the University of Pittsburgh was obtained. During the experiments, the subjects were instructed to relax and refrain from voluntary interfering during the electrical stimulation. Both controllers require the EMD value and the new controller needs the activation time constant for the activation state estimator. These values were determined using a simple system identification experiment.

To identify the EMD value, τ , and the activation decay constant, \hat{w} , the subject was seated in the LEM in an isometric configuration and a step input was applied to the quadriceps. A three step procedure was used to extract the parameters from the input signal and the force measurements, as seen in Fig. 5.2. In the first step, the EMD value was determined by observing the difference in time from when the stimulation is applied to when the measured force begins to increase. In the second step, the normalized torque measurement was shifted by the EMD value to account for the EMD in the input. In the third step, assuming that the activation function is a first order system, the activation decay constant was identified by finding the decay constant that produced the smallest error between the shifted normalized torque measurement and the normalized response of the first order system to a normalized step input.

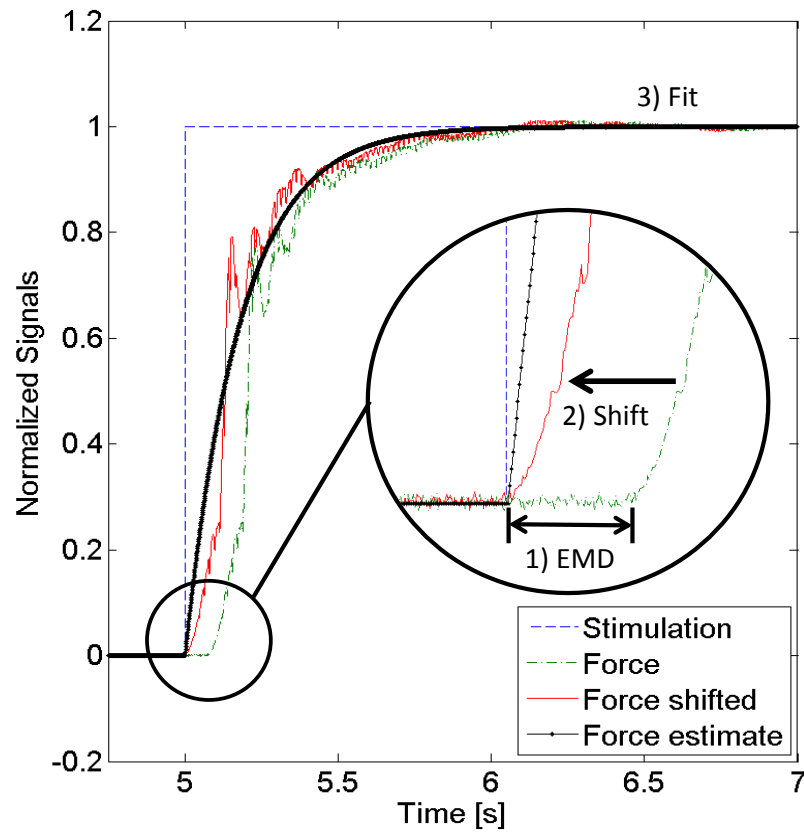


Figure 5.2: A visual representation of the 3 step data processing of the system identification experiments. Step 1: find the EMD value. Step 2: shift the measured force signal. Step 3: find the activation time constant that produces the best fit.

After the necessary parameters were identified, the two controllers were tested on each subject to track a sinusoidal signal with a period of 4-seconds and alternating peaks. The desired trajectory was designed to start at the equilibrium position and oscillated between a minimum amplitude of 5° and an alternating maximum amplitude of 50° and 35° . The alternating peaks were used to reduce the chance of the subjects anticipating the desired motion and subconsciously interfering with the performance of the controller. Each controller was evaluated in five consecutive trials for each combination of subject, leg, and controller. A rest period of 3 minutes was allotted in between the 30 second trials to prevent the subjects from fatiguing. Also, the subjects were not allowed to view the desired trajectory or the performance in real-time.

A limitation of experimenting with NMES on human subjects is that the gain tuning procedure could only be done over a finite time period as the muscles begin to fatigue and may cause subject discomfort. To bypass this limitation the two controllers were tuned on a separate day to find an initial guess for the control gains. Then before conducting the five trials for each controller, the controller was further tuned beginning at the initial guess for a short period of time until the error over a 10 second trial was minimized. The controllers were tuned using trial and error; some observations on the tuning process are addressed in the discussion section.

5.5 EXPERIMENTAL RESULTS

The experimental results for the tracking experiments are presented in Fig. 5.3 & 5.4 and Table 5.1. To quantify the performance of each controller the root mean squared error (RMSE), root mean squared steady state error (SSRMSE), and the root mean squared current (RMSC), normalized by the body mass index of the subject to account for possible variance in subject size, are used as the metrics. The measured EMD, estimated activation decay constant, average RMSE, average SSRMSE, and average RMSC are presented in Table 5.1. The desired and actual positions, tracking error, and stimulation input for the best trial for each controller are shown in Fig. 5.3 (a) and (b). The best trial for the PID-DSC was

on subject A1's right leg and resulted in an RMSE of 2.89° and SSRMSE of 2.10° and the best trial for the PID-DC was on subject A2's right leg and resulted in an RMSE of 3.14° and SSRMSE of 3.22° . In addition, the best trial for each controller on subject S1s left leg are shown in Fig. 5.4. From the tabulated results, the PID-DSC produced smaller RMSE in 4 out of the 5 sets of data, and smaller SSRMSE in all 5 sets, however, the RMSC produced mixed results. A two sample paired t-test was performed to determine if the differences in the criteria were statistically significant at a 95% confidence level. The statistical analysis determined that the PID-DSC statistically outperformed the PID-DC in the RMSE (p-value = $3.12e-4$) and SSRMSE (p-value = $1.49e-4$) criteria but not in the RMSC (p-value = $6.29e-1$) criterion. The mean of each criterion and its standard error for each controller are presented in Fig. 5.3 (c).

5.6 CONCLUSION

In this chapter, a PID-based tracking controller for musculoskeletal systems with input delays in the activation dynamics is presented. The controller uses a DSC structure to deal with the activation dynamics which are cascaded to the musculoskeletal dynamics. Model-based estimators are used to estimate the unmeasurable activation states in real-time implementation. In addition, a delay compensation term was used to deal with the input delay in the activation dynamics. A Lyapunov stability analysis was performed to prove UUB tracking performance. The controller was experimentally validated on two able-bodied subjects and compared with its predecessor, the PID-DC, which is a PID-based controller that compensates for EMD but does not consider activation dynamics. A t-test statistical analysis was performed and determined that the PID-DSC outperformed the PID-DC at a 95% confidence level.

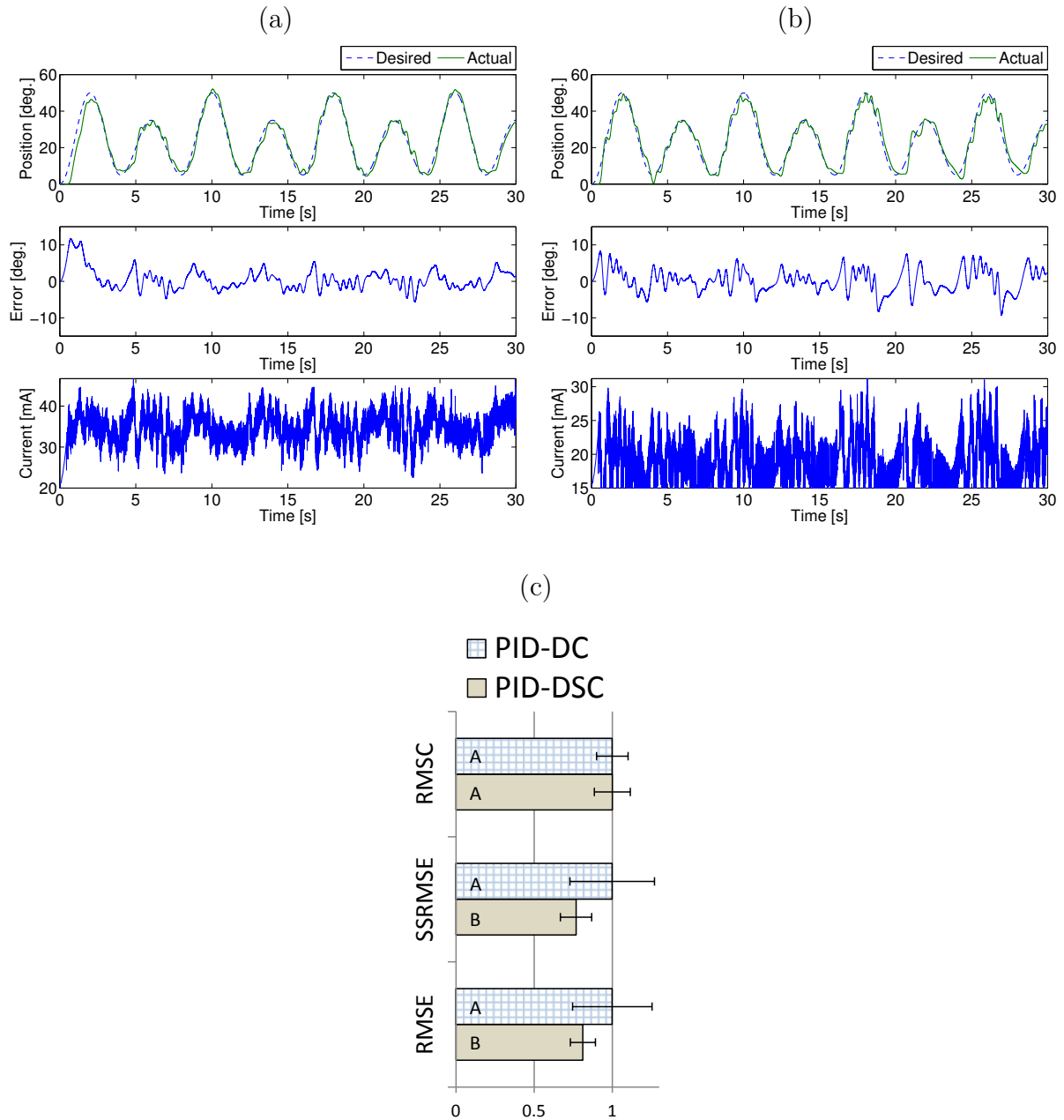


Figure 5.3: Experimental results obtained from the best trial for each controller: (a) PID-DSC and (b) PID-DC. These plots show the desired & actual angular position (top plots), error (middle plots), and stimulation current amplitude (bottom plots). (c) A graphical representation of the results from the LEM experiments. The three criteria: RMSE, SSRMSE, and RMSC were used to compare the controllers. The error bars show the standard error of the mean for each criteria. Miss-matching letters (A & B) indicate statistically significant differences between the controllers at a 95% confidence levels.

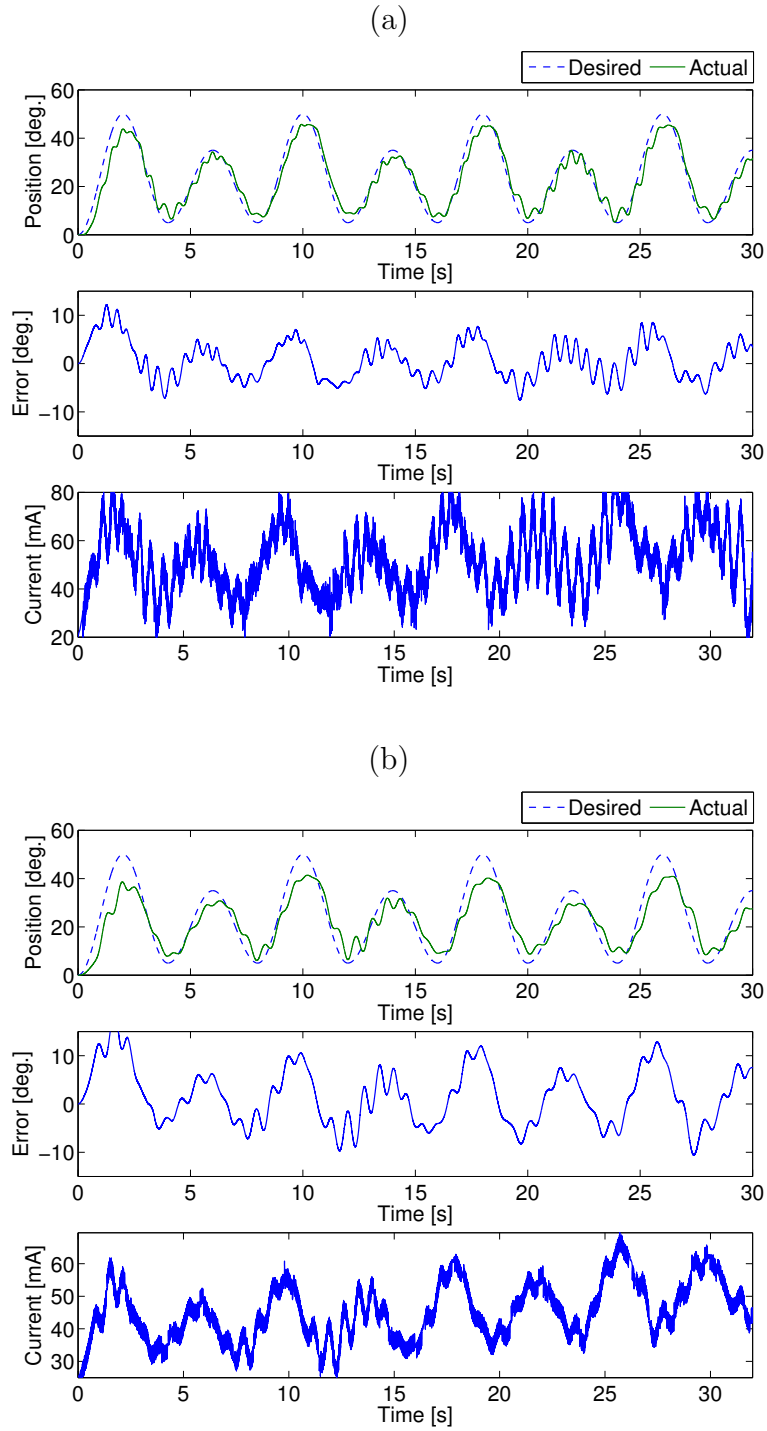


Figure 5.4: Experimental results obtained from the best trial for each controller: (a) PID-DSC and (b) PID-DC on subject S1. These plots show the desired & actual angular position (top plots), error (middle plots), and stimulation current amplitude (bottom plots).

Table 5.1: The tabulated results for the 4 second trajectory experiments include the EMD measured for each volunteer subject (S), the average root mean squared error (RMSE), the average steady state RMS error (SSRMSE), and the average RMS Current (RMSC) normalized by the body mass index of each subject.

S	Leg	EMD [ms]	\hat{w} [s]	AVG RMSE [deg.]		AVG SSRMSE [deg.]		AVG RMSC [$\frac{mAm^2}{kg}$]	
				PID-DSC	PID-DC	PID-DSC	PID-DC	PID-DSC	PID-DC
A1	R	91	4.2	3.39	4.39	2.94	3.48	1.37	1.51
	L	89	4.7	3.89	4.52	3.46	4.12	1.57	1.68
A2	R	80	3.9	3.63	3.51	3.17	3.50	0.73	0.72
	L	84	6.2	3.54	3.86	2.85	3.54	1.01	0.97
S1	L	78	10.4	4.23	6.73	3.85	6.51	2.35	2.04
AvG	-	84.4	5.88	3.74	4.60	3.25	4.23	1.40	1.38

6.0 HUMAN MOTOR CONTROL-INSPIRED SYNERGY-BASED PID-DSC CONTROLLER WITH DELAY COMPENSATION

6.1 INTRODUCTION

In the previous chapters, the derivation and validation of control methods that address three of the four challenges associated with the real-time control of walking hybrid neuroprostheses are presented. In chapter 3 human motor control inspired synergy-based controller is derived to solve the actuator redundancy problem. Then chapter 4 addressed the EMD by augmenting the standard PID controller with a delay compensation term. This delay compensation term is the integral of the past control law over a time duration equal to the input delay and is used to modified the control input by removing excess ill-timed control effort. Later in chapter 4, this PID-DC controller is extended to consider the third challenge, the actuator dynamics of the system, by incorporating dynamic surface control to the error structure. The last challenge to be addressed is the rapid onset of muscle fatigue when the muscles are artificially stimulated. In addition, a control system that combines the control techniques from the last three chapters has to be derived and tested for the overall system.

In this chapter the derivation of an adaptive synergy-based PID-DSC tracking controller with delay compensation for a hybrid neuroprosthesis with actuator redundancy, EMD, actuator dynamics, and muscle fatigue is presented. This is done by combining the different techniques developed in chapters 3, 4, and 5. This control scheme solves the actuator redundancy problem by using the adaptive synergy-based feedforward component developed in the chapter 3 to provide the rough input profile for all the actuators. Then PID-based feedback control of the motors is used to increase the robustness of the controller and to provide better tracking control. The synergies are extracted using principle component analysis on optimal

activations, which are pre-computed through dynamic optimizations of a hybrid lower-limb and exoskeleton model [92]. The synergies with the least reconstruction variance were truncated to reduce the amount of signals needed during online implementation. The synergy activation profiles were modified online using an adaptive update law to compensate for any unmodeled phenomena or parametric changes in the system. Because the actuator dynamics were considered in the control development, the DSC framework presented in Chapter 5 was used to avoid the requirement of acceleration signals in the controller.

To address the challenge of muscle fatigue, the feedforward and feedback terms are scaled up by the inverse of the fatigue estimate to maintain the effectiveness of the feedforward component as the muscles fatigues. In addition, a scaling factor gain is added to the feedforward component in case there is mismatch in model strength and the subjects during experiments. The fatigue and activation states are not measurable, so model-based estimators was designed to estimate the signals for real-time implementation of the controller. Sections 6.2 and 6.3 present the control development and Lyapunov stability analysis. In section 6.4, a simulation study was performed on the 2-DOF fixed hip model to show the efficacy of the newly developed controller. In section 6.5, the controller was then tested in preliminary experiments on an able-bodied male subject in the fixed-hip configuration. Section 6.6 and 6.7 concludes this chapter with a discussion and conclusion. Note that the simulation and experimental results presented in this chapter are based on a previous version of the controller where no integral control is present even though the control development includes integral control.

6.2 CONTROL DEVELOPMENT

6.2.1 Control Objective

The control objective is to track a continuously differentiable desired trajectory $q_d \in \mathbb{R}^n$. The tracking error, $e \in \mathbb{R}^n$, is defined as

$$e \triangleq q_d - q. \tag{6.1}$$

To facilitate the control design and stability analysis, the auxiliary error signal $e_1(t)$, $r(t) \in \mathbb{R}^n$ is defined as

$$e_1 \triangleq \dot{e}_0 + \alpha_0 e_0, \quad (6.2)$$

$$r \triangleq \dot{e}_1 + \alpha_1 e_1, \quad (6.3)$$

where $\alpha_0, \alpha_1 \in \mathbb{R}^+$ are control gains and $e_0(t) \in \mathbb{R}^n$ is an auxiliary signal defined as [29]

$$e_0 \triangleq \int_{t_0}^{t_f} e(s) ds, \quad (6.4)$$

in order to incorporate integral control. To simplify the derivations, the following notations are used: (1) the time dependence of a function is dropped (e.g., $e(t) \rightarrow e$) and (2) a signal delayed by τ is notated as a subscript (e.g., $e(t - \tau) \rightarrow e_\tau$). In addition, to facilitate the control development and stability analysis, the following assumptions were made.

Assumption 1: Only motion in the saggital plane is considered and the ankle joint is locked by an orthosis.

Assumption 2: The unmodeled effects or disturbances, τ_d , are bounded as $|\tau_d| \leq \epsilon_1$ where $\epsilon_1 \in \mathbb{R}^+$ is a constant.

Assumption 3: The transformation coefficients in the matrix, W , are bounded constants and the principal components, c_d , are bounded vectors. The reconstruction error μ_{loss} which accounts for the loss of variability in the activation profile data is bounded.

Assumption 4: The desired trajectory, $q_d \in \mathbb{R}^n$, and its derivatives, $\dot{q}_d, \ddot{q}_d \in \mathbb{R}^n$, are bounded.

6.2.2 Synergy Extraction

Let $\mu_d(t) \in \mathbb{R}^{3n}$ be the desired intermediate normalized activation variable vector containing desired muscle activation and motor current levels. This activation variable vector can be computed using dynamic optimizations [92]. Below, the dynamics, excluding the fatigue factor ϕ , are written in terms of the desired control and kinematic trajectories as

$$\begin{aligned}
M(q_d)\ddot{q}_d + C(q_d, \dot{q}_d)\dot{q}_d + G(q_d) + f(q_d, \dot{q}_d) \\
\equiv b(q_d, \dot{q}_d)\mu_d(t).
\end{aligned} \tag{6.5}$$

Further, by using PCA, the possibly correlated optimal activations, μ_d , can be transformed into a set of linearly correlated synergy activations, c_d , using the synergies W such as

$$\mu_d = Wc_d(t) + \mu_{loss}, \tag{6.6}$$

where the rows in $W \in \mathbb{R}^{3n \times p}$ are the synergies and $c_d(t) \in \mathbb{R}^p$ are the first p synergy activation coefficients. PCA is a statistical procedure that uses an orthogonal transformation, i.e., multiplying by W , to transform an ensemble of signals into linearly correlated signals also known as principal components (synergy activation coefficients). The principal components are ordered such that the first synergy and its activation coefficient accounts for most of the variance of the original signal, the second pair accounts for the second most, and so on. This allows the use of p synergies, where $p < 3n$, to reconstruct μ_d to over a 90% match. After disregarding the $3n - p$ synergies, there will be a mismatch between the reconstructed activation profiles, Wc_d , and the optimal activation profiles μ_d . This reconstruction error is quantified as μ_{loss} , as given in (6.6).

6.2.3 Closed-Loop Error System

The open-loop error is derived by multiplying the time derivative of (6.3) with $M(q)$ and substituting the dynamics in (2.10) and (2.12) to obtain

$$M\dot{r} = M\dot{q}_d + C\dot{q} + G + f + d - b\phi\mu + M\alpha_0\ddot{e}_0 + M\alpha_1\dot{e}_1. \tag{6.7}$$

This expression can be written in the form

$$M\dot{r} = -Cr + \tilde{N} + N_d + d - b\phi\mu - e_1 - b_a\phi e_I, \tag{6.8}$$

where $e_I \in \mathbb{R}^{3n}$, is defined as $e_{I_{i_j}} \triangleq \int_{t-\tau_{i_j}}^t u_{i_j}(\theta) d\theta$ for each actuator and $\tilde{N} \in \mathbb{R}^n$, is defined as $\tilde{N} \triangleq N - N_d$ and the auxiliary signals $N(q, \dot{q}, e, \dot{e}, e_I, t)$ and $N_d(t)$ are defined as

$$N \triangleq M\ddot{q}_d + C(\dot{q}_d + (\alpha_0 + \alpha_1)e_1 - \alpha_0^2 e_0) + G + f + M\alpha_0(r - (\alpha_1 + \alpha_0)e_1 + \alpha_0^2 e_0) \\ + M\alpha_1(r - \alpha_1 e_1) + e_1 + b_d \phi e_I,$$

$$N_d \triangleq M(q_d)\ddot{q}_d + C(q_d, \dot{q}_d)\dot{q}_d + G(q_d) + f(q_d, \dot{q}_d).$$

The term \tilde{N} in (6.8) can be upper bounded by using the Mean Value Theorem as

$$\|\tilde{N}\| \leq \rho_1(\|z\|) \|z\|, \quad (6.9)$$

where $\rho_1(\|z\|) \in \mathbb{R}$ is a positive monotonic bounded function and $z \in \mathbb{R}^{6n}$ is defined as

$$z = [e_0^T \quad e_1^T \quad r^T \quad e_I^T]^T.$$

Note that the auxiliary signal N_d is equal to the left hand side of the desired muscle dynamics in (6.5). Therefore, (6.8) can be rewritten as

$$M\dot{r} = -Cr + \tilde{N} + d + b_d \mu_d - b\phi\mu - e_1 - b_d \phi e_I. \quad (6.10)$$

After adding and subtracting the terms $b_d \hat{\phi} \bar{\mu}$, $b_d \phi \bar{\mu}$, $b_d \phi \hat{\mu}$, $b_d \phi \mu$, and $b_d \phi \mu_f$ where $b_d = b(q_d, \dot{q}_d)$, $\hat{\mu} \in \mathbb{R}^{3n}$ and $\hat{\phi} \in \mathbb{R}^{3n \times 3n}$ are estimates of the activation state and the fatigue state, $\bar{\mu} \in \mathbb{R}^{3n}$ is the desired activation to be later defined, and $\mu_f \in \mathbb{R}^{3n}$ is a filtered desired activation, and rearranging the terms, (6.10) becomes

$$M\dot{r} = -Cr + b_d \phi S + b_d \phi y + \tilde{N} + d + b_d \mu_d + \tilde{b} \phi \mu + b_d \phi \tilde{\mu} + b_d \tilde{\phi} \bar{\mu} - b_d \hat{\phi} \bar{\mu} - e_1, \quad (6.11)$$

where $\tilde{b} \in \mathbb{R}^{n \times 3n}$ is defined as $\tilde{b} \triangleq b_d - b$, $\tilde{\phi} \in \mathbb{R}^{3n \times 3n}$ is defined as $\tilde{\phi} \triangleq \hat{\phi} - \phi$, and $\tilde{\mu} \in \mathbb{R}^{3n}$ is defined as $\tilde{\mu} \triangleq \hat{\mu} - \mu$.

The estimates of the activation and fatigue states in (2.15) and (2.17) are generated through the following dynamics

$$\dot{\hat{\mu}}_{i_j} = -\hat{w}_{i_j} \hat{\mu}_{i_j} + \hat{w}_{i_j} u_{i_j}(t - \tau_{i_j}), \quad (6.12)$$

$$\dot{\hat{\phi}}_{i_j} = \frac{1}{\hat{T}_{f_{i_j}}}(\hat{\phi}_{\min_{i_j}} - \hat{\phi}_{i_j})\hat{\mu}_{i_j} + \frac{1}{\hat{T}_{r_{i_j}}}(1 - \hat{\phi}_{i_j})(1 - \hat{\mu}_{i_j}), \quad (6.13)$$

where \hat{w}_{i_j} , \hat{w}_i , $\hat{T}_{f_{i_j}}$, $\hat{T}_{r_{i_j}}$, and $\hat{\phi}_{\min_{i_j}}$ are bounded estimates of the real parameters that can be determined through system identification. Note that these estimators are governed by first-order differential equations, thus the estimates are bounded as $\hat{\mu} \in [u_{\min}, u_{\max}]$ and $\hat{\phi} \in [\hat{\phi}_{\min}, 1]$.

In (6.11), the surface error, $S \in \mathbb{R}^{3n}$, is defined as

$$S \triangleq \mu_f - \hat{\mu} - e_I, \quad (6.14)$$

and the boundary layer error, $y \in \mathbb{R}^{3n}$, for μ is defined as

$$y \triangleq \bar{\mu} - \mu_f. \quad (6.15)$$

The filtered desired activation μ_f is obtained by passing $\bar{\mu}$ through a low-pass filter such as

$$\zeta_f \dot{\mu}_f + \mu_f = \bar{\mu}; \quad \mu_f(0) = \bar{\mu}(0), \quad (6.16)$$

where $\zeta_f \in \mathbb{R}^+$ is the low-pass filter time constant. The delay compensation term, e_I , is added to the surface error, S , to deal with the input delay in the actuator dynamics.

After designing the desired activation, $\bar{\mu}$, as

$$\bar{\mu} = \hat{\phi}^{-1} [\zeta_{sf} W \hat{c} + kr], \quad (6.17)$$

where $\hat{c} \in \mathbb{R}^p$ is the estimate of c_d , $\zeta_{sf} \in \mathbb{R}^{3n \times 3n}$ is a control gain matrix and $k \in \mathbb{R}^{3n \times n}$ is the feedback gain matrix that is chosen to only influence the electric motors.

Remark. *The desired feedback activation, kr , defined in (6.17) can be expressed in standard PID form as $K_P e + K_D \dot{e} + K_I \int_0^t e(\theta) d\theta$ where K_P , K_D , $K_I \in \mathbb{R}^+$ are the proportional, derivative, and integral control gains and are defined as $K_P = k(\alpha_0 + \alpha_1)$, $K_D = k$, and $K_I = k\alpha_0\alpha_1$.*

In $\bar{\mu}$, the feedforward component, $\zeta_{sf}W\hat{c}$, and the feedback component, kr , are scaled by the inverse of the fatigue estimate. This feature is included in the controller so that as a muscle fatigues, the stimulation input to that muscle increases gradually to counteract the effects of the fatigue. The estimate of the synergy activation updates according to the following update law with the projection algorithm

$$\dot{\hat{c}} = \text{proj} \left(\dot{c}_d + FW^T \zeta_{sf}^T b_d^T r \right), \quad (6.18)$$

where $F \in \mathbb{R}^{p \times p}$ is a symmetric positive definite gain matrix. After using (6.6) and (6.17), (6.11) becomes

$$\begin{aligned} M\dot{r} = & -Cr + b_d\phi S + b_d\phi y + \tilde{N} + d + b_d\zeta_{sf}W\tilde{c} + b_d(I - \zeta_{sf})Wc_d \\ & + b_d\mu_{loss} + \tilde{b}\phi\mu + b_d\phi\tilde{\mu} + b_d\tilde{\phi}\hat{\phi}^{-1}\zeta_{sf}W\hat{c} + b_d\tilde{\phi}\hat{\phi}^{-1}kr - b_dkr - e_1, \end{aligned} \quad (6.19)$$

where $\tilde{c} \in \mathbb{R}^p$ is defined as

$$\tilde{c} = c_d - \hat{c}.$$

Using the Mean Value Theorem, Assumption 4, and the property of projection algorithm the following terms can be bounded as

$$\begin{aligned} \left\| \tilde{b}\phi\mu \right\| & \leq \rho_2(\|z\|) \|z\|, \quad \|b_d\| \leq \zeta, \\ \left\| b_d\mu_{loss} + b_d(I - \zeta_{sf})Wc_d \right\| & \leq \epsilon_2, \quad \left\| b_d\tilde{\phi}\hat{\phi}^{-1}\zeta_{sf}W\hat{c} \right\| \leq \epsilon_3 \end{aligned} \quad (6.20)$$

where $\rho_2(\|z\|) \in \mathbb{R}$ is a positive monotonically increasing bounded function and $\epsilon_2, \epsilon_3, \zeta \in \mathbb{R}^+$ are constants.

The surface error dynamics are derived by taking the time derivative of (6.14) and using (6.12), resulting in

$$\dot{S} = \dot{\mu}_f + \hat{w}\hat{\mu} - \hat{w}u_\tau - (u - u_\tau). \quad (6.21)$$

Based on the subsequent stability analysis, the normalized input u is designed as

$$u = \beta S + \dot{\mu}_f, \quad (6.22)$$

where $\beta \in \mathbb{R}^+$ is a control gain.

Remark. Note that in the overall controller v , the DSC component which is tuned through ζ_f could potentially amplify the feedforward component, $W\hat{c}$. To avoid this, the feedforward component, $W\hat{c}$, in the definition of $\bar{\mu}$ was scaled by ζ_{sf} in anticipation of this amplifying effect. In addition, this gain could be used to scale down or up the feedforward signals if there is a mismatch between the strength of a subject and the model used to compute the feedforward signals. This scaling factor gain will also give the user control over the relative amount of stimulation and motor effort used in the overall controller.

Therefore, the closed-loop surface error dynamics can be written as

$$\dot{S} = -\beta S + \hat{w}\hat{\mu} + (1 - \hat{w})u_\tau. \quad (6.23)$$

The boundary layer error dynamics are found by taking the time derivative of (6.15) and using (6.16), which results in

$$\dot{y} = \eta - \frac{y}{\zeta_f}, \quad (6.24)$$

where $\eta(e, r, S, y, t)$ is a continuous nonlinear function defined as $\eta = \frac{d}{dt} [\bar{\mu}]$. Based on the definition of u in (6.22), the control law v is designed as

$$v = \left[\beta S + \frac{\hat{\phi}^{-1} [\zeta_{sf} W\hat{c} + kr] - \mu_f}{\zeta_f} - u_{min} \right] \frac{v_{max} - v_{min}}{u_{max} - u_{min}} + v_{min}. \quad (6.25)$$

6.3 STABILITY ANALYSIS

Theorem 4. The controller designed in (6.17), (6.18), and (6.25), when $v_{min} \leq v \leq v_{max}$, ensures uniformly ultimately bounded tracking

$$\|y(t)\| \leq \epsilon_0 \exp(-\epsilon_1 t) + \epsilon_2, \quad (6.26)$$

provided that the following gain conditions are met:

$$K_{min} > \frac{(\rho_1(\|z\|) + \rho_2(\|z\|))^2}{2\zeta}, \quad \gamma_{min} \{b_d k - \Lambda\} > 0, \quad \beta > \vartheta + \frac{\bar{\tau}\zeta_f}{\beta},$$

$$\alpha_0 > \frac{1}{2}, \quad \alpha_1 > \frac{1}{2}$$

where $\gamma_{\min}\{\cdot\}$ denotes the minimum eigenvalue of a square matrix and K_{\min} , ϑ , $\bar{\tau} \in \mathbb{R}^+$ are subsequently defined constants.

Proof. To prove stability, choose a continuously differentiable Lyapunov candidate $V(x, t) \in \mathbb{R}$, defined as

$$V = \frac{1}{2}e_0^T e_0 + \frac{1}{2}e_1^T e_1 + \frac{1}{2}r^T M r + \frac{1}{2}S^T S + \frac{1}{2}y^T y + \frac{1}{2}\tilde{c}^T F^{-1}\tilde{c} + P. \quad (6.27)$$

The Lyapunov candidate V can be lower and upper bounded as

$$\lambda_1 \|x\|^2 \leq V \leq \lambda_2 \|x\|^2 + \Upsilon, \quad (6.28)$$

where Υ , λ_1 , $\lambda_2 \in \mathbb{R}^+$ are constants and $x = [e_0^T \ e_1^T \ r^T \ S^T \ y^T \ \sqrt{P}]^T$. The Lyapunov-Krasovskii functional $P \in \mathbb{R}^+$ is defined as

$$P = \frac{\zeta_f}{\beta^2} \int_{t-\bar{\tau}}^t \left(\int_s^t u(\theta)^T u(\theta) d\theta \right) ds,$$

where $\bar{\tau} = \max(\tau_{ij})$. Taking the time derivative of $V(x, t)$ and using (6.4), (6.2), (6.3), (6.19), (6.23), (6.24), the update law in (6.18), the skew-symmetry property [99] and canceling out the like terms results in

$$\begin{aligned} \dot{V} = & -\alpha_0 e_0^T e_0 - \alpha_1 e_1^T e_1 - r^T b_d k r - S^T \beta S - \frac{1}{\zeta_f} y^T y + S^T (\hat{w} \hat{\mu} + (1 - \hat{w}) u_\tau) + e_0 e_1 \\ & + y^T \eta + r^T \left(\tilde{N} + d + b_d \mu_{loss} + b_d (I - \zeta_{sf}) W c_d + b_d \phi S + b_d \phi y + \tilde{b} \phi \mu \right) \\ & + r^T \left(b_d \tilde{\phi} \bar{\mu} + b_d \phi \tilde{\mu} \right) + \frac{\zeta_f}{\beta^2} \bar{\tau} \|u\|^2 - \frac{\zeta_f}{\beta^2} \int_{t-\bar{\tau}}^t \|u(\theta)\|^2 d\theta. \end{aligned}$$

The previous equation can be bounded using (6.9), (6.20), the definitions of u , and Assumptions 2 and 3 to get

$$\begin{aligned} \dot{V} \leq & -\alpha_0 e_0^T e_0 - \alpha_1 e_1^T e_1 - r^T \left(b_d k - b_d \tilde{\phi} \hat{\phi}^{-1} k \right) r - S^T \beta S - \frac{1}{\zeta_f} y^T y + \|S\| \|\hat{w} \hat{\mu} + (1 - \hat{w}) u_\tau\| \\ & + \|e_0\| \|e_1\| + \|r\| [(\rho_1(\|z\|) + \rho_2(\|z\|)) \|z\| + \epsilon_1 + \epsilon_2] + \|y\| \|\eta\| + \|b_d \phi\| \|r\| \|S\| \\ & + \|b_d \phi\| \|r\| \|y\| + \|r\| \left\| b_d \tilde{\phi} \hat{\phi}^{-1} \zeta_{sf} W \hat{c} \right\| + \|r\| \|b_d \phi \tilde{\mu}\| \\ & + \frac{\zeta_f \bar{\tau}}{\beta^2} (\beta^2 \|S\|^2 + 2\beta \|S\| \|\dot{\mu}_f\| + \|\dot{\mu}_f\|^2) - \frac{\zeta_f}{\beta^2} \int_{t-\bar{\tau}}^t \|u(\theta)\|^2 d\theta. \end{aligned}$$

Using the fact that $u \in [u_{\min}, u_{\max}]$, $\hat{\mu} \in [u_{\min}, u_{\max}]$, and $\hat{\phi} \in [\hat{\phi}_{\min}, 1]$, Young's inequality, and (6.20) to bound the following terms

$$\begin{aligned}
\|e_0\| \|e_1\| &\leq \frac{1}{2} \|e_0\|^2 + \frac{1}{2} \|e_1\|^2, \\
\|b_d \phi\| \|r\| \|S\| &\leq \frac{\zeta}{2} \|r\|^2 + \frac{\zeta}{2} \|S\|^2, \\
\|b_d \phi\| \|r\| \|y\| &\leq \frac{\zeta}{2} \|r\|^2 + \frac{\zeta}{2} \|y\|^2, \\
\|y\| \|\eta\| &\leq \frac{1}{2\varepsilon} \|y\|^2 \|\eta\|^2 + \frac{\varepsilon}{2}, \\
\|S\| \|\hat{w}\hat{\mu} + (1 - \hat{w})u_\tau\| &\leq \Psi \|S\| \leq \frac{1}{2\varepsilon} \Psi^2 \|S\|^2 + \frac{\varepsilon}{2}, \\
\|r\| \left\| b_d \tilde{\phi} \hat{\phi}^{-1} \zeta_{sf} W \hat{c} \right\| &\leq \frac{\varepsilon_3^2}{2\varepsilon} \|r\|^2 + \frac{\varepsilon}{2} \\
\|b_d \phi \tilde{\mu}\| \|r\| &\leq \frac{\zeta^2}{2\varepsilon} \|r\|^2 + \frac{\varepsilon}{2} \\
\frac{2\bar{\tau}}{\beta} \|S\| \|y\| &\leq \frac{\bar{\tau}\zeta_f}{\beta} \|S\|^2 + \frac{\bar{\tau}}{\zeta_f\beta} \|y\|^2
\end{aligned}$$

where $\varepsilon \in \mathbb{R}^+$ is an arbitrary constant, $\Psi = \hat{w} + (1 + \hat{w})u_{\max}$, and ζ is defined in (6.20).

After rearranging the terms this expression becomes

$$\begin{aligned}
\dot{V} &\leq - \left(\alpha_0 - \frac{1}{2} \right) e_0^T e_0 - \left(\alpha_1 - \frac{1}{2} \right) e_1^T e_1 - r^T (b_d k + \zeta - \Lambda) r - S^T \left(\beta - \vartheta - \frac{\tau\zeta_f}{\beta} \right) S \\
&\quad - \left(\frac{\kappa}{\zeta_f} - \frac{\zeta}{2} \right) y^T y + \|r\| [(\rho_1(\|z\|) + \rho_2(\|z\|)) \|z\| + \epsilon_1 + \epsilon_2] + \frac{1}{2\varepsilon} \|y\|^2 \|\eta\|^2 \\
&\quad + 2\varepsilon - \frac{\zeta_f}{\beta^2} \int_{t-\bar{\tau}}^t \|u(\theta)\|^2 d\theta.
\end{aligned}$$

where $\Lambda = b_d \tilde{\phi} \hat{\phi}^{-1} k + \left(2\zeta + \frac{\zeta^2}{2\varepsilon} + \frac{\varepsilon_3^2}{2\varepsilon} \right) I$, $\vartheta = \frac{\zeta}{2} + \frac{\Psi^2}{2\varepsilon} + \zeta_f \bar{\tau}$, and $\kappa = 1 - \bar{\tau}\beta^{-2} - \bar{\tau}\beta^{-1}$. After defining ζ_f such that

$$\frac{1}{\zeta_f} \geq \frac{1}{\kappa} \left[\frac{\zeta}{2} + \frac{\Omega^2}{2\varepsilon} + k_o \right], \tag{6.29}$$

where $k_o \in \mathbb{R}^+$ is a known constant and $\Omega > 0$ is the maximum of η in the defined compact set $\Xi = \{h \in \mathbb{R}^{8n} \mid \|h\| < 2\sigma, h = [e, r, S, y]^T\}$ where $\sigma \in \mathbb{R}^+$ is a known constant, the previous

equation becomes

$$\begin{aligned}\dot{V} \leq & - \left(\alpha_0 - \frac{1}{2} \right) e_0^T e_0 - \left(\alpha_1 - \frac{1}{2} \right) e_1^T e_1 - r^T (b_d k + \zeta - \Lambda) r - S^T \left(\beta - \vartheta - \frac{\bar{\tau} \zeta_f}{\beta} \right) S \\ & - k_o y^T y + \|r\| [(\rho_1(\|z\|) + \rho_2(\|z\|)) \|z\| + \epsilon_1 + \epsilon_2] \\ & - \left(1 - \frac{\|\eta\|^2}{\Omega^2} \right) \frac{\|y\|^2 \Omega^2}{2\varepsilon} + 2\varepsilon - \frac{\zeta_f}{\beta^2} \int_{t-\bar{\tau}}^t \|u(\theta)\|^2 d\theta.\end{aligned}$$

Using nonlinear damping to separate the terms and further bounding results in

$$\begin{aligned}\dot{V} \leq & - \left(\alpha_0 - \frac{1}{2} \right) e_0^T e_0 - \left(\alpha_1 - \frac{1}{2} \right) e_1^T e_1 - r^T (b_d k - \Lambda) r - S^T \left(\beta - \vartheta - \frac{\bar{\tau} \zeta_f}{\beta} \right) S \\ & - k_o y^T y + \frac{(\rho_1(\|z\|) + \rho_2(\|z\|))^2 \|z\|^2}{2\zeta} + \frac{(\epsilon_1 + \epsilon_2)^2}{2\zeta} + 2\varepsilon - \frac{\zeta_f}{\beta^2} \int_{t-\bar{\tau}}^t \|u(\theta)\|^2 d\theta.\end{aligned}$$

Further, by splitting the integral term and using the Cauchy Schwarz inequality

$$\|e_I\|^2 \leq \bar{\tau} \int_{t-\bar{\tau}}^t \|u(\theta)\|^2 d\theta$$

the following term can be bounded as

$$-\frac{\zeta_f}{2\bar{\tau}\beta^2} \left(\bar{\tau} \int_{t-\bar{\tau}}^t \|u(\theta)\|^2 d\theta \right) \leq -\frac{\zeta_f}{2\bar{\tau}\beta^2} \|e_I\|^2.$$

This expression can be bounded as

$$\begin{aligned}\dot{V} \leq & - \left(K_{min} - \frac{(\rho_1(\|z\|) + \rho_2(\|z\|))^2}{2\zeta} \right) \|z\|^2 - S^T \left(\beta - \vartheta - \frac{\bar{\tau} \zeta_f}{\beta} \right) S \\ & - k_o y^T y + \frac{(\epsilon_1 + \epsilon_2)^2}{2\zeta} + 2\varepsilon - \frac{\zeta_f}{2\beta^2} \int_{t-\bar{\tau}}^t \|u(\theta)\|^2 d\theta,\end{aligned}\tag{6.30}$$

where K_{min} is defined as $K_{min} = \min \left\{ \alpha_0 - \frac{1}{2}, \alpha_1 - \frac{1}{2}, \gamma_{min} \{b_d k - \Lambda\}, \frac{\zeta_f}{2\bar{\tau}\beta^2} \right\}$. Because

$$\begin{aligned}\int_{t-\bar{\tau}}^t \left(\int_s^t \|u(\theta)\|^2 d\theta \right) ds & \leq \bar{\tau} \sup_{s \in [t, t-\bar{\tau}]} \left[\int_s^t \|u(\theta)\|^2 d\theta \right] \\ & = \bar{\tau} \int_{t-\bar{\tau}}^t \|u(\theta)\|^2 d\theta,\end{aligned}$$

(6.30) can be rewritten as

$$\begin{aligned} \dot{V} \leq & - \left(K_{min} - \frac{(\rho_1(\|z\|) + \rho_2(\|z\|))^2}{2\zeta} \right) \|z\|^2 - S^T \left(\beta - \vartheta - \frac{\bar{\tau}\zeta_f}{\beta} \right) S \\ & - k_o y^T y + \frac{(\epsilon_1 + \epsilon_2)^2}{2\zeta} + 2\varepsilon - \frac{1}{2\bar{\tau}} P, \end{aligned} \quad (6.31)$$

Using the definitions of $x(t)$ and $z(t)$ this expression can be upper bounded as

$$\dot{V} \leq - \bar{K}_{min} \|x\|^2 - \left(K_{min} - \frac{(\rho_1(\|z\|) + \rho_2(\|z\|))^2}{2\zeta} \right) \|e_I\|^2 + \frac{(\epsilon_1 + \epsilon_2)^2}{2\gamma} + 2\varepsilon, \quad (6.32)$$

where \bar{K}_{min} is defined as

$$\bar{K}_{min} = \min \left\{ K_{min} - \frac{(\rho_1(\|z\|) + \rho_2(\|z\|))^2}{2\zeta}, \beta - \vartheta - \frac{\bar{\tau}\zeta_f}{\beta}, k_o, \frac{1}{2\bar{\tau}} \right\}.$$

This expression can be further bounded if $K_{min} - \frac{(\rho_1(\|z\|) + \rho_2(\|z\|))^2}{2\zeta} > 0$, which is true if the condition $\|z\|^2 < \bar{\rho}^{-2}(\sqrt{2\bar{K}_{min}\zeta})$ is satisfied, where $\bar{\rho}$ is a positive monotonically increasing bounded function defined as $\bar{\rho} = \rho_1(\|z\|) + \rho_2(\|z\|)$. Considering (6.28), the definitions of x and z , and $P > \frac{\zeta_f}{\bar{\tau}\beta^2} e_I^2$, a set \mathbb{S} can be defined as

$$\mathbb{S} \triangleq \left\{ x(t) \in \mathbb{R}^{9n+1} \mid \|x(0)\| < \sqrt{\frac{\lambda_1}{\lambda_2} \left(\min \left\{ 1, \frac{\zeta_f}{\bar{\tau}\beta^2} \right\} \bar{\rho}^{-2} \left(\sqrt{2\zeta K_{min}} \right) - \frac{\Upsilon}{\lambda_1} \right) - \frac{B\lambda_2}{\delta\lambda_1}} \right\},$$

where $B \in \mathbb{R}^+$ is a subsequently defined constant. In \mathbb{S} , $\bar{K}_{min}(\|z\|)$ is bounded by a constant $\delta \in \mathbb{R}^+$ as

$$\bar{K}_{min}(\|z\|) \geq \delta.$$

Adding and subtracting $\frac{\delta}{\lambda_2} \Upsilon$ to (6.32) and using (6.28), (6.32) becomes

$$\dot{V} \leq -\frac{\delta}{\lambda_2} V + B, \quad (6.33)$$

where $B = \frac{\delta}{\lambda_2} \Upsilon + \frac{(\epsilon_1 + \epsilon_2)^2}{2\zeta} + 2\varepsilon$. (6.33) can be integrated with respect to time to obtain

$$V(x, t) \leq V(0)e^{-\frac{\delta}{\lambda_2}t} + \frac{B\lambda_2}{\delta} \left(1 - e^{-\frac{\delta}{\lambda_2}t} \right). \quad (6.34)$$

Based on (6.34) and (6.28), the condition in Theorem 1, (6.26), can be restated as

$$\|x(t)\| \leq \sqrt{\frac{\lambda_2}{\lambda_1} \left(\|x(0)\|^2 - \frac{B}{\delta} \right)} e^{-\frac{\delta}{2\lambda_2}t} + \sqrt{\frac{\lambda_2 B}{\lambda_1 \delta}}. \quad (6.35)$$

Using this expression, the definition of $x(t)$, and (6.2), an explicit bound on the tracking error $e(t)$ can be derived as

$$\|e(t)\| \leq (1 + \alpha_0) \left(\sqrt{\frac{\lambda_2}{\lambda_1} \left(\|y(0)\|^2 - \frac{B}{\delta} \right)} e^{-\frac{\delta}{2\lambda_2}t} + \sqrt{\frac{\lambda_2 B}{\lambda_1 \delta}} \right). \quad (6.36)$$

□

6.4 SIMULATIONS

The efficacy of the newly developed controller was tested in a simulation study on a 2-DOF fixed hip model of a leg. Note that these simulations were conducted on a previous version of the controller which did not include integral control. The fixed hip model represents the movement of the lower extremities while the hip is fixed. In this model, only the hip and knee joints are actuated (i.e., the ankle joint is fixed) and only motion in the saggital plane is considered. This model considers actuation of the antagonistic muscle pairs via FES and an electric motor at each joint, i.e., 6 overall inputs for a 2-DOF system. The musculoskeletal model and parameters used in the simulations were taken from [78] for a person with SCI. Optimizations were conducted to compute the optimal inputs that track normal gait data taken from [119] for one complete gait cycle. For the optimizations, the convex cost function's objective was to minimize the position and velocity error, and minimize the activations of the system and is defined as

$$\min_u \Pi = \int_{t_0}^{t_f} (e(t)^T Q_1 e(t) + \dot{e}(t)^T Q_2 \dot{e}(t) + \mu(t)^T R \mu(t)) dt \quad (6.37)$$

$$\text{subject to: } M(q)\ddot{q} + C(q, \dot{q})\dot{q} + G(q) + f(q, \dot{q}) = b(q, \dot{q})\mu$$

$$\mu \in [\mu_l, \mu_u]$$

where $Q_1 \in \mathbb{R}^{2 \times 2}$ is a weight on the position tracking error, $Q_2 \in \mathbb{R}^{2 \times 2}$ is the weight on the velocity tracking error, the matrix $R \in \mathbb{R}^{6 \times 6}$ is a positive-definite matrix of weights on the activation vector, and the lower and upper bound on the activations are defined as μ_l and $\mu_u \in \mathbb{R}^6$. The optimal activations computed through the optimization to reproduce the gait data can be seen in Fig. 6.2. For more details on the dynamic optimization used to compute optimal activations, see [92].

The synergies, W , and their activation, c_d , were then extracted from the optimal activations using PCA. The synergies that account for little variance in the reconstructed activation data were truncated to decrease the dimensionality of the feedforward component. For this simulation study, the dimensions were reduced from 6 to 3 variables while still accounting for about 94% of the variance as can be seen in Fig. 6.3. The reduced 3 synergies and their activations are shown in Fig. 6.4.

After the synergies were extracted from the optimal activations and reduced dimensionally, the controller in (6.25) was simulated for 5 minutes to demonstrate the effect of the fatigue estimate on the controller. The fatigue and activation dynamics are modeled as a first order differential equations [84, 94]. To illustrate the effect of the fatigue, the plots in Fig. 6.5-6.8 depict the simulation results for the first 5 seconds, where there is little fatigue, and for the last five seconds, where the muscles are more fatigued. The tracking performance of the controller can be seen in Fig. 6.5. The root mean squared errors for the hip and knee joints were found to be 2.91° and 2.82° , respectively.

This controller is comprised of multiple components that play an important role in the overall control system which can be seen in the control results. The effects of the adaptive synergy-based feedforward component, $\hat{\phi}^{-1} \zeta_{sf} W \hat{c}$, in $\bar{\mu}$ can be seen in Fig. 6.6. The effect of the fatigue estimate becomes apparent when comparing the normalized muscle activations from the first and last five seconds of the results. By design, the fatigue estimate does not affect the normalized motor currents as motors do not fatigue. However, from Fig. 6.6, a slight increase in amplitude (motor) is still apparent. This is due to the adaptation of the synergy activation coefficients. The feedback component, kr , in $\bar{\mu}$ was only applied to the motors and is shown in Fig. 6.7. After applying the DSC structure, the actual input signals can be seen in Fig. 6.8. The estimate of the fatigue can be seen in Fig. 6.9 where it can

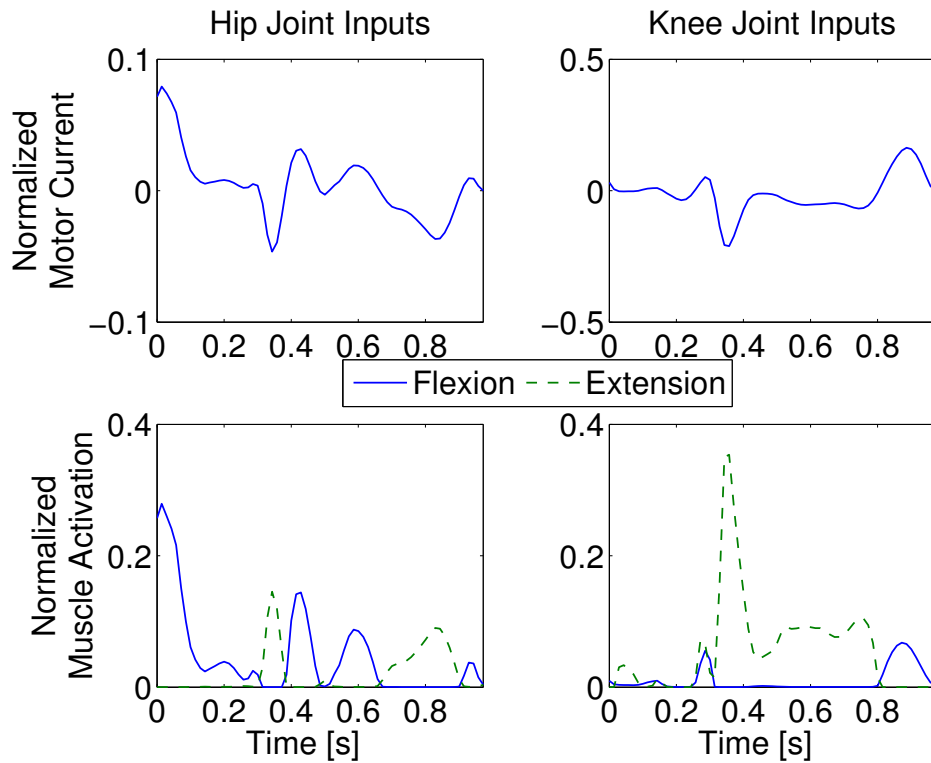


Figure 6.2: Optimal activations generated from dynamic optimizations. The peak in the hip flexion and knee extension are intentionally computed by the dynamic optimizations to counteract the passive torques near hyper flexion and hyper extension.

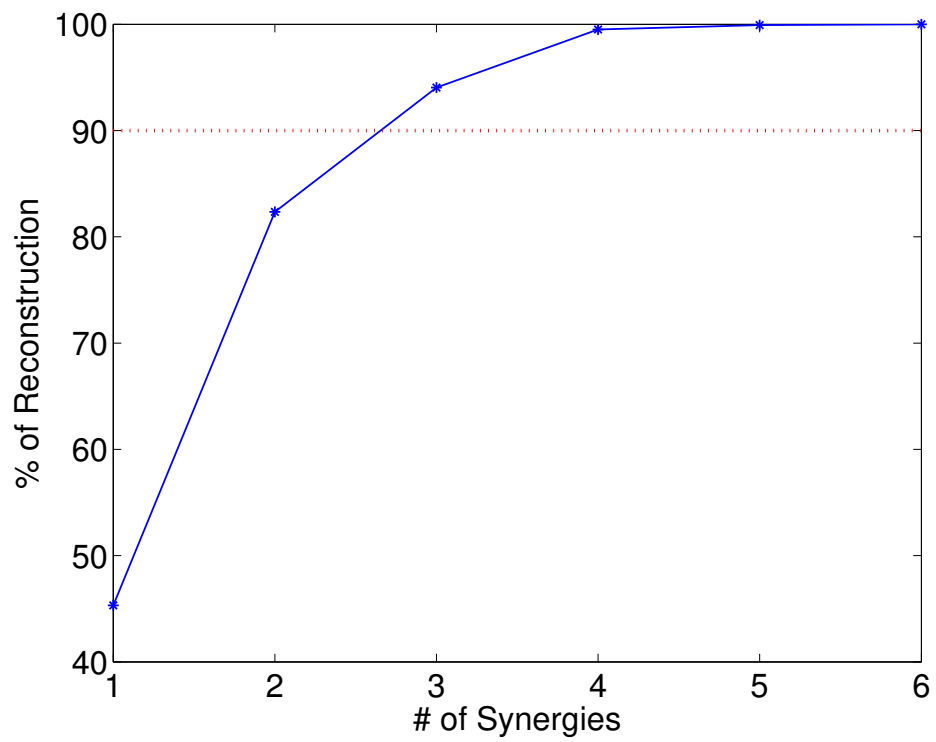


Figure 6.3: Number of synergies vs. Reconstruction variance

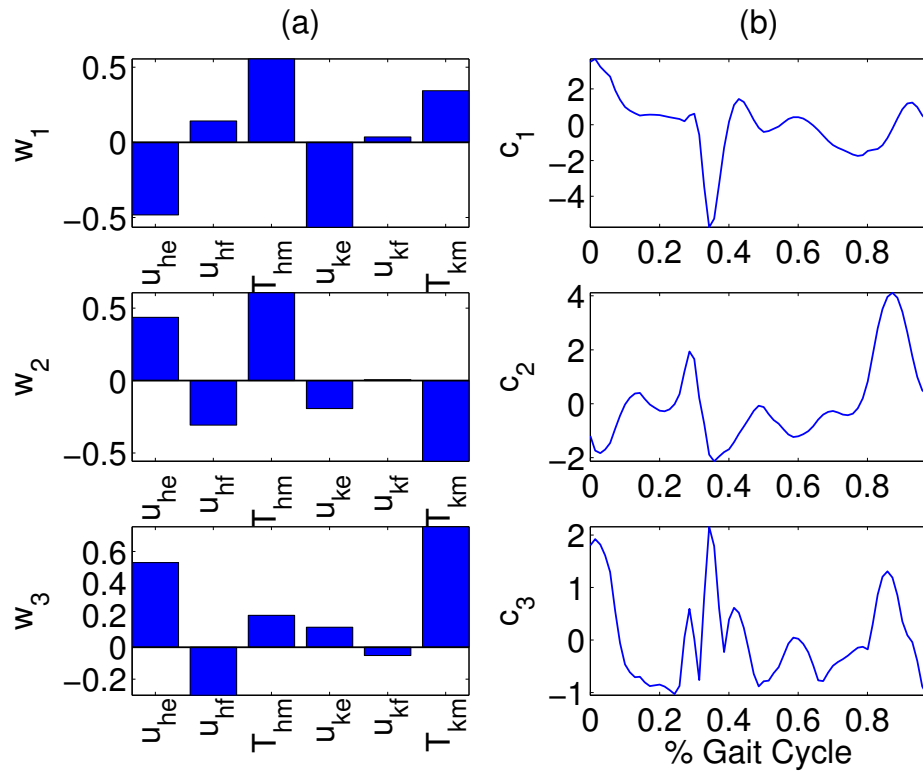


Figure 6.4: (a) Three synergies: w_1 , w_2 , and w_3 after dimension reduction. (b) The corresponding time-varying synergy activation c_1 , c_2 , c_3 , of the three synergies.

be seen that the knee extensors and hip flexors fatigued the most, which means that their input is scaled the most due to the $\hat{\phi}^{-1}$ term; this is evident in Fig. 6.6 & 6.8.

6.5 EXPERIMENTAL PROTOCOL

Experiments were conducted on a single leg of an able bodied subject (Male; Age: 24 years), on two testbeds which can be seen in Fig. 6.10. Prior to any experimentation, an approval from the Institutional Review Board at the University of Pittsburgh was obtained. The participant was instructed to relax and avoid any voluntary interference during the electrical stimulation. The real-time implementation of the controller requires subject specific parameters for the state estimators. These parameters and the minimum/maximum stimulation levels for each muscle were empirically identified through system identification experiments. These experiments were conducted on a leg extension machine (LEM) modified to hold the subjects leg in an isometric configuration and instrumented with a load cell (Omega, USA) to measure the torque generated through FES elicited contractions.

The system identification process consisted of three sets of experiments for each muscle. During these experiments the subject is seated in the LEM with their shank strapped to the load cell in an isometric configuration (position is constant). In the first experiment, the muscle is stimulated with a stimulation ramp while the torque produced is measured. The purpose of this experiment was to determine the v_{\max} and v_{\min} parameters in (6.25). In the second set, the muscles are stimulated at v_{\max} for a few seconds to elicit a step response. From the normalized torque data, the EMD and time constant for the first order activation dynamics were determined. This same procedure was used to determine the activation time constant for the motor which was mounted on the LEM. In the final set of experiments, the subject was stimulated at v_{\max} for two minutes to fatigue the muscles followed by one second pulses every ten seconds to capture the recovery rate of the muscles. From the normalized torque measurements, the fatigue and recovery rates for each muscle can be determined from the two data sets. These parameters are then used in the estimators in (6.12) and (6.13) during real-time implementation of the controller. Table 6.1 shows the identified parameters.

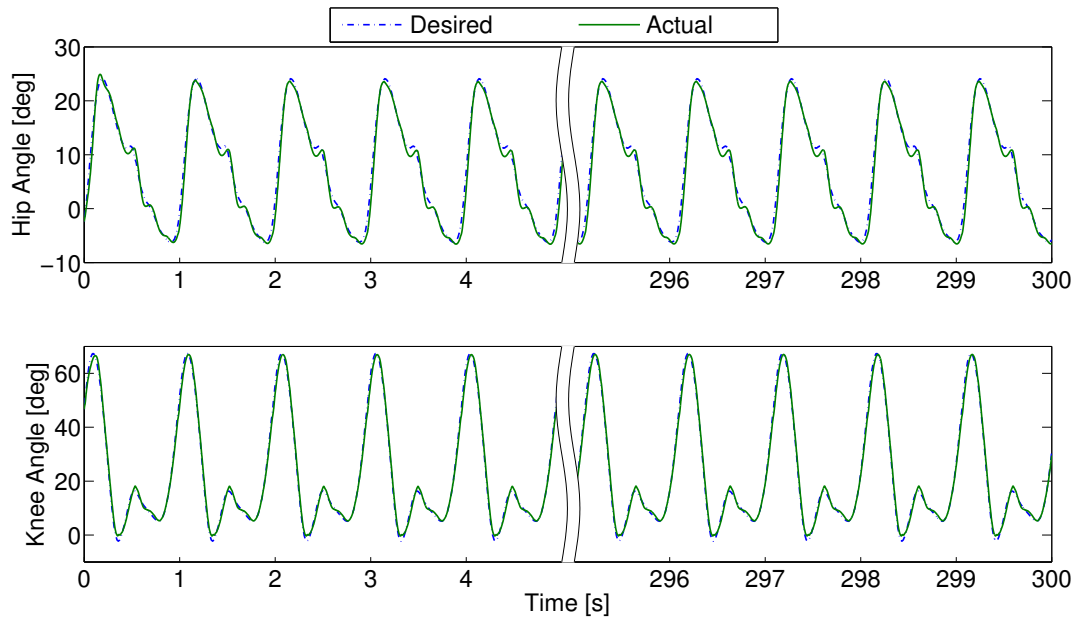


Figure 6.5: The control performance of the joint angles resulting from simulating the newly developed controller. Top plots the desired and actual hip joint angle. Bottom plots the desired and actual knee joint angle, each for the first and last five seconds of the 5 min. simulation.

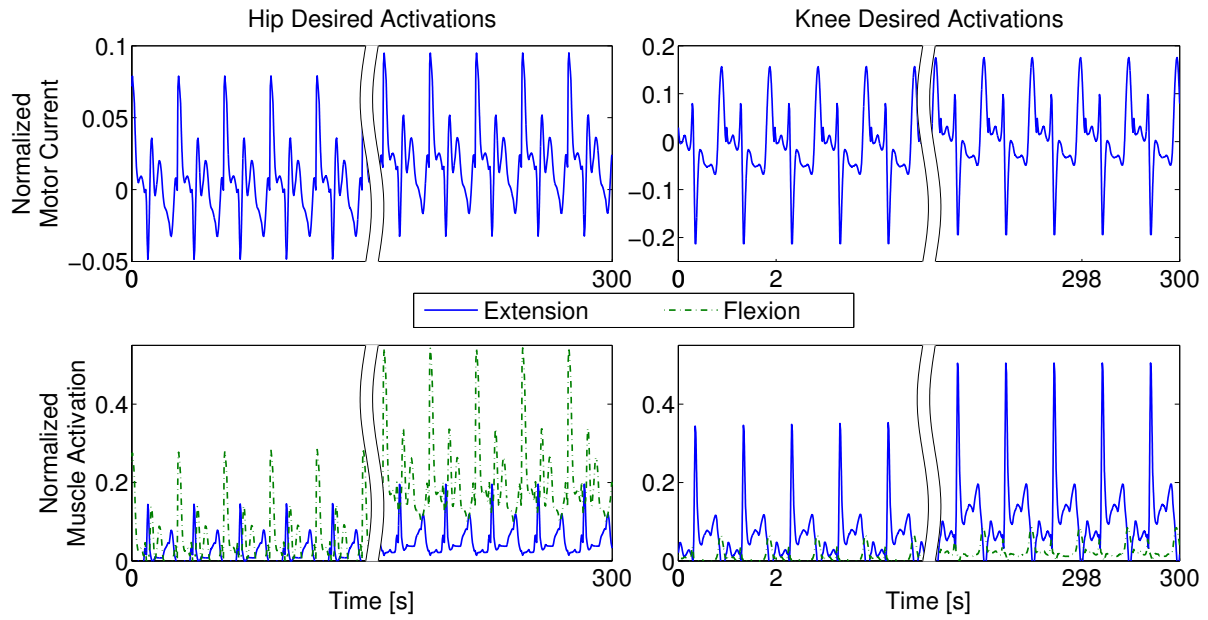


Figure 6.6: Feedforward component, $\hat{\phi}^{-1}\zeta_{sf}W\hat{c}$ in $\bar{\mu}$, reconstructed through the reduced synergies after adaptation and with the scaling up from the fatigue estimates. The first and last 5 seconds of the signals are shown to illustrate the increases in the signal amplitude as the muscles fatigue.

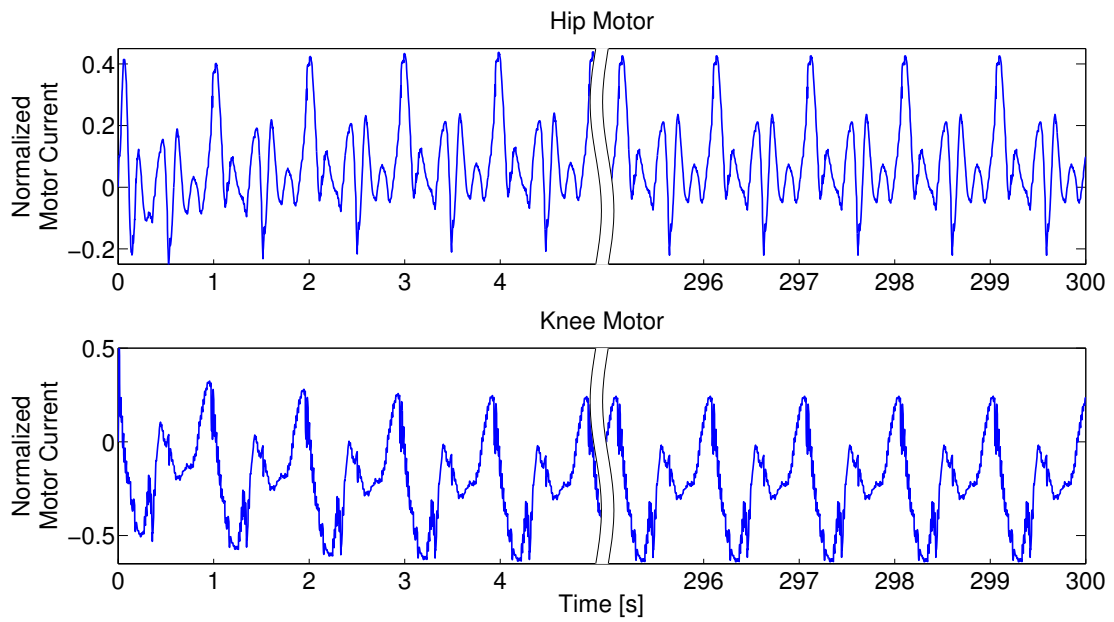


Figure 6.7: The first and last 5 seconds of the feedback component, kr in $\bar{\mu}$, which was only applied to the two motors.

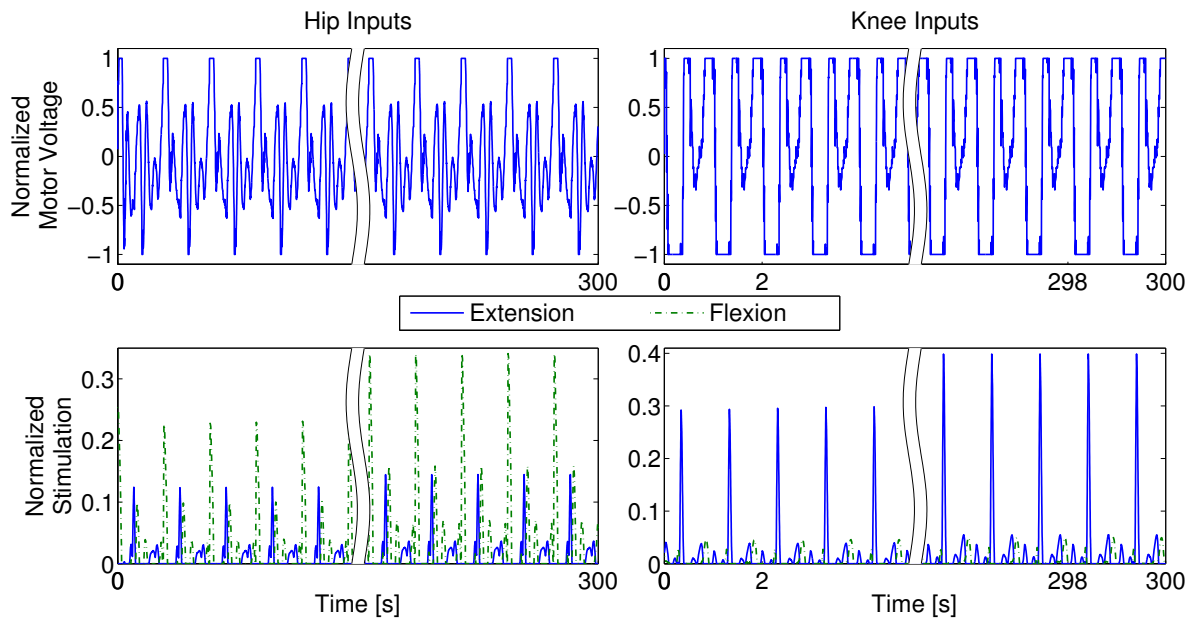


Figure 6.8: The normalized inputs to the system, u . The first and last 5 seconds are shown for the stimulation inputs to show the effect of the scaling due to the fatigue estimate.

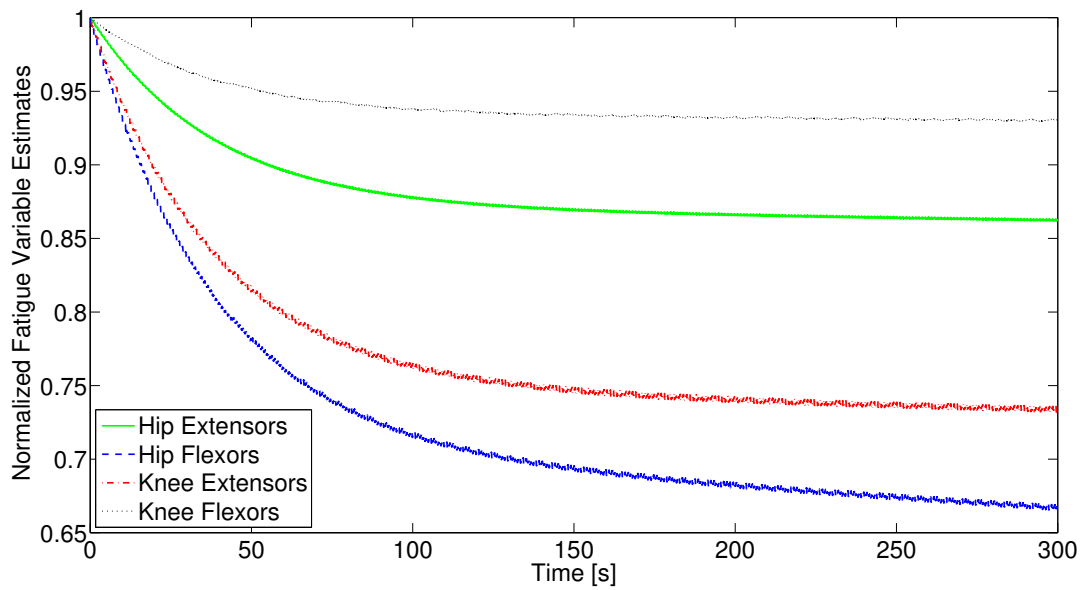


Figure 6.9: The normalized fatigue variable for the four muscles, hip and knee flexors/extensors, over the 5 minute trial. The fatigue variable ranges from zero to one, which correspond to full fatigue and no fatigue, respectively.

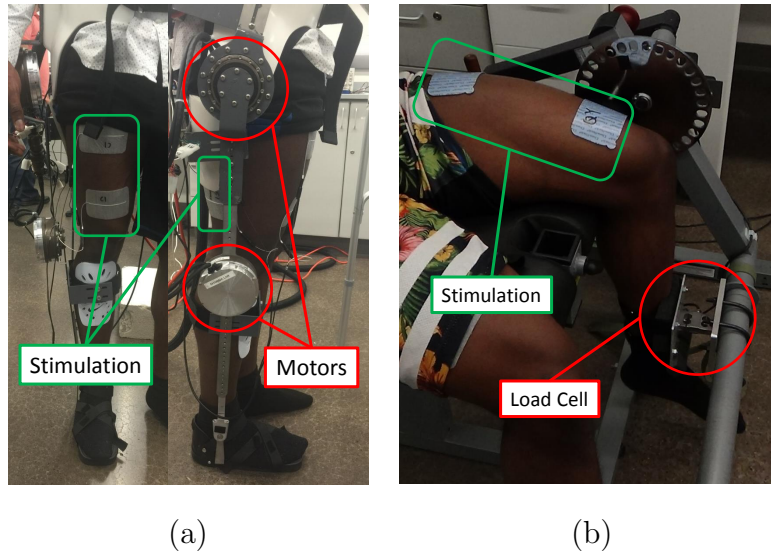


Figure 6.10: The testbeds used to conduct the experiments: (a) a hybrid exoskeleton with electric motors at the hip and knee joint and stimulation of quadriceps and hamstrings was used to implement the new controller and (b) a modified leg extension machine with a load cell to measure force was used to perform system identification experiments.

Table 6.1: The subject specific parameters and motor parameters extracted in the system identification experiments. Notice that the motors do not have any fatigue parameters or input delays.

Parameter	Quadriceps	Hamstring	Motor
v_{\min}	15 mA	20 mA	-10 volts
v_{\max}	45 mA	50 mA	10 volts
\hat{w}	.085	.096	.062
τ	111 ms	130 ms	-
\hat{T}_r	29.02 s	33.24 s	-
\hat{T}_f	33.01 s	45.62 s	-
$\hat{\phi}_{\min}$	0.051	0.404	-

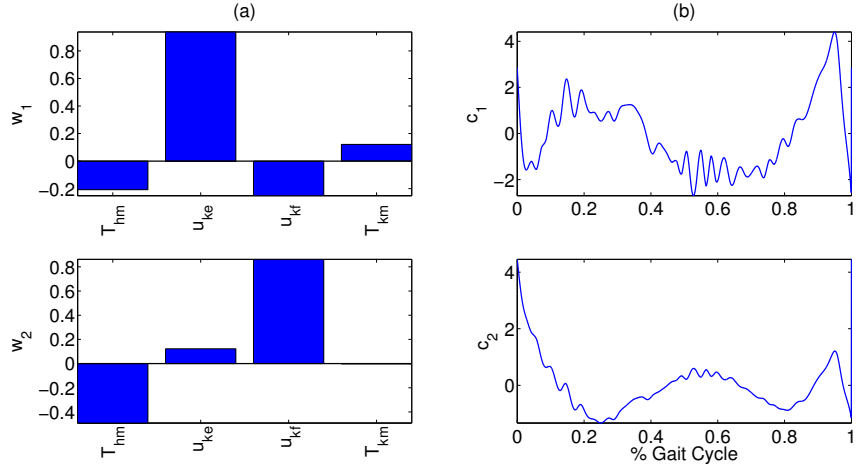


Figure 6.11: The synergies used in the preliminary experiments: (a) Two synergies: w_1 and w_2 after dimension reduction. (b) The corresponding time-varying synergy activation profiles c_1 and c_2 .

Before the controller can be implemented, the optimal activations and synergies must be computed offline. For the dynamics optimizations, parameters for the passive dynamics and torque-length/torque-velocity relationships were taken from data reported for healthy subjects in [78]. Any mismatch or model error this would cause is considered as additional disturbances in the system and in u_{loss} . The cost function expressed in (6.37) was modified for a 2-DOF system with 4 inputs, thus the parameters are redefined as $R \in \mathbb{R}^{4 \times 4}$ and μ_l , and $\mu_u \in \mathbb{R}^4$. The swing phase gait trajectories from [119] were used, except that the trajectories were slowed down to 4s step cycle instead of a 1s step cycle. This was done because the electric motors of the exoskeleton are not able to generate the joint torque required at faster speeds. The amount of signals needed in the feedforward component were reduced by 50% by using 2 synergies. These 2 synergies and their desired activation profiles can be seen in Fig. 6.11.

The newly developed controller was then tested on a hybrid exoskeleton consisting of electric motors and FES of multiple muscles. Note that these experiments were conducted on a previous version of the controller which did not include integral control. The electric

motors (Harmonic Drive LLC, MA, USA) were located at the hip joint and knee joint and can produce a maximum torque of 40 Nm. Although the simulations consider stimulation of the flexors and extensors at both joints, the use of transcutaneous electrical stimulation to produce hip movements is not feasible as the muscles are located deep and can be difficult to stimulate through surface electrodes. Therefore only stimulation of the knee joint flexors and extensors was used in the experimental trials. A RehaStim 8-channel stimulator (Hasomed Inc., DE) was used to generate the current modulated biphasic pulse trains transmitted to the transcutaneous electrodes at 35 Hz. The QPIDE (Quanser Inc, Ontario Canada) DAQ board was used to interface with the motor drivers and run the controller in real-time at 1 kHz. The system identification and control algorithms were coded in Simulink (MathWorks Inc, USA) and implemented using the Quarc real-time software (Quanser Inc, Ontario Canada). The full controller was tested in a 20s long trial. These experiments were conducted on another day after the first set of experiments to allow the subjects muscle to fully recover from the fatigue trials in the system identification experiments.

6.6 EXPERIMENTAL RESULTS

The tracking performance from the experimental trial can be seen in Fig. 6.12. The root mean squared errors for the hip and knee joints were found to be 0.31° and 0.18° , respectively. The feedforward component, $\hat{\phi}^{-1}\zeta_{sf}W\hat{c}$, and feedback component, kr , in $\bar{\mu}$ can be seen in Figs. 6.13 & 6.14. As seen in Fig. 6.17 the effect of the fatigue estimate is not as apparent in the experiments. This is because the fatigue parameters identified for the subject were very slow resulting in the muscles barely fatiguing. However, for SCI subjects muscle fatigue occurs more rapidly, hence this is still a practical feature in the controller. Another important aspect of the controller is the βS term in (6.22), which includes the delay compensation term and serves to minimize the error between the desired activation and the activation estimate. Therefore, the DSC structure determines the control input which minimizes this error, as seen in Fig. 6.15. After applying the DSC structure, the actual input signals can be seen in Fig. 6.16.

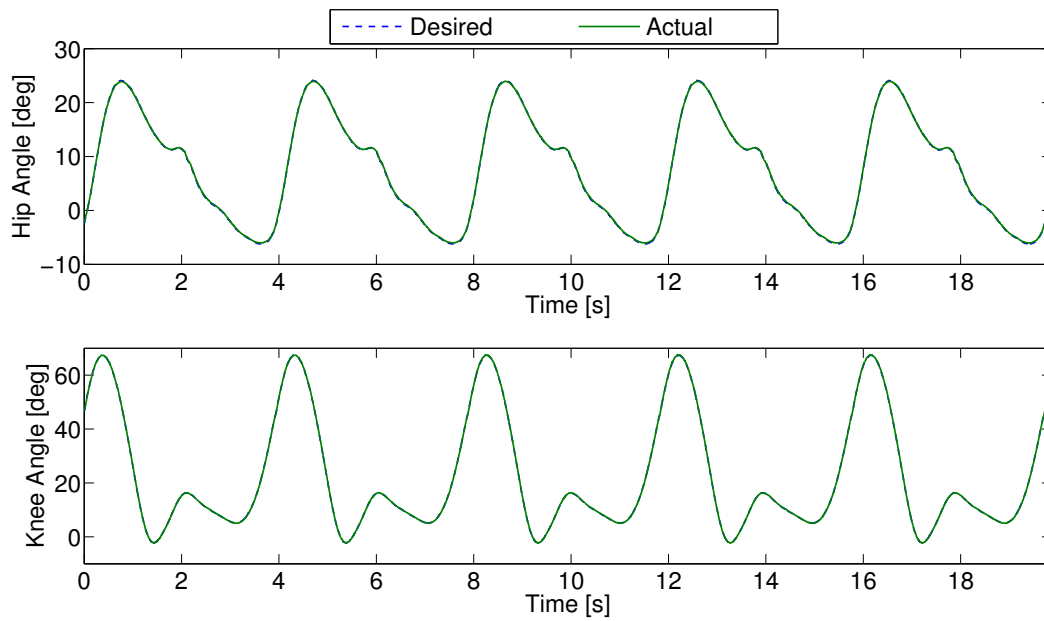


Figure 6.12: The joint angles resulting from the newly developed controller in experiments. Top plots the desired and actual hip joint angle. Bottom plots the desired and actual knee joint angle, each for five cycles.

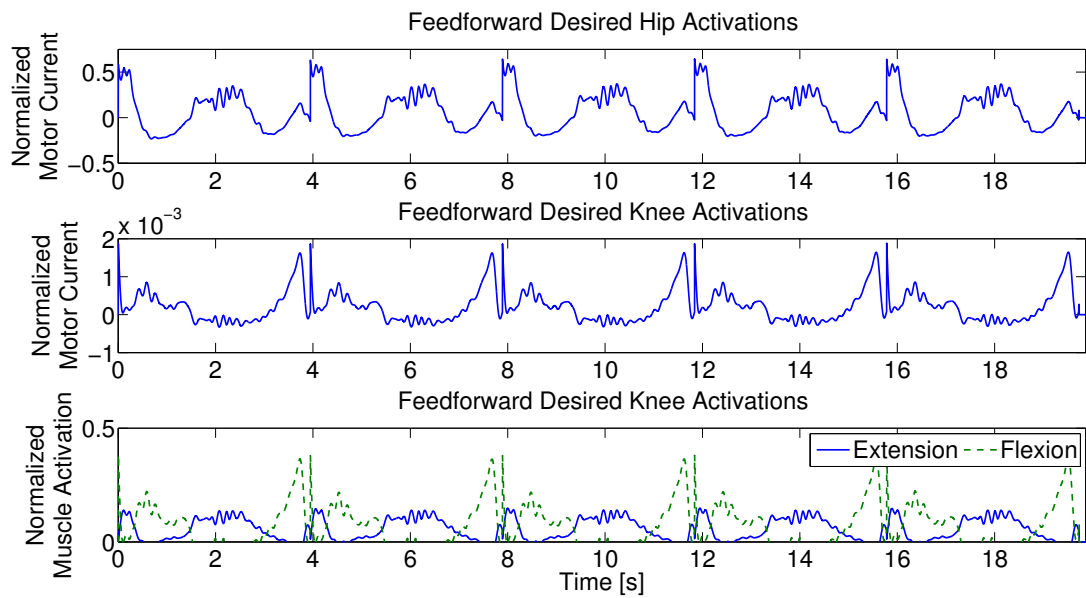


Figure 6.13: The feedforward component of $\bar{\mu}$ which is reconstructed through the synergies after adaptation and with the scaling up from the fatigue estimate.

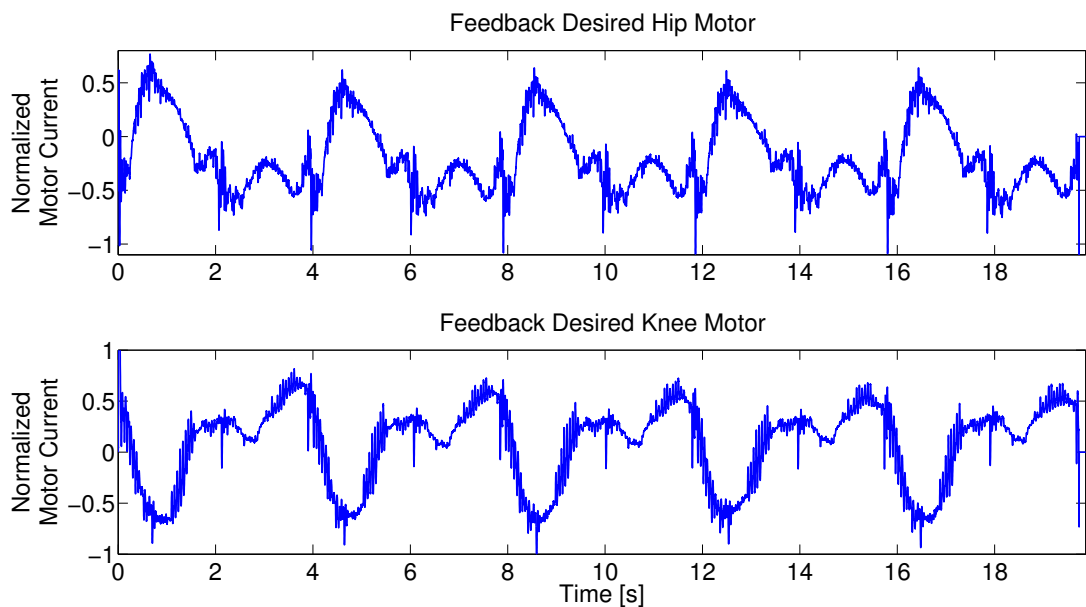


Figure 6.14: The feedback component of $\bar{\mu}$, which were only applied to the motors.

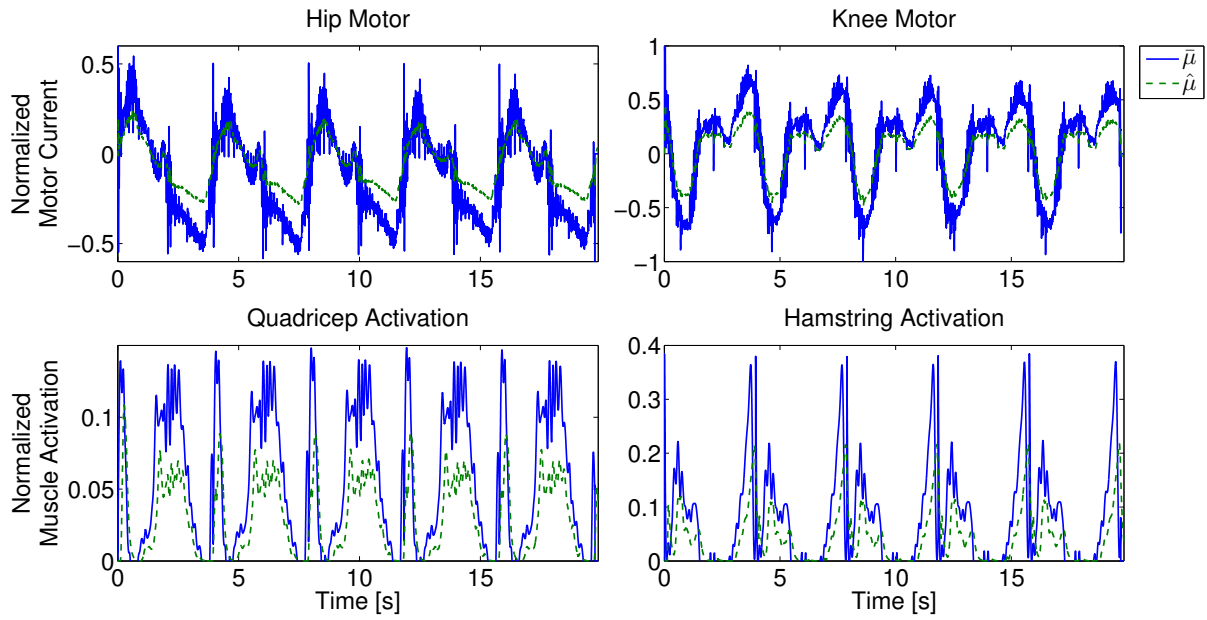


Figure 6.15: A comparison between the desired activation $\bar{\mu}$ and the estimated activation $\hat{\mu}$.

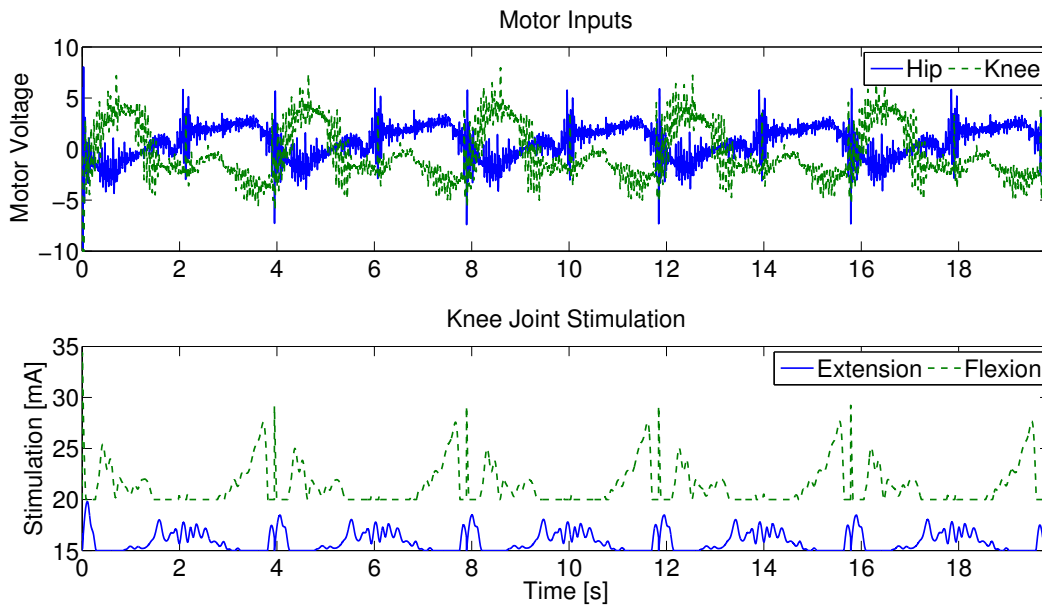


Figure 6.16: The inputs for the motors and stimulation during the experiments. Note that the stimulation levels start at the minimum value which differs for each muscle.

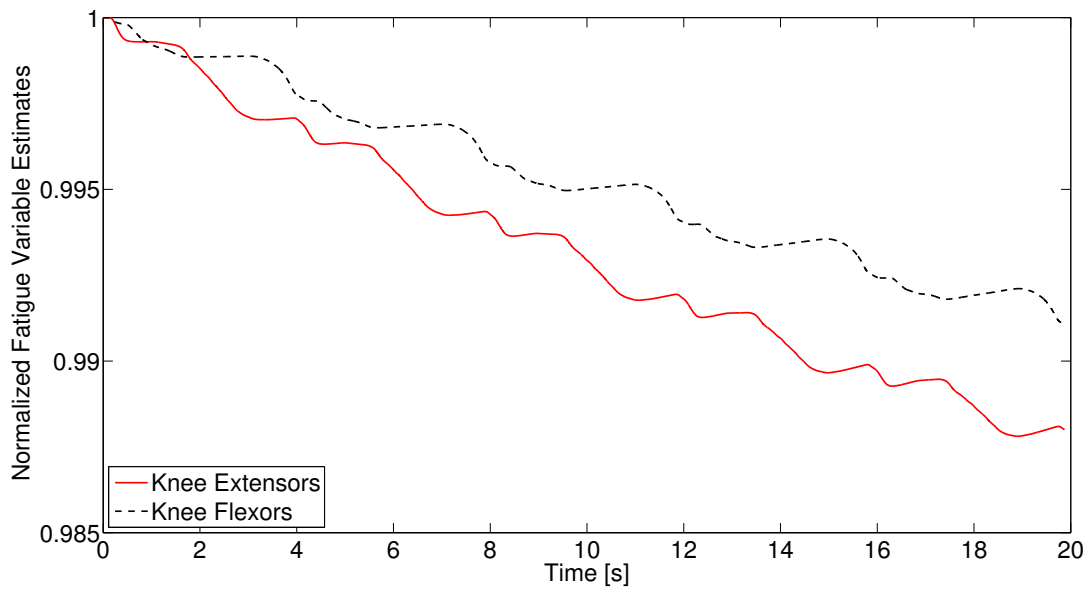


Figure 6.17: The normalized fatigue variable estimate for the knee flexors and extensors. The fatigue variable ranges from zero to one, which correspond to full fatigue and no fatigue, respectively.

6.7 DISCUSSION

Hybrid exoskeletons that combine electric motors and FES may have a potential to induce greater walking durations than the systems that strictly use electric motors or FES; in addition to providing a light weight walking restoration technology. However, the cooperative use of electric motor and FES in such hybrid devices results in an actuator redundancy. In this chapter an adaptive synergy-based dynamic surface controller that can compensate for actuator dynamics, muscle fatigue dynamics, and input delays was developed and demonstrated through simulations and experiments. The controller solves the control allocation problem by using optimized feedforward components which are dimensionally reduced through synergies. The optimized feedforward signals were computed from control signals resulting from a dynamic optimization that determined how to allocate control between the electric motors and FES. Feedback control to only the motors was included to improve robustness and performance. The newly developed controller was validated through simulations on a fixed hip model of the leg, and through experiments on an able-bodied person in a hybrid exoskeleton device.

The control approach proposed in this chapter follows a systematic control design approach for hybrid walking exoskeletons. The approach is inspired from the muscle synergy principle. The studies proposing muscle synergy as a basis of human motor control employ an approach of recording EMG signals (collected from multiple muscles) and then decompose these signals to muscle synergies (lower dimensions). Unlike these studies, our focus is on the design of synergies for stimulating multiple muscles and actuating electric motors in a hybrid exoskeleton. For the latter design approach, using optimized control signals offers multiple advantages and convenience. The optimization framework allows to incorporate external inputs to the exoskeleton and artificial stimulation inputs for FES at the same time. The traditional synergy studies investigate natural modes of muscle recruitment, not electric motor inputs as with a powered exoskeleton. Therefore, the muscle synergies extracted from EMG recordings cannot be mapped easily, and also optimally, to design artificial inputs for FES and electrical motors (extra redundancy). In addition, the optimization framework can be used to design or plan a new joint angle trajectory that can be specific to a subject

with a neurological impairment. The traditional synergy will not allow this as some of these subjects may not have voluntary movements, especially for persons with complete SCI (i.e., no EMG recordings). In our previous work [92], we have pointed out that the dynamic optimizations can be used to design subject-specific optimal control inputs for a hybrid orthosis. These optimal control inputs, which are redundant, can be then transformed to a lower dimensional control by using methodology inspired from the traditional muscle synergy extraction approach.

Optimizations are used to compute the optimal activations to ensure that the redundant actuators are not counteracting each other, i.e. the motors and FES should not be working against each other. The relative amount of stimulation and motor effort can be adjusted through two aspects of the control scheme: 1) via the cost function of the optimization or 2) via the scaling gain in the feedforward loop in (6.17). The optimal stimulation activation profiles, used in the feedforward component of the controller, are computed based on the model and are limited by modeling errors and parameter mismatch. We used majority of the model parameters from [78] to compute the synergy-based feedforward component during the experimental validation on the able-bodied subject. This parameter mismatch may have decreased the effectiveness or contribution of the feedforward component. However, it did not affect the control performance, which depicts the robustness of the overall control scheme. We also suspect that the feedforward stimulation inputs from the controller may not generate enough torque to overcome the impedance due to electric motors. The current work ignored the impedance in the motors during the optimizations. We will address these limitations and the following limitations in our future work.

The new controller can be implemented on any type of trajectory, therefore simpler trajectories can be used in accordance with this controller. We opted to use trajectories from normal gait studies [119]. One can use the feedforward controller for a simple set of trajectories and the feedback controller to reject any disturbances that may result during gait; e.g., upper body forces during walking. However, the current study was focused on the control design for only the swing phase. In our future work, numerous improvements will be made to extend the controller to full gait cycle. These modifications include adding impedance control and accounting for upper-body effort. The preliminary experimental

results that validated the new controller on an able-bodied subject are promising; however, the clinical efficacy of the control design remains to be seen. Our future efforts includes verifying the controller on a person with complete SCI and developing control methods that incorporate voluntary effort; e.g. extending the control designs to persons with stroke and incomplete SCI.

Precise measurement or accurate estimate of fatigue and activation dynamics is still an open research problem. EMG based fatigue estimators are not feasible, especially when the EMG signals are masked by artifacts due to surface stimulation. The use of force sensors to estimate fatigue would also prove challenging as there are multiple interaction forces which would alter the signals and have to be used in an isometric configuration to measure fatigue. As an alternative, the control development and stability analysis uses model based estimates of the activation and fatigue as opposed to an assumption that they are measurable. These estimates are computed on-line using a model based estimators that use the equations presented in the dynamic model section. In addition, the controller has been implemented experimentally in real-time on an able bodied subject. System identification experiments were conducted to determine the parameters needed for the estimators. Nonetheless, the control development provides a systematic way to integrate fatigue measurements or fatigue estimates in the control design. The controller, or the control development can be easily replaced with an accurate model of fatigue or a measurable fatigue signal, if real-time measurements of fatigue or improved mathematical descriptions of FES-induced muscle fatigue become feasible in the future.

6.8 CONCLUSION

In this chapter, an adaptive synergy-based low dimensional controller is presented for a lower-limb hybrid neuroprosthesis comprising of an FES system and a powered exoskeleton. The new controller, which was inspired from the muscle synergy principle, was designed to account for redundant actuation structure. Further, the control design also accounted for activation and fatigue dynamics and EMD due to FES. Model based estimators were used to

estimate the actuator activation and the fatigue signals. A Lyapunov-based stability analysis of the new controller yielded UUB tracking, despite unmodeled disturbances. The efficacy of the controller was tested in simulations and an experiment. The experiment was conducted on an able-bodied subject to track a swing-phase gait trajectory. The controller showed ability to coordinate FES of the quadriceps and hamstrings muscles and electric motors at the hip joint and knee joint of the exoskeleton. The controller also showed robustness to modeling errors. Future research efforts will be to extend the developed controller to a full gait cycle control and verifying the control design on a person with neurological impairment.

7.0 EXPERIMENTAL DEMONSTRATION OF THE SYNERGY-BASED PID-DSC CONTROLLER IN A WALKING HYBRID NEUROPROSTHESIS

7.1 INTRODUCTION

In the previous chapter, the overall control system that addressed the 4 challenges was derived and tested through simulations and experiments on an able bodied subject in the fixed hip configuration. Although the tracking performance was acceptable, the effectiveness of the feedforward component of the controller was questionable. Based on the human subjects verbal feedback, the stimulation of the quadriceps and hamstrings, due to the synergy-based feedforward component, was ill-timed and ineffective, e.g., the flexor muscles were activating when the desired motion was in the extension direction. A possible cause of this is that the synergies extracted through PCA were overly complex and abstruse, e.g., the negative synergy activation's and negative synergy values for the stimulation, which is always positive. Another possible cause of this, is the co-activation of antagonistic muscle pairs in each synergy, which becomes problematic when one muscle is more sensitive than the other. For these reasons, it is hard to justify the usefulness of these synergies extracted through PCA in the control scheme.

In this chapter, the remaining objective of the primary research goal, the experimental demonstration of the adaptive synergy-based DSC controller with delay compensation in walking experiments on human subjects, is presented. In addition to achieving this research objective, the methods to find synergies for the feedforward component are improved upon. Instead of using PCA to extract the synergies from the optimal inputs pre-computed through dynamic optimizations, the synergies were designed prior to performing the dynamic optimizations. One of the purposes of muscle synergies in human motor control is to reduce the

complexity of the system by reducing the input space and redundant DOF by activating them in predetermined patterns. Similarly, designing the synergies prior to the optimizations will help restrict the input space to help prevent the co-activation of antagonistic muscle pairs and ill-timing of stimulation. To do this, an alternative form of synergies were determined based on the key dynamic postures observed during gait. Dynamic postures is defined as the position of the body/joints at any moment during a movement pattern. For gait, the swing phase is composed of two key dynamic postures; the withdrawal reflex and knee extension. Using optimizations, I computed the synergies that produced these dynamic postures when activated. Then, separate dynamic optimizations are used to find their optimal activation to reproduce gait. In addition, these dynamic optimizations were modified to include the double support phase (DSP) part of the gait sequence when the body is supported by both legs. During the DSP the load transfers from the stance leg to the swing leg and the legs switch roles, i.e., the stance leg from the previous step becomes the swing leg for the next step and vice versa. The dynamic postural synergies, their activations, and the optimal trajectories they produced were then used for the experimental demonstration of the synergy-based PID-DSC controller for walking in a hybrid neuroprosthesis on an able-bodied subject.

The remainder of this chapter is organized as follows. Section 7.2 covers the methods used to compute the dynamic postural synergies and their activations. Section 7.3 will present the Finite State Machine (FSM) used for the experiments. The experimental results for one able-bodied subject walking using the hybrid neuroprosthesis will be presented in Section 7.4. Sections 7.5 & 7.6 will conclude this chapter with a discussion and conclusion.

7.2 DYNAMIC POSTURAL SYNERGIES

7.2.1 Computing the Synergies

Theoretically, if the movement patterns from a gait sequence can be broken down into a finite number of dynamic postures and their corresponding synergies can be computed, then these synergies can be activated in a sequence to reproduce gait. In studies by Bajd et al. [7]

rudimentary gait for subjects with SCI is produced by first flexing the hip, produced through the withdrawal reflex, and then knee extension. The withdrawal reflex is induced through the stimulation of the peroneal nerve and the knee extension is produced by stimulating the quadriceps muscle group. The withdrawal reflex is an involuntary spinal reflex triggered when a damaging stimulus is sensed by the foot. When the peroneal nerve, located near the pit of the knee joint, is stimulated above pain threshold this reflex is triggered and results in the flexion of the hip, knee, and ankle joint [62]. When followed by the stimulation of the quadriceps, the knee extends and the subject could lean forward until their foot makes contact with the ground. Using these two key motions, the swing phase of gait can be recreated. Instead of using peroneal nerve stimulation, I found the dynamic postural synergies that distributed the effort to all the available actuators that result in the key dynamic postures created as a result of the withdrawal reflex and knee extension. I then used dynamic optimizations to compute the optimal synergy activations that reproduced gait.

The dynamic postural synergies are computed using optimizations that use the 4-link walking model. The 4-link walking model was modified to reflect the hybrid neuroprosthesis testbed, therefore, only the hip motors, knee motors, and the antagonistic muscle pairs of the knee joint are used. The parameters used for this model were taken from [78] for an able bodied person. Optimizations were conducted to compute the synergies that distribute the effort to the 4 inputs that minimize the error between the desired dynamic posture and the resulting motion. The joint angles for the desired dynamic postures were taken from the optimal trajectories in chapter 3. For these optimizations, the convex cost function's objective was to minimize the dynamic posture's position error and minimize the activation states of the system and is defined as

$$\min_w \Pi = \int_{t_0}^{t_f} (e(t)^T Q e(t) + \mu(t)^T R \mu(t)) dt \quad (7.1)$$

subject to: $M(q)\ddot{q} + C(q, \dot{q})\dot{q} + G(q) + f(q, \dot{q}) = b(q, \dot{q})\mu$

$$\mu \in [\mu_l, \mu_u]$$

where dynamic posture's position error is defined as $e = q_{dp} - q$, q_{dp} is the joint positions for the desired dynamic posture. In 7.1 $Q \in \mathbb{R}^{4 \times 4}$ is a weight on the position tracking error,

the matrix $R \in \mathbb{R}^{4 \times 4}$ is a positive-definite matrix of weights on the activation vector, and the lower and upper bound on the activations are defined as μ_l and $\mu_u \in \mathbb{R}^4$. Based on the selection of the input weight matrix R , the distribution of the effort from the motors or stimulation can be emphasized. These optimizations were performed by using Matlab's `fmincon` function (MathWorks, Inc.). The simple synergies computed through the optimization and the postures they produce; withdrawal reflex and knee extension, can be seen in Fig. 7.1. The first dynamic postural synergy activates the hip motor to produce a moment at the hip in the flexion direction, and activates the knee motor and knee flexor to produce a moment at the knee in the flexion direction, to produce the withdrawal reflex. The second dynamic postural synergy activates the hip motor to produce a smaller moment at that hip to maintain the hip joints position, and activates the knee motor and knee extensor to produce a moment at the knee to fully extend the knee joint. It can be observed that these dynamic postural synergies are less complex and have no co-activation of the antagonistic muscle pairs when compared to the synergies extracted through PCA in chapter 6.

7.2.2 Computing the Synergies' Activation

Unlike the synergies extracted through PCA used in Chapter 3, these dynamic postural synergies were determined using separate optimizations prior to these dynamic optimizations. Using these already computed dynamic postural synergies, these dynamic optimizations now compute the optimal synergies' activations in order to complete a step.

In order to consistently and easily maintain the initial condition during experimentation, the subject will start the gait process while standing upright. Therefore, two sets of dynamic optimizations are computed; one for a half step (0.2 meters) and the second for a full step (0.4 meters). In addition, unlike the dynamic optimizations from Chapter 3, these results include the DSP, i.e., the swing leg has to reach the desired position, where the swing leg makes contact with the ground, in the allotted time, $t_{step} = 1$ sec., and maintain that position, i.e., maintain contact with the ground, for a predetermined duration, $t_{DSP} = .5$ sec.

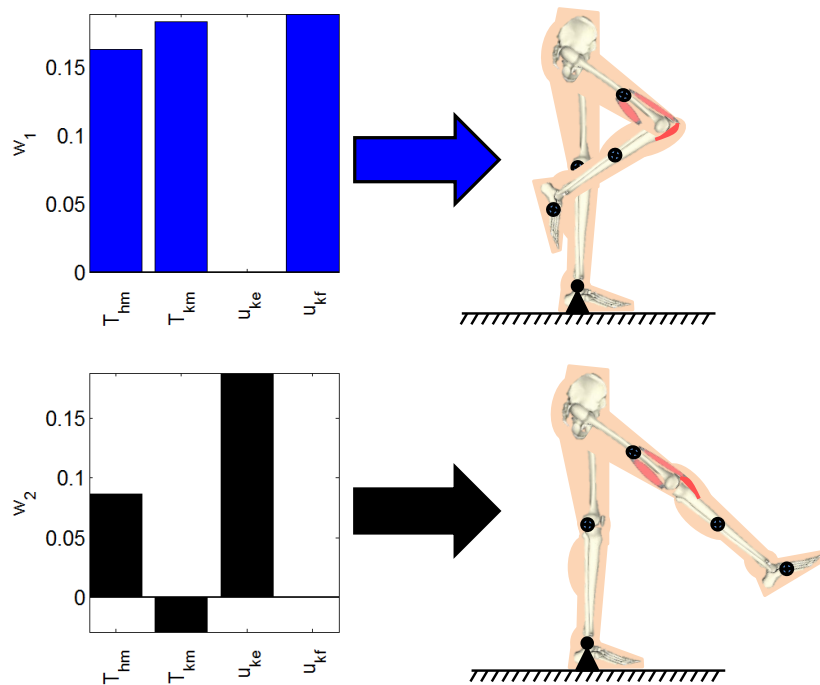


Figure 7.1: The dynamic postural synergies computed through the optimizations and the dynamic postures they result in when activated.

For these optimizations, the convex cost function's objective was to minimize the synergy activation for the full duration and the final position error from $t = t_{step}$ to $t = t_{DSP}$. The cost function is defined as

$$\min_{c, M_w} \Pi = \int_{t_0}^{t_f} (c(t)^T R c(t)) dt + \int_{t_{step}}^{t_f} (e(t)^T Q e(t)) dt + \Pi_{extra} \quad (7.2)$$

subject to: $c \in [c_l, c_u]$

where final position error is defined as $e = q_f - q$, q_f is the final joint positions for a complete step, $R \in \mathbb{R}^{2 \times 2}$ is the positive-definite weight matrix for the synergy activation, $Q \in \mathbb{R}^{3 \times 3}$ is the positive-definite weight matrix for the the joint angle errors, and the lower and upper bound on the synergy activations are defined as c_l and $c_u \in \mathbb{R}^2$. In the cost function t_0 is the time in which the step begins and t_f is the final time for the step and is defined as $t_f = t_{step} + t_{DSP}$. The last variable in the cost function, Π_{extra} is an addition cost that is activated when certain undesirable events occur in the solution, e.g., the foot drags on the ground or the swing leg overshoots.

These optimizations were performed using a genetic algorithm particle swarm optimization (GAPSO) method to minimize the cost function. This was done by generating a random guess population of a predetermined size, in this case 5000, in between the upper and lower bounds, c_l and c_u . The sample time of the optimization variables was selected to be $T_{sopt} = .25$ sec. and then interpolated to the simulation sample time T_{sim} using a cubic fit. Then the cost function for each guess of the population is evaluated by simulation the gait model at $T_{sim} = .001$ sec. Then based on the genetic algorithm, the cost of the guess population is split into three categories; the guesses with the lowest 40% costs are labeled as the Select group, the next 40% are labeled as the Crossover group, and the last 20% are labeled as the Mutation group. The particle swarm part of the algorithm then modifies the Select group portion of the population to approach the guess with the lowest cost. The Crossover group mixes segments of the guesses to generate a new portion of the population, and the mutation group randomly generates that portion of the population. The algorithm then moves on to the next iteration where it re-evaluates the cost of the new population and

repeats the aforementioned operations. This process is repeated for a predetermined number of iterations, in this case 25 iterations.

The dynamic postural synergies, their activations computed through the optimizations, the joint trajectories they produce, and the sequence gait sequence for the half step and full step can be seen in Fig. 7.2 and Fig. 7.3, respectively. From gait sequences, it can be observed that the optimizations computed the synergy activations to complete the step, whether half or full, and maintained contact with the ground throughout the DSP while interacting with the ground reaction model. In addition, it can be seen that the dynamic postural synergies are activated in sequence as intended, i.e., for the first 0.5 sec. primarily the first synergy is activated and then for the remainder of time primarily the second synergy is activated. Even though the model completes the step by around 1 sec. the second synergy is still activated for the remainder of the time, this is to keep the knee from buckling since both legs are supporting the body during this phase.

One thing to note for the full step results, is as the swing leg leaves the ground, the stance leg is leaning back which is not typical for normal gait. This is because this system does not currently include actuation at the ankle joints to produce push off. During normal gait the first part of the gait sequence is push off, as a result of the planter flexion of the ankle, to propel the body forward. The differences between gait with and without push off can be seen when comparing these results to the walking simulation results in chapter 3 where ankle actuation is present. If the push off phase is to be included in this system, it would have its own dynamic postural synergy.

7.3 FINITE STATE MACHINE

The hybrid neuroprosthesis used for experimental demonstration uses 4 electric motors; one on each hip joint and knee joint, and 4 stimulation channels; the quadriceps and hamstrings of each leg. The hybrid neuroprosthesis is controlled using two of the adaptive synergy-based PID-DSC controller with delay compensation working in tandem to produce gait, one for each leg. The Finite State Machine, shown in 7.4, is used to determine which trajectories

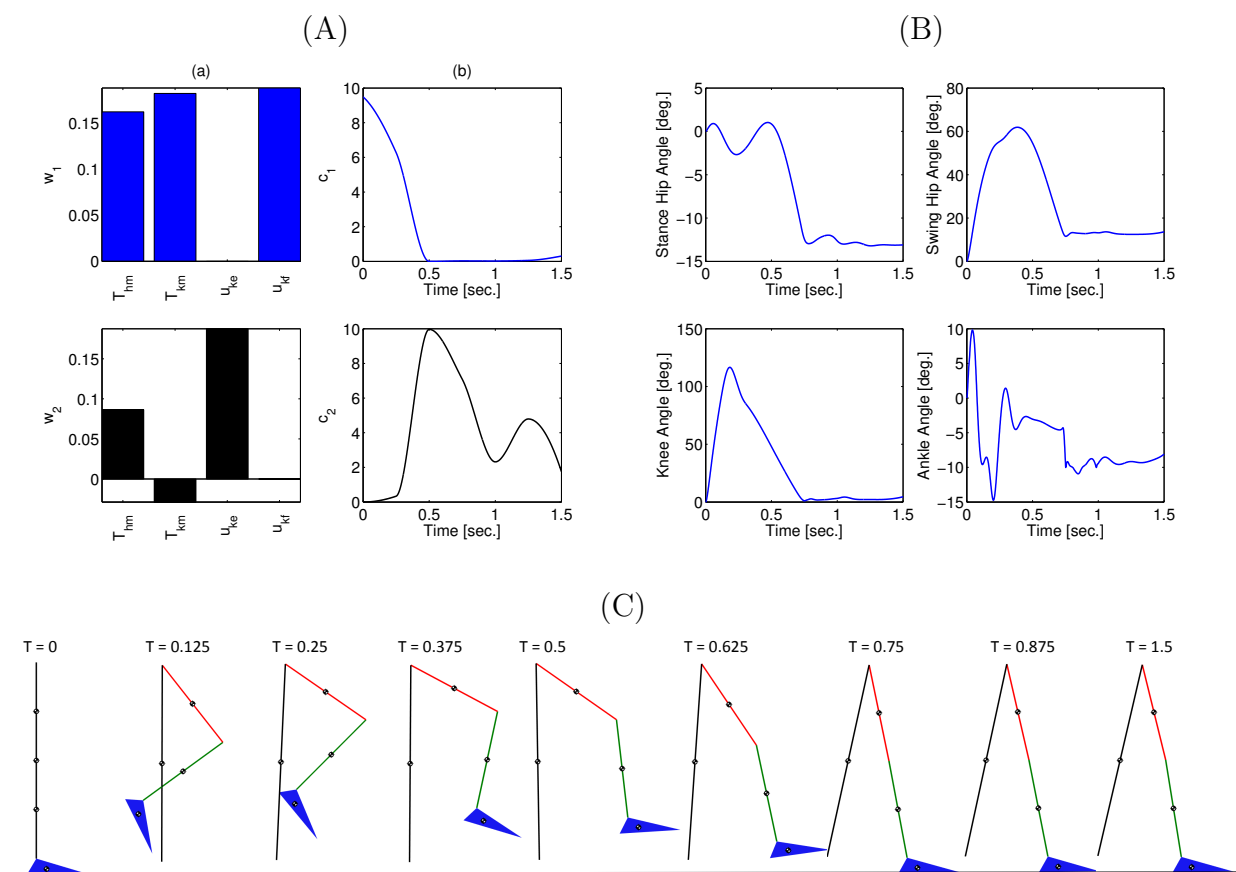


Figure 7.2: (A) The dynamic postural synergies (a) and their activation to produce a half step (b), (B) the joint trajectories they produce, (C) the gait sequence for the half step.

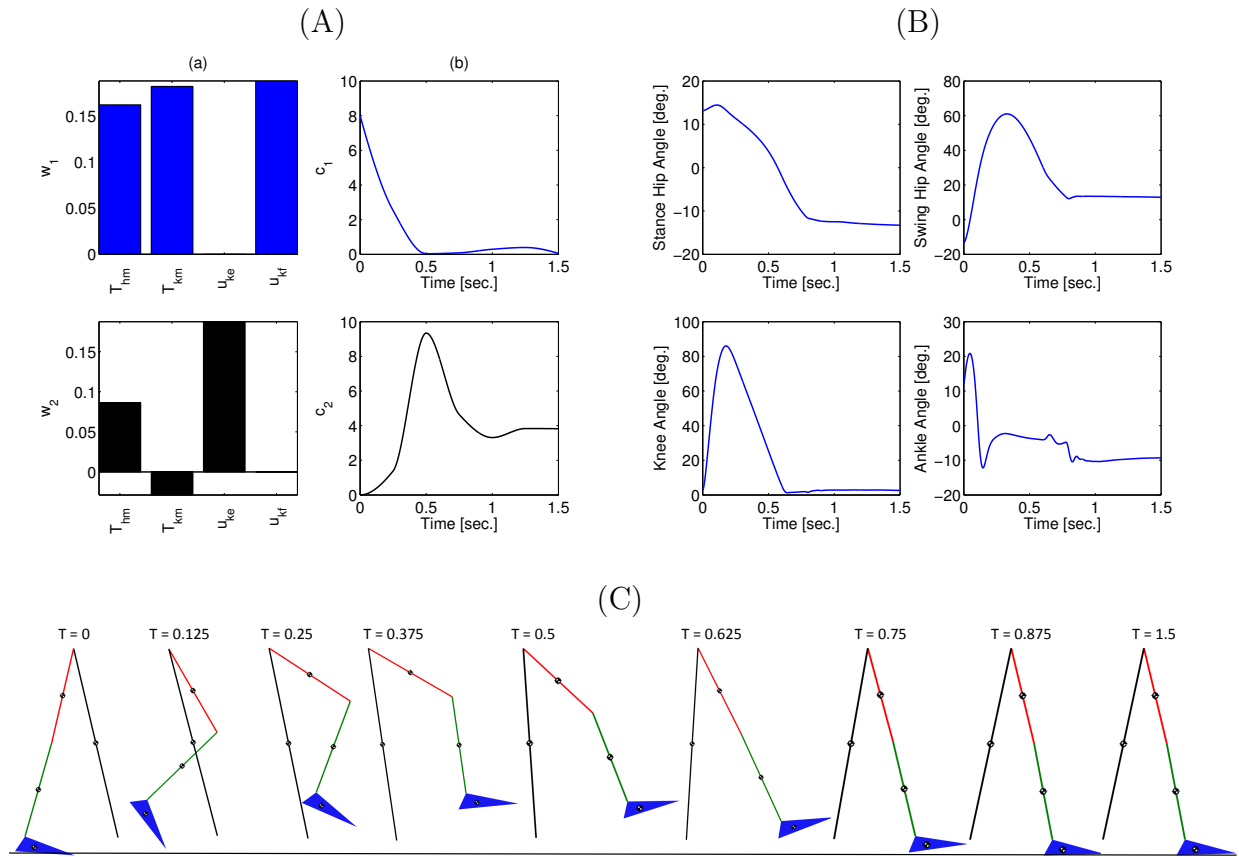


Figure 7.3: (A) The dynamic postural synergies (a) and their activation to produce a full step (b), (B) the joint trajectories they produce, (C) the gait sequence for the full step.

and synergy activations of the gait sequence are used; i.e., either half right step (State 1), full left step (State 2), or full right step (State 3). In between the active states; State 1-3, the standby state (State 0) is activated by default, in which the motors at the joints hold their positions and the synergy activations are set to zero. When a leg is activated in a state, it becomes the swing leg and its counterpart becomes the stance leg. When a leg becomes the stance leg the controller only uses feedback to track the stance hip trajectory and hold the position of the knee joint. The progression of the FSM is determined by the progression button, in which the first time it is pressed State 1 is activated, then each time it is pressed after that the even transitions activate State 2 and the odd transitions activate State 3. In addition to the progression button, there is a safety button which turns off all inputs when pressed.

7.4 EXPERIMENTAL RESULTS

The overall control system was experimentally demonstrated on an able-bodied subject (male; Age: 27 years). For these experiments it is assumed that the behaviour of the right and left leg are similar, therefore, both States 2 and 3 use the same synergies and activations computed in the previous sections. The optimizations to compute the synergies, their activations, and the trajectories they produce were performed using the subjects height and weight, but the model used the muscle parameters reported in [78] for an able-bodied subject. If this system is to be implemented on a subject with a injury/disorder in which one of their leg's response is much different than their other such as in hemiplegia due to a stroke, it would probably be more beneficial to use multiple subject-specific models, one for each leg.

Prior to any experimentation, an approval from the Institutional Review Board at the University of Pittsburgh was obtained. During the experiments, the subject was instructed to relax and refrain from voluntarily interfering with the hybrid exoskeleton. The estimates of the EMD, activation time constants, and fatigue/recovery rates from Chapter 6 were

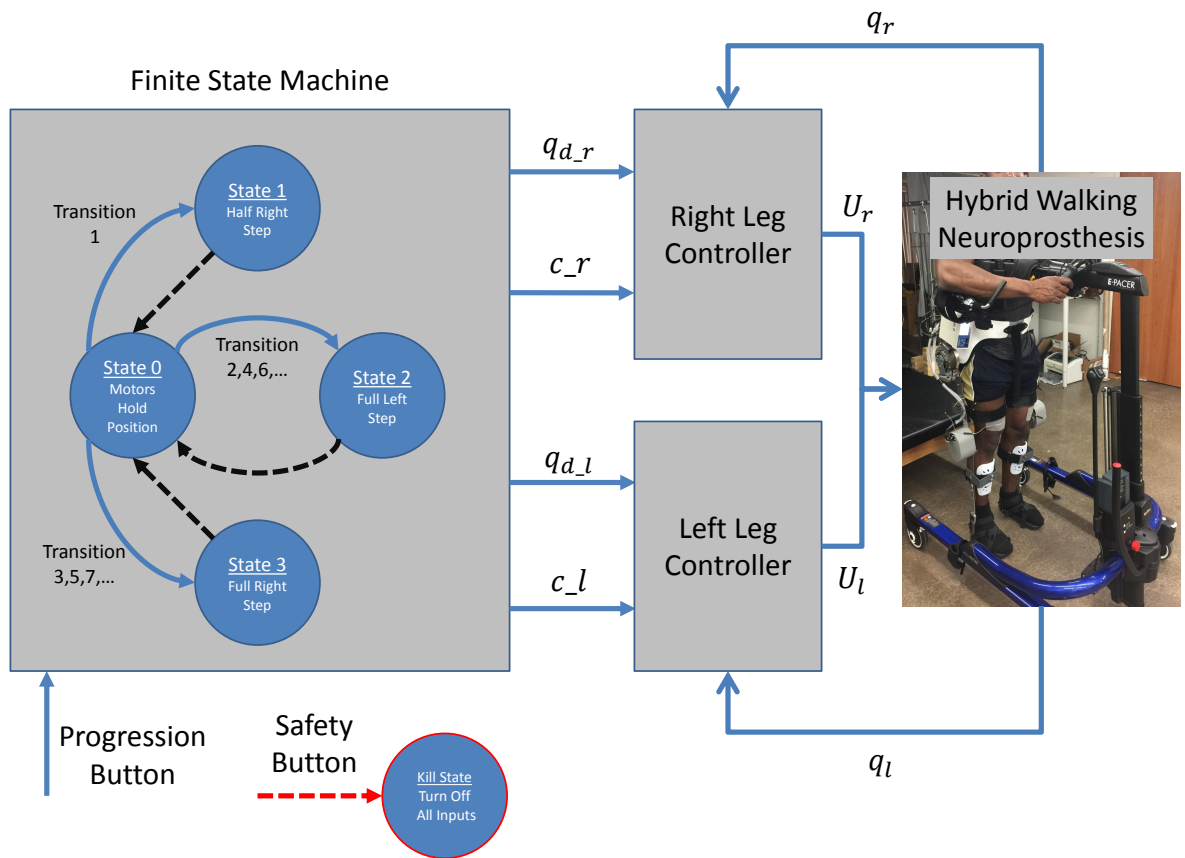


Figure 7.4: The Finite State Machine determines the desired trajectories and synergy activations based on what state is activated; either half right step, full left step, or full right step. Then two controllers are used, one for each leg, which work in tandem to produce gait.

used and assumed to be the same for both legs. During the experiments, the subject used gait assistive device called the E-Pacer (Rifton, USA) to help support and propel himself forward. The progression and safety buttons were operated by a separate user and were used to control the FSM. The experiments were run for 6 steps, including the half right step.

The experimental result can be seen in Fig. 7.5 - 7.10. The tracking performance for both the right and left hip and knee joints can be seen in Fig. 7.5 (A). Fig. 7.5 (B) shows a sequence of frames from the video footage illustrating the gait produced using the control system. The root mean squared errors for the hip and knee joints were found to be 1.56° and 0.92° , respectively, for the right leg, and 0.87° and 1.77° , respectively, for the left leg. The desired feedforward component, $\hat{\phi}^{-1}\zeta_{sf}W\hat{c}$, and desired feedback component, kr , in $\bar{\mu}$ can be seen in Figs. 7.6 & 7.7. As seen in Fig. 7.8 and the lack of increase in the desired feedforward activations in Fig. 7.6 the effects of the fatigue estimate is not as apparent in the experiments. Once again, this is because the fatigue parameters identified for the able-bodied subject were very slow resulting in the muscles barely fatiguing. However, for SCI subjects muscle fatigue occurs more rapidly, hence this is still a practical feature in the controller.

The actual input signals for all 8 inputs of the system can be seen in Fig. 7.9. Fig. 7.10 shows the dynamic postural synergies and how they are activated, for the right and left leg, throughout the experimental trial. It can be observed, that when a leg takes the role of the stance leg, the synergy activation is zero which results in zero stimulation and zero desired feedforward motor activation. Hence, only feedback control of the motors is used to lock the knee joint of the stance leg. From the inputs, we can see that the timing of the stimulation is logical as for each step the flexors is activated first to produce the withdrawal reflex and then the extensors to fully extend the knee. Further, based on the verbal feedback from the subjects, the timing of the stimulation for the flexors and extensors was more effective/logical using the dynamic postural synergies as opposed to the synergies extracted through PCA.

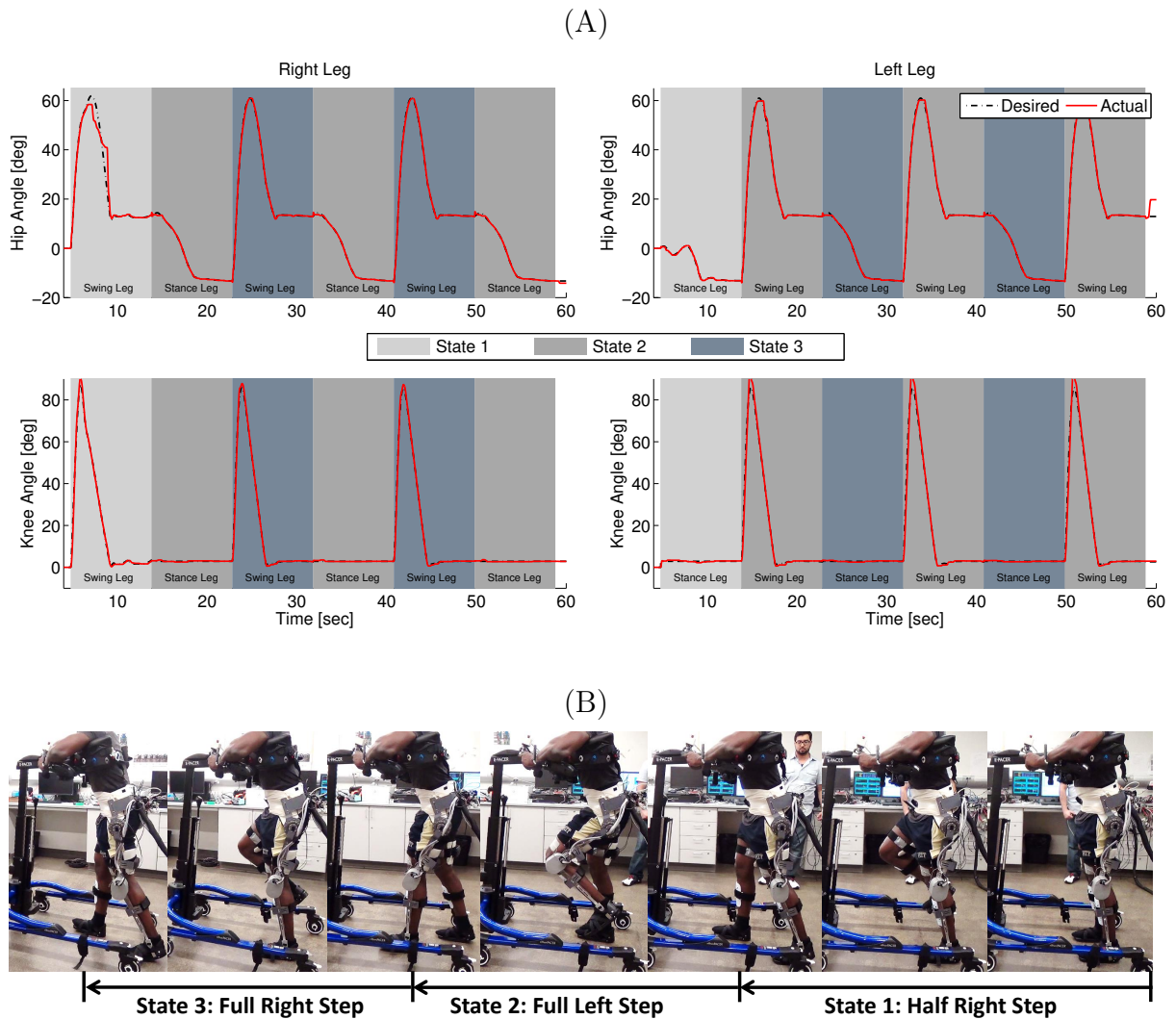


Figure 7.5: (A) The desired and actual joint angles of the right and left hip and knee joints resulting from using the developed synergy-based DSC/DC control system in conjunction with the FSM on an able-bodied subject. The shaded regions indicate which state of the FSM is active at that time. In addition, the role of the leg; whether it is the stance leg or swing leg, is also indicated. (B) A sequence of photos illustrating the gait produce during the experiments.

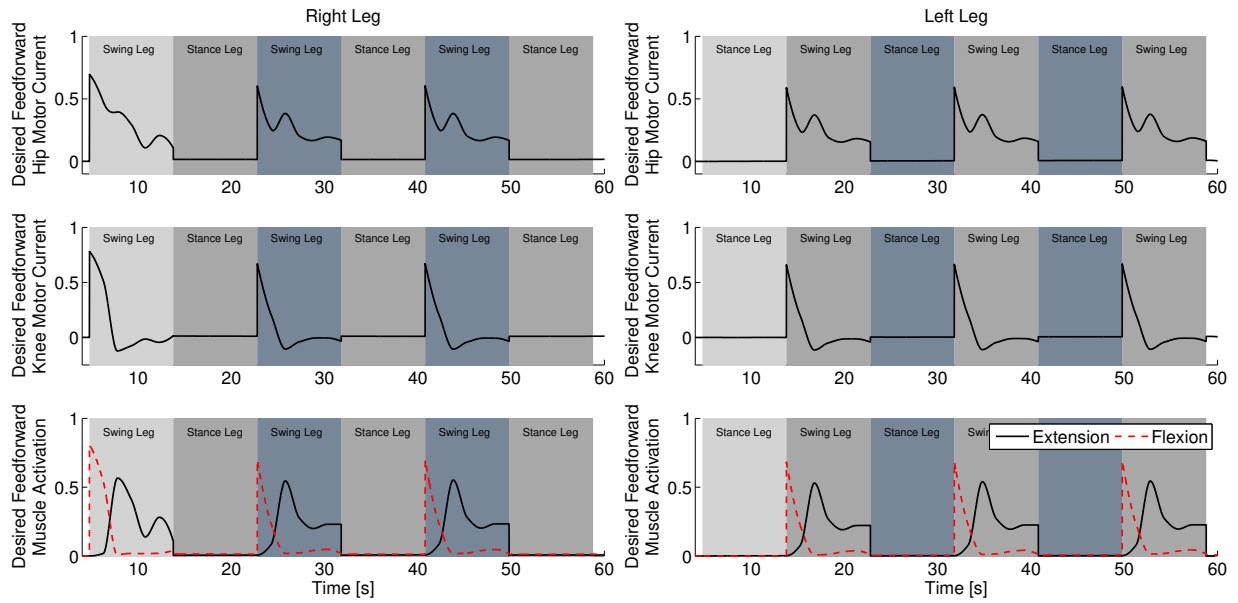


Figure 7.6: The desired feedforward component of $\bar{\mu}$ for all of the system inputs. This component is generated from the dynamic postural synergies and their activation after adaptation and with the scaling up from the fatigue estimate and the scaling factor control gain.

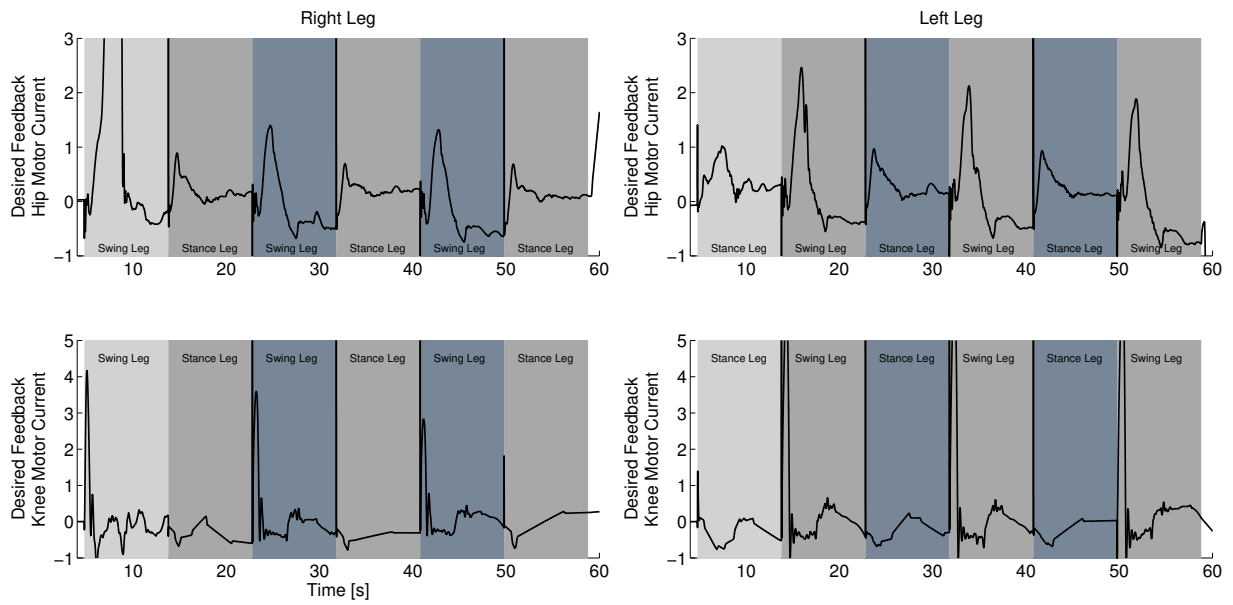


Figure 7.7: The desired feedback component of $\bar{\mu}$ which is only applied to the four motors at the hip and knee joints of each leg. It can be observed that they majority of the effort is occurring during the swing phase of each leg.

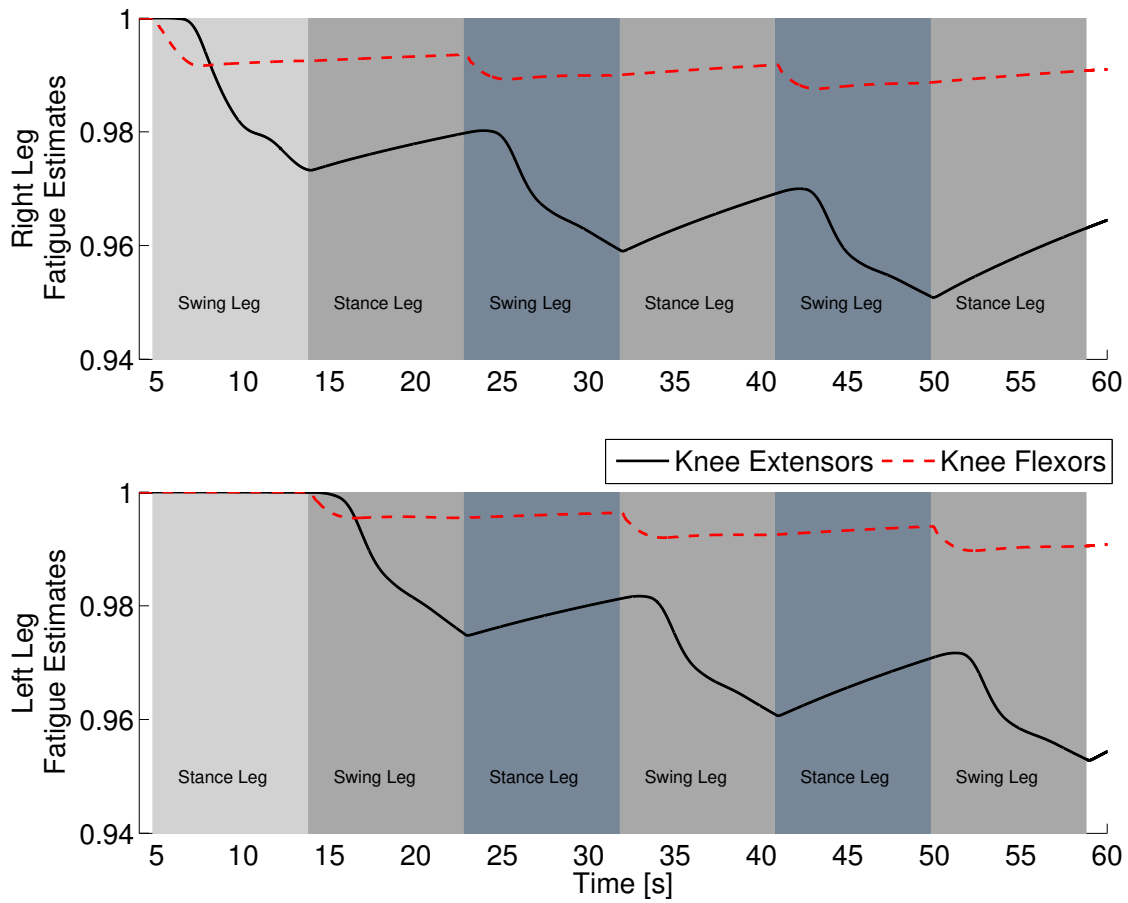


Figure 7.8: The fatigue estimates for the knee flexors and extensors of both legs. The fatigue estimate ranges from 1 to ϕ_{min} , which corresponds to no fatigue to fully fatigued, respectively. It can be observed that the fatigue occurs during the swing phase, and the muscles recover during the stance phase since there is no stimulation.

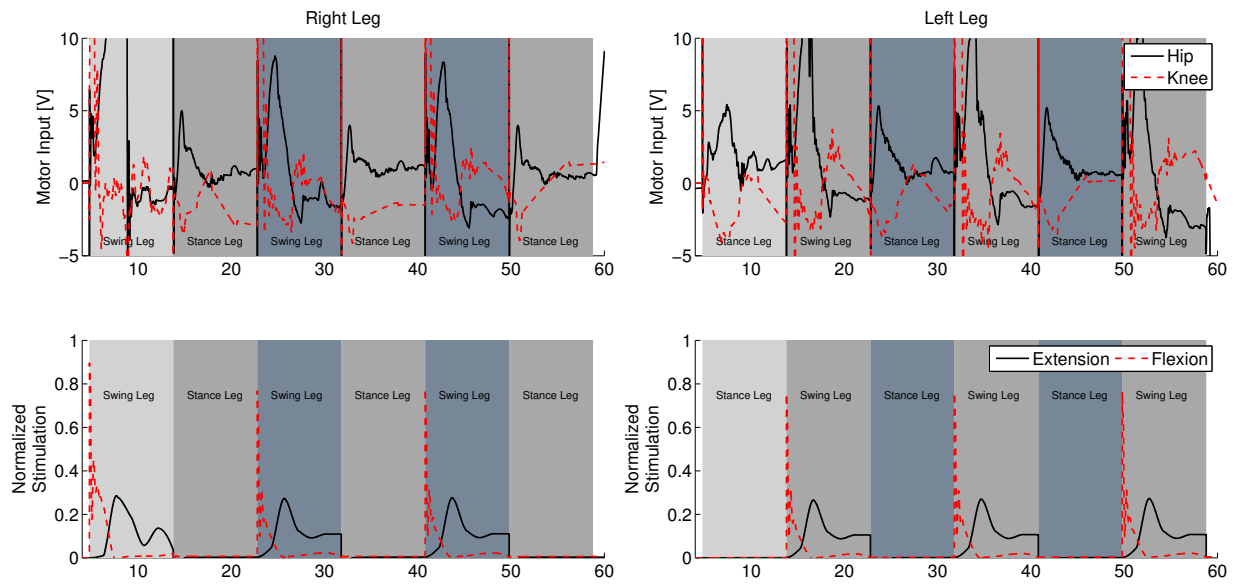


Figure 7.9: The inputs to all of the system inputs for this experimental trial. Note that there is no stimulation occurring during the stance phase of each leg.

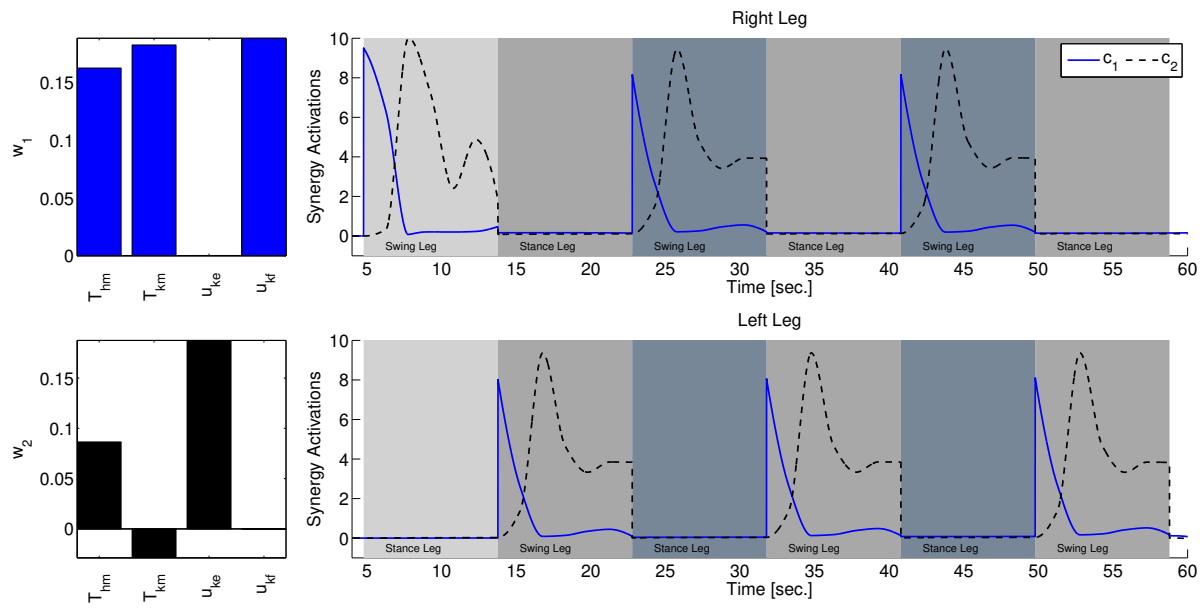


Figure 7.10: The synergy activation after adaptation for both legs. Note that the synergies are not activated during the stance phase of each leg.

7.5 DISCUSSION

Hybrid exoskeletons come in many configurations including any combination of FES, active actuators such as electric motors, or passive actuators such as controlled brakes and wrap spring clutches [35, 57, 79, 108]. This newly developed controller employs a control structure in which simultaneous control of electric motors as well as FES is used instead of fine control of FES using controlled brakes. The latter approach, which is used in [31], uses open-loop control of stimulation to provide the active torque and controlled brakes are used like a dynamic stopper to restrict a single joint to a desired joint angle. In [42], this method was extended to a full orthosis with FES and controlled brakes at both the hip and knee joints of each leg. The method was tested on four paraplegic subjects. The disadvantage of this method is that the antagonistic muscles are stimulated at the maximum stimulation to generate a raw joint torque, which is fine tuned through the controlled brakes. This results in massive over stimulation of the muscles leading to the rapid onset of muscle fatigue. Later in [57], a hybrid neuroprosthesis with 16 intramuscular stimulation channels combined with a locking orthosis was tested on able-bodied and SCI subjects. The hybrid neuroprosthesis was controlled with an FSM with predetermined open-loop control signals for FES for multiple tasks such as sitting, standing, walking, and ascending and descending stairs. Unlike the aforementioned papers, in [82] a combination of FES and active actuators (electric motors) were used to control knee extensions using an adaptive gain-based controller to allocate the control effort. In [21] and [45] a cooperative controller for hybrid knee-ankle-foot exoskeletons were tested on human subjects. The controllers used an FSM that coordinated the PD controller for the electric motors and an iterative learning controller (ILC) for FES. In [21], the FSM also uses a fatigue estimator to detect the onset of fatigue and modify the stimulation parameters. Although the aforementioned control approaches are interesting, the methods did not consider control of multiple muscle stimulation and multiple electric drives applied to multiple DOFs. Further, these control methods do not follow a formal control development and do not provide stability guarantees.

The control system developed for hybrid walking exoskeletons in this dissertation follows a systematic control design approach. The approach is inspired from the human motor

control concept of muscle synergies. In most studies, muscle synergies are proposed as a basis employed during human motor control and found by recording EMG signals (collected from multiple muscles) which are then decomposed to extract muscle synergies. Unlike these studies, in this chapter dynamic postural synergies are designed to be used as a basis for the control system for the walking hybrid neuroprosthesis. This synergy design approach, using optimizations to distribute the control effort among the available actuators, offers multiple advantages and convenience such as allowing for the incorporation of external inputs, i.e., electric motors and FES. Another benefit for this method of designing dynamic postural synergies is the ease of adding additional restrictions on the synergies, i.e., no co-activation or no negative stimulation. While, the developed control system was capable of reproducing gait, the finite state machine can still be scaled-up to achieve motions other than gait such as sitting/standing and ascending/descending.

A general set of synergies that are applicable to multiple tasks/movements such as different step lengths and gait speeds, sitting/standing, or ascending/descending stairs would provide a comprehensive data set to accomplish a control design for the hybrid neuroprosthesis. An optimization algorithm, such as the one used in [9], may be used to extract a more general set of synergies from a reduced model (lower dimensional) and used with this controller for a general task. However, unlike the synergies extracted using PCA, since the dynamic postural synergies are computed before the dynamic optimizations, they are more generalizable for different step lengths and gait speeds. In addition they may also be used for ascending/descending stairs studies. This can be achieved by designing a library of synergies that encompass walking, sitting, and standing. Also, because these optimizations are model based, extensive system identification experiments are required to find the subject specific parameters that are used in the models. The use of non-selective nature of transcutaneous stimulation limits the DOF the system has control of which downplays the true benefit of the synergy-based PID-DSC controller, dealing with large high DOF systems. Alternatively, an invasive FES system such as in [111], may provide access to over 40 different lower-limb muscles. Therefore, the synergy-based PID-DSC controller may be a very good candidate for the hybrid neuroprosthesis system proposed in [57].

7.6 CONCLUSION

In this chapter, the adaptive synergy-based DSC controller is experimentally tested on an able-bodied subject walking using a hybrid neuroprosthesis. Unlike previous chapters, these experiments used dynamic postural synergies instead of the synergies extracted through PCA. These synergies were designed to reproduce the key dynamic posture; the withdrawal reflex and knee extension, which have been shown to be able to reproduce gait. Dynamic optimizations were then used to compute the optimal synergies' activation to produce a half step and full step. A finite state machine was developed to switch between the trajectories and synergy activations depending on three states; half right step, full right step, and full left step. The control system then used two of the synergy-based DSC controller, one for each leg, which worked in tandem to reproduce gait. The experiment was conducted on an able-bodied subject. The overall control system showed ability recreate gait using the hybrid neuroprosthesis and the gait assistive device.

8.0 SUMMARY

Each year approximately 3,400 people are diagnosed with complete paraplegia due to a spinal cord injury. This disability impairs their walking function and reduces their quality of life. The two most common gait restoration technologies used to restore these subjects walking function are functional electrical stimulation-based systems or powered exoskeletons. Functional electrical stimulation is the application of external artificial stimulation to the muscle groups by either using transcutaneous or intracutaneous stimulation to elicit muscle contractions that produce movements. When activated in a coordinated sequence, FES has been shown to be able to restore gait in persons with disabilities. In addition, the use of FES has been shown to have multiple therapeutic health benefits. However, the use of external artificial stimulation has been shown to rapidly increase the onset of muscle fatigue, which limits the duration of walking when using solely FES-based systems. The alternative approach to gait restoration is powered exoskeletons, which use external sources of actuation such as electric motors. These devices have been shown to be capable of restoring gait and achieving longer walking durations than typical FES-systems; however, these devices can be larger and bulkier, making them less feasible. Recently, there have been efforts to combine the two means of actuation, FES and motors, into gait restoration devices called hybrid neuroprostheses. The use of FES can provide supplementary torque, which allows for smaller motors that require less energy storage, and have added health benefits for the user such as improved cardiovascular health and increased muscle mass and bone density.

The primary goal of this research was the derivation of a human motor control-inspired control system with a guarantee of stability for a walking hybrid neuroprosthesis. Particularly, this research addresses the technical challenges associated with the real-time control of the actuation methods used in a hybrid neuroprosthesis: FES and electric motors. The con-

control of FES can be difficult due to the nonlinear muscle dynamics, Ca^{2+} activation dynamics, electromechanical delays, and muscle fatigue. In addition, the hybrid actuation structure, which combines FES and electric motors, introduces an actuator redundancy problem. This research overcomes these challenges by using Lyapunov based control design methods that consider these problems in the control development and stability analysis. In addition, this research used concepts and methods from human motor control theory and incorporated them into the derived control system while guaranteeing stability. Instead of addressing all four challenges at once, which can be a daunting task, this body of work addressed each challenge individually through simpler systems and testbeds.

The different models and testbeds used throughout this work are presented in Chapter 2. These models include the 4-link walking model which models a person walking in a hybrid neuroprosthesis while using an assistive device like a walker. The individual controllers to address the EMD and the actuator dynamics were developed for the 1-DOF knee extension model, which represents a person sitting in a leg extension machine with their quadriceps being stimulated. The final model is the fixed hip model which represents a person standing on one leg while the other leg, using one side of the hybrid neuroprosthesis, is free to swing without interacting with the ground. The testbeds on which these models are based on are a full walking hybrid neuroprosthesis that uses a combination of electric motors and FES at the knee flexors and extensors, and a modified leg extension machine instrumented with an incremental encoder and load cell. Using these musculoskeletal models, this research uses nonlinear control techniques to help derive novel control systems that address the challenges of actuator redundancy, actuator dynamics, electromechanical delays, and muscle fatigue.

8.1 CONTRIBUTIONS

The efforts of this research produced the following contributions to the field of real-time closed-loop control of FES-based systems and hybrid neuroprostheses.

1. The derivation of a novel human motor control inspired control system for a walking hybrid neuroprosthesis. The control system address the four challenges associated with

real-time control of a hybrid neuroprosthesis; actuator redundancy, electromechanical delays, actuator dynamics, and muscle fatigue. This controller uses the concept of synergies in the feedforward path to solve the actuator redundancy problem and feedback control for the motors to improve tracking performance. A modified dynamic surface control structure is used to account for the actuator dynamics. The DSC structure is augmented with a delay compensation term to deal with the EMD associated with FES. The controller also includes an inverse of the fatigue estimate to increase stimulation levels in the feedforward component as the muscles fatigue. This contribution is the result of achieving objectives 1, 2, & 3 of the research objectives listed in Chapter 1.2.

2. The incorporation of the concept of muscle synergies, for the first time, in real-time closed-loop control systems to address the actuator redundancy challenge. Until this work, synergies were a human motor control concept typically used for motion analysis. This work uses the concept of synergies to reduce the input space in the feedforward path and to dimensionally reduce the input space and couple multiple DOF to active in unison. This contribution is a result of achieving objective 1 of the research objectives listed in Chapter 1.2.
3. Dynamic postural synergies were designed to reproduce two key dynamic postures; the withdrawal reflex and knee extension, which have been shown to be able to reproduce the swing phase of gait. Dynamic optimizations were then used to compute the optimal synergies' activation to produce a half step and full step. An update law is derived to adapt the synergy activation in real-time to further improve the effectiveness of the synergies. This contribution is a result of achieving objective 1 of the research objectives listed in Chapter 1.2.
4. The experimental demonstration of the synergy-based PID-DSC controller on an able bodied human subject in the hybrid neuroprosthesis. A finite state machine was used to transition between the different states of a gait sequence; half step and full steps. A finite state machine is developed to switch between the trajectories and synergy activations depending on three states; half right step, full right step, and full left step. The control system then used two of the synergy-based PID-DSC controller, one for each leg, which worked in tandem to reproduce gait. The experiments were conducted on an able-bodied

subject in which the subject took 6 steps in the hybrid neuroprosthesis. The overall control system showed the ability to recreate gait using the hybrid neuroprosthesis and the gait assistive device. This contribution is a result of achieving objective 4 of the research objectives listed in Chapter 1.2.

5. The derivation and experimental validation of the standalone PID-based delay compensation controller for a 1-DOF FES-driven musculoskeletal system with EMD. A Lyapunov-based stability analysis yielded semi-globally uniformly ultimately bounded tracking despite model uncertainties and EMDs. This contribution is a result of achieving objective 2 of the research objectives listed in Chapter 1.2.
6. The experimental comparison of the PID-DC controller with two nonlinear controllers: PD-DC (previous control design for EMD compensation with no integral control) and RISE controller. The addition of the integral action resulted in improved performance that was validated on four able bodied subjects. The results showed that the PID-DC has a superior tracking performance (statistically significant) compared to the other two controllers. Further, the new controller was shown to be robust to variations in the measured EMDs. This controller was also tested on a person with a SCI where it provided adequate tracking performance. This contribution is a result of achieving objective 4 of the research objectives listed in Chapter 1.2.
7. The derivation of the standalone PID-DSC tracking controller for musculoskeletal systems with input delays in the activation dynamics. The controller uses a dynamic surface control structure to deal with the activation dynamics, which are cascaded to the musculoskeletal dynamics. Model-based estimators are used to estimate the unmeasurable activation states in real-time implementation. In addition, the DSC framework was augmented with the delay compensation term to deal with the input delay in the activation dynamics. A Lyapunov stability analysis was performed to prove UUB tracking performance. This contribution is a result of achieving objective 2 of the research objectives listed in Chapter 1.2.
8. The experimental validation of the PID-DSC on two able-bodied subjects and a subject with a SCI by comparing it with its predecessor, the PID-DC, which does not consider activation dynamics. A t-test statistical analysis was performed and determined that the

PID-DSC outperformed the PID-DC at a 95% confidence level. This contribution is a result of achieving objective 4 of the research objectives listed in Chapter 1.2.

8.2 FUTURE WORK

The conclusion of this research resulted in a novel human motor control inspired control system that has been shown to be capable of achieving gait restoration experimentally on able bodied subjects. This provides a foundation for future research in human motor control inspired control systems for walking hybrid neuroprostheses. However, there are still areas where improvements need to be made.

For instance, while the synergy-based feedforward component was capable of solving the actuator redundancy problem, the over control system can still be improved by incorporating the synergies in the feedback path. The challenge of achieving this is that the synergies are defined to effect multiple DOF when activated. Therefore, in order to use the synergies in the feedback loop, the errors for the multiple DOF have to be mapped to a single variable since the activation for each synergy is a constant. With the introduction of the dynamic postural synergies in Chapter 7, the motions they create are more defined. This makes it easier to develop a mapping to convert the errors from the multiple DOF to one synergy activation. One possible method to do this would be to isolate one key degree of freedom to each synergy and use that to derive a feedback control law for the synergy activation. For instance, for the first synergy which results in the withdraw reflex, the key motion would be the hip joint angle as it is the primary DOF that swings the swing leg forward. For the second synergy the key DOF would be the knee angle as this is the primary joint being effected through that synergy.

Another area where this research can be expanded, is the experimental validation of the control system on subjects with SCI. Since the control system was demonstrated on an able body subject, and was able to recreate gait, I am confident that it would be successful with subjects with SCI. However, there are still areas for improvements that can be made to make the system more user friendly. A limitation of this system is that the control

system is set up for trajectory tracking, which imposes a trajectory on the subject. While, these trajectories are computed through optimizations and are arguably more optimal than trajectories recorded from able bodied subjects, they are still being imposed. The more control the subjects have over the system, the more comfortable they would be. A simple way to improve on this work and give the subject more control of the system besides when they take a step, is to give them control over the progression of time for the desired trajectories, i.e., the trajectories only advance in time while a button is pressed. The use of a button with pressure sensitivity would allow them to also control the speed of the time progression of the trajectories, i.e. the harder they press the button, the faster the trajectories progress. An even simpler system would be to just use the dynamic postural synergies in the feedforward path, and the pressure sensitive button would dictate the synergy activation, i.e., as they press the button for the first synergy, the hybrid neuroprosthesis would activate to produce the withdrawal reflex, then the second button would activate the second synergy to extend the knee, etc.

The current control system uses model-based estimators to estimate the fatigue and activation states that are used in the control law. While, system identification experiments were performed to accurately estimate the dynamic parameters for the model, measuring the states online using sensors would be more accurate. The muscle activation state can easily be measured using EMG, however, the electrical stimulation due to FES masks the signals and makes them unusable. The development of a masking circuit to only read the EMG signal in between the stimulation pulse trains would fix this issue. For the fatigue state, the only way to currently measure fatigue is in the isometric configuration using a load cell. However, recently conducted research is looking into using ultrasound imaging machines to capture images of the muscle fibers. Image processing algorithms can then extrapolate the stress strain relationships of the muscle fibers which studies have shown are related to muscle fatigue. If possible, these methods of sensing the fatigue state and activation state can be used instead of estimating these signals. However, these signals are not crucial for the operation of the control system, so the model-based estimates are adequate in the meantime.

BIBLIOGRAPHY

- [1] Marko Ackermann and Antonie J Van den Bogert. Optimality principles for model-based prediction of human gait. *Journal of biomechanics*, 43(6):1055–1060, 2010.
- [2] N. Alibeji, N. Kirsch, S. Farrokhi, and N. Sharma. Further results on predictor-based control of neuromuscular electrical stimulation. *IEEE Trans. Neural Syst. Rehabil. Eng.*, 2015.
- [3] N. Alibeji, N. Kirsch, and N. Sharma. Control of functional electrical stimulation in the presence of electromechanical and communication delays. In *6th International IEEE/EMBS Conference on NER*, pages 299–302, 2013.
- [4] Naji Alibeji, Nicholas Kirsch, and Nitin Sharma. Dynamic surface control of neuromuscular electrical stimulation of a musculoskeletal system with activation dynamics and an input delay. In *American Control Conference (ACC)*, pages 631–636. IEEE, 2015.
- [5] P.K. Artemiadis and K.J. Kyriakopoulos. EMG-based control of a robot arm using low-dimensional embeddings. *IEEE Trans. on Rob.*, 26(2):393–398, 2010.
- [6] Z. Artstein. Linear systems with delayed controls: A reduction. *IEEE Trans. Autom. Control*, 27(4):869–879, 1982.
- [7] T. Bajd, A. Kralj, R. Turk, H. Benko, and J. Šega. The use of a four-channel electrical stimulator as an ambulatory aid for paraplegic patients. *Phys. Ther.*, 63:1116–1120, 1983.
- [8] M. Bellman, T. Cheng, R. Downey, and W. Dixon. Stationary cycling induced by switched functional electrical stimulation control. In *Proc. of ACC*, 2014.
- [9] Max Berniker, Anthony Jarc, Emilio Bizzi, and Matthew C Tresch. Simplified and effective motor control based on muscle synergies to exploit musculoskeletal dynamics. *Proceedings of the National Academy of Sciences*, 106(18):7601–7606, 2009.
- [10] C. Bickel, C. Gregory, and J. Dean. Motor unit recruitment during neuromuscular electrical stimulation: a critical appraisal. *Eur. J. Appl. Physiol.*, 111(10):2399–2407, 2011.

- [11] Stuart A Binder-Macleod, Jesse C Dean, and Jun Ding. Electrical stimulation factors in potentiation of human quadriceps femoris. *Muscle & nerve*, 25(2):271–279, 2002.
- [12] W. L. Buford, Jr., F. M. Ivey, Jr., J. D. Malone, R. M. Patterson, G. L. Peare, D. K. Nguyen, and A. A. Stewart. Muscle balance at the knee - moment arms for the normal knee and the ACL - minus knee. *IEEE Trans. Rehabil. Eng.*, 5(4):367–379, 1997.
- [13] Manuel G Catalano, Giorgio Grioli, Alessandro Serio, Edoardo Farnioli, Cristina Piazza, and Antonio Bicchi. Adaptive synergies for a humanoid robot hand. In *IEEE Humanoid Rob.*, pages 7–14, 2012.
- [14] PR Cavanagh and PV Komi. Electromechanical delay in human skeletal muscle under concentric and eccentric contractions. *Eur. J. Appl. Physiol. Occup. Physiol.*, 42(3):159–163, 1979.
- [15] E K Chadwick, D Blana, J D Simeral, J Lambrecht, S P Kim, A S Cornwell, D M Taylor, L R Hochberg, J P Donoghue, and R F Kirsch. Continuous neuronal ensemble control of simulated arm reaching by a human with tetraplegia. *J. Neural Eng.*, 8(3):034003, 2011.
- [16] K-J Cho, Josiah Rosmarin, and Harry Asada. SBC hand: a lightweight robotic hand with an SMA actuator array implementing c-segmentation. In *ICRA*, pages 921–926. IEEE, 2007.
- [17] P Cooman and R. F. Kirsch. Control of a time-delayed 5 degrees of freedom arm model for use in upper extremity functional electrical stimulation. In *Annual Int. Conf. of the IEEE EMBC*, pages 322–324. IEEE, 2012.
- [18] A. d’Avella and M. C. Tresch. Modularity in the motor system: decomposition of muscle patterns as combinations of time-varying synergies. In *Advances in Neural Information Processing Systems 14*, pages 141–148, 2001.
- [19] Rahman Davoodi, Brian J Andrews, Garry D Wheeler, and Robert Lederer. Development of an indoor rowing machine with manual FES controller for total body exercise in paraplegia. *IEEE Trans. Neural Syst. Rehabil. Eng.*, 10(3):197–203, 2002.
- [20] Aymar de Rugy, Gerald E Loeb, and Timothy J Carroll. Are muscle synergies useful for neural control? *Front. Comput. Neurosci.*, 7, 2013.
- [21] A. del Ama, Á. Gil-Agudo, J. Pons, and J. Moreno. Hybrid FES-robot cooperative control of ambulatory gait rehabilitation exoskeleton. *J. NeuroEng. Rehabil.*, 11(1):27, 2014.
- [22] Antonio J del Ama, Aikaterini D Koutsou, Juan C Moreno, Ana de-los Reyes, A Gil-Agudo, and José L Pons. Review of hybrid exoskeletons to restore gait following spinal cord injury. *J. Rehabil. Res. Dev.*, 49(4):497–514, 2012.

- [23] J. Ding, AS Wexler, and SA Binder-Macleod. A predictive fatigue model. I. predicting the effect of stimulation frequency and pattern on fatigue. *IEEE Trans. Rehabil. Eng.*, 10(1):48–58, 2002.
- [24] J. Ding, AS Wexler, and SA Binder-Macleod. A predictive fatigue model. II. predicting the effect of resting times on fatigue. *IEEE Trans. Rehabil. Eng.*, 10(1):59–67, 2002.
- [25] Strahinja Dosen and Dejan B Popovic. Accelerometers and force sensing resistors for optimal control of walking of a hemiplegic. *IEEE Trans. Biomed. Eng.*, 55(8):1973–1984, 2008.
- [26] Strahinja Dosen and Dejan B Popovic. Moving-window dynamic optimization: design of stimulation profiles for walking. *IEEE Trans. Biomed. Eng.*, 56(5):1298–1309, 2009.
- [27] R. Downey, M. Bellman, N. Sharma, Q. Wang, C. Gregory, and W. Dixon. A novel modulation strategy to increase stimulation duration in neuromuscular electrical stimulation. *Muscle & Nerve*, 44(3):382–387, 2011.
- [28] R. Downey, T. Cheng, M. Bellman, and W. Dixon. Closed-loop asynchronous electrical stimulation prolongs functional movements in the lower body. *IEEE Trans. Neural. Syst. Rehabil. Eng.*, Pre-print available online.
- [29] R. J. Downey, T. H. Cheng, M. J. Bellman, and W. E. Dixon. Switched tracking control of a human limb during asynchronous neuromuscular electrical stimulation. In *Proc. of ACC*, pages 4504–4508, July 2015.
- [30] R J Downey, Teng-Hu H Cheng, and W E Dixon. Tracking control of a human limb during asynchronous neuromuscular electrical stimulation. In *IEEE 52nd Annual CDC*, pages 139–144, 2013.
- [31] William K Durfee and Jeffrey M Hausdorff. Regulating knee joint position by combining electrical stimulation with a controllable friction brake. *Ann. Biomed. Eng.*, 18(6):575–596, 1990.
- [32] W.K. Durfee and K.I. Palmer. Estimation of force-activation, force-length, and force-velocity properties in isolated, electrically stimulated muscle. *IEEE Trans. Biomed. Eng.*, 41(3):205–216, 1994.
- [33] M. Ebrahimpour and A. Erfanian. Comments on “sliding mode closed-loop control of FES: Controlling the shank movement”. *Biomedical Engineering, IEEE Transactions on*, 55(12):2842–2843, 2008.
- [34] R. Farris, H. Quintero, and M. Goldfarb. Preliminary evaluation of a powered lower limb orthosis to aid walking in paraplegic individuals. *IEEE Trans. Neural Syst. Rehabil. Eng.*, 19(6):652–659, 2011.

- [35] R.J. Farris, H.A. Quintero, T.J. Withrow, and M. Goldfarb. Design and simulation of a joint-coupled orthosis for regulating FES-aided gait. In *IEEE ICRA*, pages 1916–1922, 2009.
- [36] Maurizio Ferrarin and Antonio Pedotti. The relationship between electrical stimulus and joint torque: a dynamic model. *Rehabilitation Engineering, IEEE Transactions on*, 8(3):342–352, 2000.
- [37] C. Freeman, D. Tong, K. Meadmore, A. Hughes, E. Rogers, and J. Burridge. FES based rehabilitation of the upper limb using input/output linearization and ILC. In *American Control Conference*, pages 4825–4830. IEEE, 2012.
- [38] Chris T Freeman, Ann-Marie Hughes, Jane H Burridge, Paul H Chappell, Paul L Lewin, and Eric Rogers. A model of the upper extremity using FES for stroke rehabilitation. *Journal of biomechanical engineering*, 131(3):031011, 2009.
- [39] H. Geyer and H. Herr. A muscle-reflex model that encodes principles of legged mechanics produces human walking dynamics and muscle activities. *IEEE Trans Neural Syst Rehabil Eng.*, 18(3):263–273, 2010.
- [40] Yohanan Giat, Joseph Mizrahi, and Mark Levy. A musculotendon model of the fatigue profiles of paralyzed quadriceps muscle under FES. *IEEE Trans. Biomed. Eng.*, 40, no. 7:664–674, 1993.
- [41] M. Goldfarb and W. Durfee. Design of a controlled-brake orthosis for FES-aided gait. *IEEE T. Rehabil. Eng.*, 4(1):13–24, 1996.
- [42] M. Goldfarb, K. Korkowski, B. Harrold, and W. Durfee. Preliminary evaluation of a controlled-brake orthosis for FES-aided gait. *IEEE Trans. Neural Syst. Rehabil. Eng.*, 11(3):241–248, 2003.
- [43] M. Granat, A. Ferguson, B. Andrews, and M. Delargy. The role of functional electrical stimulation in the rehabilitation of patients with incomplete spinal cord injury - observed benefits during gait studies. *Spinal Cord*, 31(4):207–215, 1993.
- [44] Giorgio Grioli, Manuel Catalano, Emanuele Silvestro, Simone Tono, and Antonio Bicchi. Adaptive synergies: an approach to the design of under-actuated robotic hands. In *IEEE/RSJ IROS*, pages 1251–1256. IEEE, 2012.
- [45] K. Ha, S. Murray, and M. Goldfarb. An approach for the cooperative control of FES with a powered exoskeleton during level walking for persons with paraplegia. *IEEE Trans. Neural Syst. Rehabil. Eng.*, 2015.
- [46] K. Ha, H. Quintero, R. Farris, and M. Goldfarb. Enhancing stance phase propulsion during level walking by combining FES with a powered exoskeleton for persons with paraplegia. In *IEEE EMBC*, pages 344–347, 2012.

- [47] Xiaoran Han, Emilia Fridman, and Sarah K Spurgeon. Sliding mode control in the presence of input delay: A singular perturbation approach. *Automatica*, 48(8):1904–1912, 2012.
- [48] E. Hardin, R. Kobetic, L. Murray, M. Corado-Ahmed, G. Pinault, J. Sakai, S. Bailey, C. Ho, and R. Triolo. Walking after incomplete spinal cord injury using an implanted FES system: a case report. *J. Rehabil. Res. Dev.*, 44(3):333–346, 2007.
- [49] Kenneth J Hunt, Barry Stone, Nils-Otto Negård, Thomas Schauer, Matthew H Fraser, Andrew J Cathcart, Chiara Ferrario, Susan a Ward, and Stan Grant. Control strategies for integration of electric motor assist and functional electrical stimulation in paraplegic cycling: utility for exercise testing and mobile cycling. *IEEE Trans. Neural Syst. Rehabil. Eng.*, 12(1):89–101, 2004.
- [50] Sašo Jezernik, Ruben GV Wassink, and Thierry Keller. Sliding mode closed-loop control of FES controlling the shank movement. *IEEE Trans. Biomed. Eng.*, 51(2):263–272, 2004.
- [51] A Kantrowitz. Electronic physiologic aids. *Report of the Maimonides Hospital*, pages 4–5, 1960.
- [52] H. Kawai, M. Bellman, R. Downey, and W. E. Dixon. Tracking control for FES-cycling based on force direction efficiency with antagonistic bi-articular muscles. In *proc. of ACC*, 2014.
- [53] H. Khalil. *Nonlinear Systems*. Prentice Hall, 3rd edition, 2002.
- [54] N. Kirsch, N. Alibeji, W. Dixon, and N. Sharma. A nonlinear control method to compensate for muscle fatigue during neuromuscular electrical stimulation. *IEEE Transactions on Robotics*, Submitted.
- [55] N. Kirsch, N. Alibeji, L. Fisher, C. Gregory, and N. Sharma. A semi-active hybrid neuroprosthesis for restoring lower limb function in paraplegics. In *IEEE EMBC*, 2014.
- [56] Nicholas Kirsch, Naji A Alibeji, and Nitin Sharma. Optimized control of different actuation strategies for FES and orthosis aided gait. In *Proc. ASME DSCC*, 2013.
- [57] R. Kobetic, C.S. To, J.R. Schnellenberger, M.L. Audu, T.C. Bulea, R. Gaudio, G. Pinault, S. Tashman, and RJ Triolo. Development of hybrid orthosis for standing, walking, and stair climbing after spinal cord injury. *J. Rehabil. Res. Dev.*, 46(3):447–462, 2009.
- [58] R. Kobetic, R. Triolo, and E. Marsolais. Muscle selection and walking performance of multichannel FES systems for ambulation in paraplegia. *IEEE Trans. Rehabil. Eng.*, 5(1):23–29, 1997.
- [59] A.R. Kralj and T. Bajd. *Functional electrical stimulation: standing and walking after spinal cord injury*. CRC, 1989.

- [60] Janet L. Krevolin, Marcus G. Pandy, and John C. Pearce. Moment arm of the patellar tendon in the human knee. *J. Biomech.*, 37:785–788, 2004.
- [61] M. Levy, J. Mizrahi, and Z. Susak. Recruitment, force and fatigue characteristics of quadriceps muscles of paraplegics, isometrically activated by surface FES. *J. Biomed. Eng.*, 12:150–156, 1990.
- [62] WT Liberson, HJ Holmquest, David Scot, and Margot Dow. Functional electrotherapy: stimulation of the peroneal nerve synchronized with the swing phase of the gait of hemiplegic patients. *Arch. Phys. Med.*, 42:101–105, 1961.
- [63] C.L. Lynch and M.R. Popovic. A comparison of closed-loop control algorithms for regulating electrically stimulated knee movements in individuals with spinal cord injury. *IEEE Trans. Neural Syst. Rehabil. Eng.*, 20(4):539–548, 2012.
- [64] R.D. Maladen, R. Perumal, A.S. Wexler, and S.A. Binder-Macleod. Effects of activation pattern on nonisometric human skeletal muscle performance. *J. Appl. Physiol.*, 102(5):1985–91, 2007.
- [65] A. Manitius and A. Olbrot. Finite spectrum assignment problem for systems with delays. *IEEE Trans. Autom. Control*, 24(4):541–552, 1979.
- [66] E. Marsolais and R. Kobetic. Functional electrical stimulation for walking in paraplegia. *J. Bone Joint Surg.*, 69(5):728–733, 1987.
- [67] K. Masani, A H. Vette, N. Kawashima, and M R. Popovic. Neuromusculoskeletal torque-generation process has a large destabilizing effect on the control mechanism of quiet standing. *J. Neurophysiol.*, 100(3):1465, 2008.
- [68] Kei Masani, Albert H Vette, and Milos R Popovic. Controlling balance during quiet standing: proportional and derivative controller generates preceding motor command to body sway position observed in experiments. *Gait & Posture*, 23(2):164–172, 2006.
- [69] W. Michiels, K. Engelborghs, P. Vansevenant, and D. Roose. Continuous pole placement for delay equations. *Automatica*, 38(5):747–761, 2002.
- [70] R. Nathan and M. Tavi. The influence of stimulation pulse frequency on the generation of joint moments in the upper limb. *IEEE Trans. Biomed. Eng.*, 37:317–322, 1990.
- [71] Vahab Nekoukar and Abbas Erfanian. A decentralized modular control framework for robust control of FES-activated walker-assisted paraplegic walking using terminal sliding mode and fuzzy logic control. *IEEE Trans. Biomed. Eng.*, 59(10):2818–2827, 2012.
- [72] Richard R. Neptune, David J. Clark, and Steven A. Kautz. Modular control of human walking: A simulation study. *J. Biomech.*, 42(9):1282–1287, 2009.

- [73] P. Neuhaus, J. Noorden, T. Craig, T. Torres, J. Kirschbaum, and J. Pratt. Design and evaluation of mina: A robotic orthosis for paraplegics. In *IEEE ICORR*, pages 1–8, 2011.
- [74] Serhat Obuz, Ryan J Downey, Justin R Klotz, and Warren E Dixon. Unknown time-varying input delay compensation for neuromuscular electrical stimulation. In *Proc. of 2015 IEEE Conference on Control Applications*, pages 365–370. IEEE, 2015.
- [75] Marcus G Pandy and Thomas P Andriacchi. Muscle and joint function in human locomotion. *Annual review of biomedical engineering*, 12:401–433, 2010.
- [76] P. H. Peckham and D. B. Gray. Functional neuromuscular stimulation. *J. Rehabil. Res. Dev.*, 33:9–11, 1996.
- [77] P. Hunter Peckham and Jayme S Knutson. Functional electrical stimulation for neuromuscular applications. *Annu. Rev. Biomed. Eng.*, 7:327–360, 2005.
- [78] D. Popović, R. Stein, M. Oğuztöreli, M. Lebedowska, and S. Jonić. Optimal control of walking with functional electrical stimulation: a computer simulation study. *IEEE Trans. Rehabil. Eng.*, 7(1):69–79, 1999.
- [79] Dejan Popović. Hybrid assistive system-the motor neuroprosthesis. In *IEEE Trans. Biomed. Eng.*, volume 36, 1989.
- [80] Dejan B. Popović, Milovan Radulović, Laszlo Schwirtlich, and Novak Jauković. Automatic vs hand-controlled walking of paraplegics. *Med. Eng. Phys.*, 25(1):63–73, 2003.
- [81] H. Quintero, R. Farris, W. Durfee, and M. Goldfarb. Feasibility of a hybrid-FES system for gait restoration in paraplegics. In *IEEE EMBC*, pages 483–486, 2010.
- [82] Hugo Quintero, Ryan Farris, Kevin Ha, and Michael Goldfarb. Preliminary assessment of the efficacy of supplementing knee extension capability in a lower limb exoskeleton with FES. In *IEEE Eng. Med. Biol. Soc.*, volume 2012, pages 3360–3, 2012.
- [83] R. Riener and Thomas Fuhr. Patient-driven control of FES-supported standing up: A simulation study. *IEEE Trans. Rehabil. Eng.*, 6:113–124, 1998.
- [84] R. Riener, J. Quintern, and G. Schmidt. Biomechanical model of the human knee evaluated by neuromuscular stimulation. *J. Biomech.*, 29:1157–1167, 1996.
- [85] Josiah B Rosmarin and H Harry Asada. Synergistic design of a humanoid hand with hybrid DC motor-SMA array actuators embedded in the palm. In *IEEE ICRA*, pages 773–778, 2008.
- [86] D.W. Russ, K. Vandenborne, and S.A. Binder-Macleod. Factors in fatigue during intermittent electrical stimulation of human skeletal muscle. *J. Appl. Physiol.*, 93(2):469–478, 2002.

- [87] T. Schauer, N. O. Negard, F. Previdi, K. J. Hunt, M. H. Fraser, E. Ferchland, and J. Raisch. Online identification and nonlinear control of the electrically stimulated quadriceps muscle. *Control Eng. Pract.*, 13:1207–1219, 2005.
- [88] E.M. Scheerer, Yu-Wei Liao, E.J. Perreault, M.C. Tresch, W.D. Memberg, R.F. Kirsch, and K.M. Lynch. Multi-muscle FES force control of the human arm for arbitrary goals. *IEEE Trans. Neural Syst. Rehabil. Eng.*, 22(3):654–663, 2014.
- [89] N. Sharma. A predictor-based compensation for electromechanical delay during neuromuscular electrical stimulation-II. In *Proc. of ACC*, pages 5604–5609, 2012.
- [90] N. Sharma, S. Bhasin, Q. Wang, and W. E. Dixon. Predictor-based control for an uncertain euler-lagrange system with input delay. *Automatica*, 47(11):2332–2342, 2011.
- [91] N. Sharma, C. Gregory, and W. E. Dixon. Predictor-based compensation for electromechanical delay during neuromuscular electrical stimulation. *IEEE Trans. Neural Syst. Rehabil. Eng.*, 19(6):601–611, 2011.
- [92] N. Sharma, V. Mushahwar, and R. Stein. Dynamic optimization of FES and orthosis-based walking using simple models. *IEEE Trans. Neural Syst. Rehabil. Eng.*, 22(1):114–126, 2014.
- [93] N Sharma, PM Patre, CM Gregory, and WE Dixon. Nonlinear control of NMES: Incorporating fatigue and calcium dynamics. In *Proceedings of ASME Dynamic Systems and Control Conference*. ASME, 2009.
- [94] N. Sharma, K. Stegath, C. M. Gregory, and W. E. Dixon. Nonlinear neuromuscular electrical stimulation tracking control of a human limb. *IEEE Trans. Neural Syst. Rehabil. Eng.*, 17(6):576–584, 2009.
- [95] N. Sharma and R. Stein. Optimal trajectory planning for a constrained functional electrical stimulation-based human walking. In *2011 Annual International Conference of the IEEE EMBS*, pages 603–607, 2011.
- [96] Nitin Sharma, Chris M Gregory, Marcus Johnson, and Warren E Dixon. Closed-loop neural network-based NMES control for human limb tracking. *IEEE Trans. Control Syst. Technol.*, 20(3):712–725, 2012.
- [97] C S Sherrington. Flexion-reflex of the limb, crossed extension-reflex, and reflex stepping and standing. *J. Physiol.*, 40(1-2):28–121, 1910.
- [98] Margaret M Skelly and Howard Jay Chizeck. Real-time gait event detection for paraplegic FES walking. *IEEE Trans. on Neural Sys. and Rehab. Eng.*, 9(1):59–68, 2001.
- [99] J. E Slotine and W. Li. *Applied nonlinear control*, volume 199. Prentice-Hall Englewood Cliffs, NJ, 1991.
- [100] O.J. M. Smith. A controller to overcome deadtime. *J. ISA*, 6:28–33, 1959.

- [101] M. Solomonow, R. Baratta, H. Shoji, M. Ichie, S. Hwang, N. Rightor, W. Walker, R. Douglas, and R. D'Ambrosia. FES powered locomotion of paraplegics fitted with the LSU reciprocating gait orthoses (RGO). In *Proc. IEEE EMBS*, volume 4, page 1672, 1988.
- [102] K. Strausser and H. Kazerooni. The development and testing of a human machine interface for a mobile medical exoskeleton. In *IEEE/RSJ IROS*, pages 4911–4916, 2011.
- [103] D. Swaroop, J.C. Gerdes, P. Patrick Yip, and J Karl Hedrick. Dynamic surface control of nonlinear systems. In *Proc. of ACC*, volume 5, pages 3028–3034, 1997.
- [104] D. Swaroop, J Karl Hedrick, P. Patrick Yip, and J.C. Gerdes. Dynamic surface control for a class of nonlinear systems. *IEEE Transactions on Automatic Control*, 45(10):1893–1899, 2000.
- [105] The National SCI Statistical Center. Spinal cord injury (SCI) facts and figures at a glance, 2016.
- [106] T. Adam Thrasher, Vera Zivanovic, William McIlroy, and Milos R. Popovic. Rehabilitation of reaching and grasping function in severe hemiplegic patients using functional electrical stimulation therapy. *Neurorehab. Neural. Re.*, 22(6):706–714, 2008.
- [107] Lena H. Ting. Dimensional reduction in sensorimotor systems: a framework for understanding muscle coordination of posture. In *Prog. Brain. Res.*, volume 165, pages 299 – 321. Elsevier, 2007.
- [108] C To, R Kobetic, J Schnellenberger, M Audu, and R Triolo. Design of a variable constraint hip mechanism for a hybrid neuroprosthesis to restore gait after spinal cord injury. *IEEE/ASME Trans. Mechatronics*, 13(2):197–205, 2008.
- [109] Emanuel Todorov, Weiwei Li, and Xiuchuan Pan. From task parameters to motor synergies: A hierarchical framework for approximately optimal control of redundant manipulators. *J. of Rob. Sys.*, 22(11):691–710, 2005.
- [110] Matthew C Tresch and Anthony Jarc. The case for and against muscle synergies. *Curr. Opin. Neurobiol.*, 19(6):601 – 607, 2009.
- [111] Ronald J Triolo, Carol Bieri, James Uhlir, Rudi Kobetic, Avram Scheiner, and E Byron Marsolais. Implanted functional neuromuscular stimulation systems for individuals with cervical spinal cord injuries: clinical case reports. *Archives of physical medicine and rehabilitation*, 77(11):1119–1128, 1996.
- [112] A. H. Vette, K. Masani, and M R. Popovic. Implementation of a physiologically identified PD feedback controller for regulating the active ankle torque during quiet stance. *IEEE Trans. Neural Syst. Rehabil. Eng.*, 15(2):235–243, 2007.

- [113] A H. Vette, K. Masani, and M R. Popovic. Neural-mechanical feedback control scheme can generate physiological ankle torque fluctuation during quiet standing: A comparative analysis of contributing torque components. In *IEEE Int. CCA*, pages 660–665. IEEE, 2008.
- [114] Ramana Vinjamuri, Mingui Sun, Cheng-Chun Chang, Heung-No Lee, Robert J Sclabassi, and Zhi-Hong Mao. *Dimensionality reduction in control and coordination of the human hand*. PhD thesis, 2010.
- [115] Ramana Kumar Vinjamuri. *Dimensionality Reduction in Control and Coordination of the Human Hand*. PhD thesis, Swanson School of Engineering, University of Pittsburgh, 2008.
- [116] Ramana Kumar Vinjamuri, Douglas J Weber, Zhi-Hong Mao, Jennifer L Collinger, Alan D Degenhart, John W Kelly, Michael L Boninger, Elizabeth C Tyler-Kabara, and Wei Wang. Toward synergy-based brain-machine interfaces. *IEEE Trans. Inf. Technol. Biomed.*, 15(5):726–736, 2011.
- [117] D. Wang and Jie Huang. Neural network-based adaptive dynamic surface control for a class of uncertain nonlinear systems in strict-feedback form. *IEEE Transactions on Neural Networks*, 16(1):195–202, 2005.
- [118] T. Watanabe, R. Futami, N. Hoshimiya, and Y. Handa. An approach to a muscle model with a stimulus frequency-force relationship for FES applications. *IEEE Trans. Rehabil. Eng.*, 7, no. 1:12–17, 1999.
- [119] D. Winter. *Biomechanics and motor control of human movement*. Wiley, 2009.
- [120] P. Patrick Yip and J Karl Hedrick. Adaptive dynamic surface control: a simplified algorithm for adaptive backstepping control of nonlinear systems. *Int. J. Control*, 71:959–979, 1998.
- [121] S. Zhou, D. L. Lawson, W. E. Morrison, and I. Fairweather. Electromechanical delay in isometric muscle contractions evoked by voluntary, reflex and electrical stimulation. *Eur. J. Appl. Physiol. Occup. Physiol.*, 70(2):138–145, 1995.